A Lippmann-Schwinger approach to the photoelectron final state

Mathias Schwendt
Doctoral thesis
under the supervision of Univ. Prof. Dr. Peter Puschnig
Institute of Physics
University of Graz
January 2026

Abstract

In this thesis, we develop new methods for the simulation of photoemission spectra of valence band states of oriented molecular layers on metal substrates. Specifically, we address the question of how the final state of the photoelectron should be calculated in the one-step model of the photoemission process. All methods are based on the solution of the Lippmann-Schwinger equation, which is a reformulation of the Schrödinger equation for the photoelectron in the system that explicitly incorporates the boundary conditions of the photoelectron. The main purpose of this thesis is to thereby alleviate the shortcomings of the widely used plane-wave approximation for the final state of the photoelectron, which disregards all interactions of the photoelectron with the system. Broadly speaking, the developed methods fall into two categories. One class of methods aims to describe the photoemission of periodic systems and is formulated in momentum space. The implementation of these methods, however, proved to be not successful. Therefore, an alternative attempt is geared towards the description of gas-phase systems. This approach is based on a real space formulation of the Lippmann-Schwinger equation, which we first illustrate on the example of a toy model describing an electron bound inside a spherical box. In the next step, we apply it to real atoms as well as to planar and non-planar organic molecules. The chosen examples address some well-known shortcomings of the plane-wave approximation, such as its inability to account for circular dichroism.

Kurzzusammenfassung

Diese Arbeit befasst sich mit der Entwicklung neuer Methoden zur Simulation von Photoemissionsspektren von Valenzbandzuständen orientierter molekularer Filme auf Metalloberflächen. Konkret wird der Frage nachgegangen, wie der Endzustand der Photoemission in der one-step Beschreibung berechnet werden soll. Alle Methoden beruhen auf der Lösung der Lippmann-Schwinger Gleichung, die im Gegensatz zur Schrödingergleichung die Randbedingungen, denen das Photoelektron unterworfen ist, explizit enthält. Das Ziel dieser Arbeit ist dabei, die gröbsten Mängel der populären Näherung der freien Elektronen für den Endzustand des Photoelektrons zu beheben, die die Wechselwirkungen zwischen Photoelektron und System völlig vernachlässigt. Die entwickelten Methoden fallen in zwei Kategorien. Zum einen die Methoden, die die Photoemission von periodischen Systemen beschreiben sollen und im Wellenraum formuliert sind. Die Implementierung dieser Methoden hat sich als nicht erfolgreich erwiesen. Deshalb wurde eine alternative Methode implementiert, die Gasphasensysteme beschreibt und im Realraum formuliert ist. Wir illustrieren diese Methode zuerst anhand ihrer Anwendung auf ein einfaches Modellsystem eines Elektrons in einem radialen Boxpotential. In einem weiteren Schritt werden reale Atome und flache sowie dreidimensionale Moleküle damit behandelt. Die ausgewählten Beispiele behandeln bekannte Mängel der Näherung der freien Elektronen, wie etwa die Unmöglichkeit, zirkularen Dichroismus damit zu beschreiben.

Acknowledgements

I am grateful to my supervisor Peter Puschnig, who is easily one of the most patient men I have ever encountered. I also thank his group members, in particular Dominik Brandstetter and Christian Kern, for providing help and discussions. I owe a special debt of gratitude to Daniel Lüftner, who introduced me to the computational framework of our group, but then unfortunately had to leave for industry. The IT department run by Christop Ruthofer and David Schafzahl has always provided help when it was needed.

Contents

Chapter 1

Introduction and overview

Ever since Einstein's introduction of the photon concept [1], the photoelectric effect has occupied a prominent role in the history of quantum mechanics. There it has been used to demonstrate the existence of photons, photon concept, quanta of the electromagnetic field. Nowadays, the photoeffect is treated as a straightforward application of Fermi's golden rule in many quantum mechanics textbooks [2]. Typically, to simplify the description, the initial state in these treatments is the 1s orbital of hydrogen and the final state of the photoelectron is assumed to be a plane wave, which disregards all interactions of the photoelectron with the remaining hydrogen ion. Even in this simple system, this leads to a qualitatively wrong behavior at low kinetic energies of the photoelectron, say roughly below 100 eV, which is precisely the region of interest to us. In the seventies, experiments were extended to ordered molecular layers adsorbed on metal surfaces. The plane-wave approximation was introduced by Gadzuk to provide a simple description [3]. In contrast to the photoionization of hydrogen, where the plane-wave approximation could readily be replaced by an accurate calculation [4], it was considerably more difficult to give a more realistic account of the interaction of the photoelectron with the remaining system. Soon after, Grobman introduced the independent-atomic-center approximation [5], which, however, remained relatively intractable due to the low computational power available at the time.

High-temperature superconductors, and more recently quantum materials in general, gave a new impetus to the field of angle-resolved photoemission [6, 7]. Here, it was clear that it was necessary to include many-body effects into the simulation of the photoemission process, which are often negligible in simpler systems. Nevertheless, the experimental advancements were also instrumental to the renewed interest in the study of molecular films adsorbed on metal substrates.

The plane-wave approximation for the photoelectron final state resurfaced in the year 2009 [8]. Since then, it has been successfully applied to various problems, among them: the photoemission from aromatic hydrocarbon molecules [9], the charge transfer across dielectric layers [10], the bonding in metal-organic-frameworks [11], and the photoemission of excitons [12]. Despite its wide success, it was always clear that the plane-wave approximation would fail in certain regards [8, 13]. A widely employed method to that purpose is based on time-dependent density functional theory [14, 15]. This method is ideally suited to study time-resolved photoemission [16], which makes it possible to follow electronic processes in time and study excited state properties. The main purpose of this thesis is to implement a method that is as accurate as time-dependent density functional theory, while being simpler to implement, albeit at the price of being restricted to time-independent phenomena. We might also mention that the independent-atomic-center approximation was revived in Ref. [17].

The thesis concerns itself with the following topics. We start with a short chapter that gathers some fundamental concepts. Since some of these topics are already treated exhaustively in the literature, we only include the aspects that are directly relevant for our purposes. Initially we thought that the Born approximation would be sufficiently accurate to quantitatively account for the spectra. This belief turned out to be ill-funded. Consequently, we had to solve the Lippmann-Schwinger equation directly. We developed different methods to this end. In Chapter 3, we start with a formulation in wavevector space geared toward describing periodic systems. The methods in this chapter suffer from problems that we could not resolve, and are included here to allow for a comparison with a very recent and successful alternative implementation [18].

Taking a step back, we decided to investigate the photoemission of a simple toy model, the particle in a box. To this end, the Lippmann-Schwinger equation was treated in a real space approach, and the results were encouraging. Therefore, we moved on to the study of atomic systems. The results of these efforts are the subject of Chapter 4 and 5.

Chapter 6 contains the central theoretical result of this thesis. Here we develop a real space method that is capable of describing the photoemission of gas-phase molecules. We address some well known shortcomings of the plane-wave approximation of the final state. In particular, as we will see in Chapter 6, the plane-wave approximation erroneously predicts that the photoemission intensity vanishes in certain polarization configurations [13]. Similarly, it predicts vanishing circular dichroism [19]. In addition, we show simulations of the photoemission of non-planar molecules, another area where the plane-wave approximation often falls short [14]. A

comparison with results from time dependent density functional theory simulations is also included.

During the course of the PhD, additional investigations were carried out [20, 21]. But, since these contributions lie somewhat outside the main thrust of this thesis, they are not included here.

Chapter 2

Fundamental concepts

2.1 Physical systems of interest

The main focus of this work lies on understanding the valence band angle-resolved photoelectron spectroscopy of thin films or layers adsorbed on metal surfaces. The layer substances can range from molecules, where, depending on the surface geometry, molecular interactions may or may not play a prominent role, to newer 2D-materials, such as graphene [22] or transition metal dichalcogenides (TMD) [23]. Both single and multiple layers can be deposited on the surface, see for example [24]. Typically, metal substrates of high symmetry, such as the (100), (110) and (111) surfaces of FCC lattices, are used to facilitate the analysis. Since photoelectron spectroscopy is an area averaging technique, it is essential that there is long-range order in the molecular films. The choice of the layer on the metal surface can be guided by questions of fundamental interest, e.g. using circular dichroism to study orbital angular momentum [25], or by more applied interest, e.g. to better understand practically relevant interfaces.
Organic molecules, such as benzene and tetracene, are the most common option for molecular surface layers, as they readily form ordered films on metal subsrates and lead to a distinct angular distribution of photoelectrons [26].

2.2 Relevant aspects of density functional theory

The main computational tool of this thesis is (time-independent) density functional theory (DFT). DFT is a well established field by now and we limit ourselves to a very short introduction here. More information can be found in the voluminous

literature, see e.g. the books [27, 28] for pedagogical treatments of the subject. We will, however, highlight some aspects of DFT that are usually given less attention in more practically minded expositions, such as the nonlocal potential, which is needed when pseudowavefunctions, instead of all-electron wavefunctions, are calculated. In this thesis, we use atomic units, i.e., $\hbar = m_e = e = 1$ and $4\pi\epsilon_0 = 1$. We follow the treatment given in [28].

2.2.1 Density functional theory in a nutshell

DFT reduces the interacting many particle Schrödinger equation to a system of noninteracting orbitals that are governed by the Kohn-Sham equations

$$\left[-\frac{\nabla^2}{2} + v_{\mathrm{KS}}[n](\boldsymbol{r})\right]\varphi_i(\boldsymbol{r}) = \epsilon_i\varphi_i(\boldsymbol{r}). \tag{2.1}$$

The potential v_{KS} is a functional of the ground state density, which in turn is determined by the orbitals via

$$n(\boldsymbol{r}) = \sum_i^{\mathrm{occ}} |\varphi_i(\boldsymbol{r})|^2, \tag{2.2}$$

where the sum includes all occupied orbitals. The potential v_{KS} is split up into three contributions

$$v_{\mathrm{KS}}[n](\boldsymbol{r}) = v_{\mathrm{ext}}(\boldsymbol{r}) + v_{\mathrm{Hartree}}[n](\boldsymbol{r}) + v_{\mathrm{xc}}[n](\boldsymbol{r}). \tag{2.3}$$

The external potential $v_{\mathrm{ext}}(\boldsymbol{r})$ includes the electrostatic potential of the nuclei, and, if present, any external fields. The Hartree potential $v_{\mathrm{Hartree}}[n](\boldsymbol{r})$ is also a functional of the density and determined by the Poisson equation:

$$\nabla^2 v_{\mathrm{Hartree}}(\boldsymbol{r}) = -4\pi n(\boldsymbol{r}). \tag{2.4}$$

The exchange-correlation potential v_{xc} considers Pauli's exchange principle and accounts for effects arising from electron correlations. Its exact form is unknown, therefore it needs to be approximated. The two most popular choices are the local density approximation (LDA) [29, 30] and the generalized gradient approximation (GGA) [31]. Although there is an ongoing effort to find ever more accurate functional approximations for the exchange-correlation potential (see [32] for a critical take on this) we limit ourselves to these two approximations. It must also be stressed that neither the Kohn-Sham potential nor the Kohn-Sham orbitals have any direct physical meaning.

2.2.2 All-electron orbitals and pseudoorbitals

The orbitals from the above section are referred to as all-electron wavefunctions since they treat all electrons in the system on the same footing. To reduce the computation burden, often so-called pseudowavefunctions are used instead of all-electron wavefunctions. The pseudoorbital concept rests on the observation that core states are relatively inert compared to valence states, which are mainly responsible for chemical bonding. Therefore, the idea of the pseudopotential concept is to replace these core states entirely by means of a modified potential. This pseudopotential will be much smoother around the origin and hence reduce the computational burden significantly. There are at least three methods for implementing pseudopotentials. The most straightforward way of doing so are norm-conserving pseudopotentials, see [33] for a state-of-the-art approach. The pseudoorbitals need not form an orthonormal set, however. The resulting implementation is more involved, but can result in a lower computational burden overall. The ultrasoft pseudopotential [34] and projector augmented wave methods [35] are two alternative ways to define pseudopotentials. In this thesis, we will work exclusively with norm-conserving pseudopotentials. The basic derivation of the pseudopotential is straightforward for norm-conserving pseudoptentials and we include it here because it is quite insightful.

The starting point is the Schrödinger equation for the core and valence states, that is,

$$H\left|\psi_n\right\rangle = E_n\left|\psi_n\right\rangle, \tag{2.5}$$

where $n = c, v$ for core and electron states respectively. Expanding the all-electron orbitals ψ_v into smoother pseudoorbitals φ_v and the core all-electron orbitals ψ_c

$$\left|\psi_v\right\rangle = \left|\varphi_v\right\rangle + \sum_c \alpha_{cv}\left|\psi_c\right\rangle \tag{2.6}$$

leads to a Schrödinger equation for the pseudoorbitals [28]

$$H_{\text{pseudo}}\left|\varphi_v\right\rangle = E_v\left|\varphi_v\right\rangle. \tag{2.7}$$

The energy E_v stays the same, but the Hamilton operator acquires an additional energy dependent term

$$H_{\text{pseudo}}(E) = H - \sum_c (E_c - E)\left|\psi_c\right\rangle\left\langle\psi_c\right|. \tag{2.8}$$

This means that the local potential of the original Schrödinger equation accquires an additional nonlocal term V_{nonlocal}

$$V_{\text{nonlocal}}(E) = -\sum_c (E_c - E)\left|\psi_c\right\rangle\left\langle\psi_c\right|. \tag{2.9}$$

The energy E is the valence energy of the state that $V_{\text{nonlocal}}(E)$ acts on, that is,

$$V_{\text{nonlocal}} |\varphi_v\rangle = -\sum_c (E_c - E_v) |\psi_c\rangle \langle\psi_c|\varphi_v\rangle . \tag{2.10}$$

The effect of this nonlocal term is limited to the region around the origin of the corresponding atom.

The most commonly used form of the nonlocal part is slightly more general than the above expression. It was derived in [36] and is given by

$$V_{\text{nonlocal}}(\boldsymbol{r}_1, \boldsymbol{r}_2) = \sum_{lmn} \frac{E_{ln}\chi_{ln}(r_1)\chi^*_{ln}(r_2)}{r_1 r_2} Y_{lm}(\hat{\boldsymbol{r}}_1) Y^*_{lm}(\hat{\boldsymbol{r}}_2). \tag{2.11}$$

This separable form is called the Kleinman-Bylander form. Here, E_{ln} are the (fixed) Kleinman-Bylander energies, the Y_{lm} are spherical harmonics and the radial projectors are χ_{ln}. The Kleinman-Bylander parameters E_{ln} and χ_{ln} are determined so as to obey some constraints that, among other things, ensure that all-electron and pseudowavefunctions agree outside some radius r_c and improve transferability, see [37] for details. The pseudowavefunctions obtained in this manner form an orthonormal set.

One downside of these so-called norm conserving pseudopotentials is that the all-electron wavefunctions cannot be reconstructed from the corresponding pseudowavefunctions. The projector augmented wave method lifts this restriction, but at the price of relaxing the orthonormality of the pseudowavefunctions [27].

2.3 The Lippmann-Schwinger equation and the Born series

The Schrödinger differential equation for one particle in a potential V

$$\left(-\frac{1}{2}\nabla^2 + V(\boldsymbol{r})\right)\psi(\boldsymbol{r}) = E\psi(\boldsymbol{r}) \tag{2.12}$$

can be recast into an implicit integral equation, the so-called Lippmann-Schwinger (LS) equation [38],

$$\psi(\boldsymbol{r}) = \phi(\boldsymbol{r}) + \int d^3 r_1 G_0(\boldsymbol{r}, \boldsymbol{r}_1) V(\boldsymbol{r}_1)\psi(\boldsymbol{r}_1), \tag{2.13}$$

where G_0 denotes the free particle Green function given by [39]

$$G_0(\boldsymbol{r}, \boldsymbol{r}_1) = -\frac{1}{2\pi} \frac{e^{ik|\boldsymbol{r}-\boldsymbol{r}_1|}}{|\boldsymbol{r}-\boldsymbol{r}_1|}. \tag{2.14}$$

The wavenumber k is related to the energy E in the Schrödinger equation via

$$E = \frac{k^2}{2}. \tag{2.15}$$

The inhomogeinity on the right-hand side of the LS equation, ϕ, represents a plane wave, i.e.

$$\phi(\boldsymbol{r}) = e^{i\boldsymbol{k}\boldsymbol{r}}, \tag{2.16}$$

where $\boldsymbol{k}$ denotes the wavevector of the incoming particle. Importantly, the LS equation preserves the normalization of the wavefunctions, that is, ψ is automatically normalized in the same manner as ϕ [38]. The LS equation incorporates the boundary conditions directly into the equation. For this reason, the LS equation is particularly convenient to study scattering properties, where the scattered particle is typically detected as a spherical wave [38] far away from the interaction V. In this case, the incoming particle ϕ is a plane wave and the outgoing, scattered particle approaches a spherical wave asymptotically.

As it turns out, the time reversed process, where an asymptotically spherical wave impinges on the sample and scatters into a plane wave, is also of considerably interest, in particular for the description of the photoemission process [40]. In this case the LS equation that describes the above process is modified slightly to

$$\psi(\boldsymbol{r}) = \phi(\boldsymbol{r}) + \int d^3 r_1 G_0^*(\boldsymbol{r}, \boldsymbol{r}_1) V(\boldsymbol{r}_1) \psi(\boldsymbol{r}_1). \tag{2.17}$$

Alternatively, the LS equation can also be written in a representation independent manner, namely

$$|\psi\rangle = |\phi\rangle + G_0 V |\psi\rangle . \tag{2.18}$$

This way, the LS equation can be formulated in whichever representation is most suitable to the problem. For periodic systems, the LS equation is easier to handle in momentum space, while for finite systems a real space representation is more appropriate.

2.3.1 The Born series

The LS equation is implicit, that is, the solution ψ appears on both sides of the equation. Note that by discretizing the right-hand side of Eq. (2.13), the equation

can be rewritten as a linear system of equations as detailed in a later chapter. Often times, however, the solution is approximated, though [38]. To this end, the right-hand side is reinserted into itself (for ease of illustration we choose the representation independent formulation)

$$|\psi\rangle = |\phi\rangle + G_0 V |\psi\rangle = |\phi\rangle + G_0 V |\phi\rangle + G_0 V G_0 V |\psi\rangle . \tag{2.19}$$

If the potential is sufficiently small, and it is often not clear whether it is [38], then the new implicit term

$$G_0 V G_0 V |\psi\rangle \tag{2.20}$$

can be neglected. If it cannot be neglected, the process can be repeated until convergence is reached. This iterative process goes under the name of Born series [38]. In later chapters, it will become clear that the Born series is not useful for the description of the photoemission process, since the potential is indeed not small, thus the Born series does not converge.

2.3.2 Radial symmetry

The Green function formalism can be simplified in the case of a radially symmetric potential. The decomposition of the Green function into spherical harmonics is given by [38]

$$\begin{aligned} \frac{G(\boldsymbol{r}_1, \boldsymbol{r}_2)}{2} = -\frac{e^{ik|\boldsymbol{r}_1 - \boldsymbol{r}_2|}}{4\pi|\boldsymbol{r}_1 - \boldsymbol{r}_2|} &= \sum_{lm} G_k^{(l)}(r_1, r_2) Y_{lm}^*(\hat{\boldsymbol{r}}_1) Y_{lm}(\hat{\boldsymbol{r}}_2) \\ &= \sum_{lm} G_k^{(l)}(r_1, r_2) Y_{lm}(\hat{\boldsymbol{r}}_1) Y_{lm}^*(\hat{\boldsymbol{r}}_2), \end{aligned} \tag{2.21}$$

where

$$G_k^{(l)}(r; r') = -ikj_l(kr_<)h_l(kr_>). \tag{2.22}$$

In the radial symmetric case, the complete form of the wavefunction may be determined from [38]

$$\psi_{\boldsymbol{k}}(\boldsymbol{r}) = \sum_l \sqrt{\frac{2l+1}{2\pi^2}} i^l R_l(k; r) Y_{l0}(\theta), \tag{2.23}$$

where θ is the angle between the arbitrarily oriented $\boldsymbol{r}$ and $\boldsymbol{k}$. In the presence of a purely local radial potential V this leads to the following form for the radial part [38]:

$$R_l(k; r) = j_l(kr) + \int_0^\infty dr_1 r_1^2 G_k^{(l)}(r; r_1) U(r_1) R_l(k; r_1), \tag{2.24}$$

where a factor of two has been absorbed in $U(r) \equiv 2V(r)$.

A non-local potential of the Kleinman-Bylander form (which will be needed in the DFT examples later)

$$V(\boldsymbol{r}_1, \boldsymbol{r}_2) = \sum_{lmn} \frac{E_{ln}\chi_{ln}(r_1)\chi^*_{ln}(r_2)}{r_1 r_2} Y_{lm}(\hat{\boldsymbol{r}}_1) Y^*_{lm}(\hat{\boldsymbol{r}}_2) \tag{2.25}$$

results in the following equation for the radial part of the final state

$$R_l(k;r) = j_l(kr) + \sum_n \int_0^\infty dr_1 dr_2 r_1^2 {r_2}^2 G_k^{(l)}(r;r_1) \frac{E_{ln}\chi_{ln}(r_1)\chi^*_{ln}(r_2)}{r_1 r_2} R_l(k;r_2). \tag{2.26}$$

Defining

$$V_l(r_1, r_2) = \sum_n \frac{E_{ln}\chi_{ln}(r_1)\chi^*_{ln}(r_2)}{r_1 r_2}, \tag{2.27}$$

gives the more concise expression

$$R_l(k;r) = j_l(kr) + \int_0^\infty dr_1 dr_2 r_1^2 {r_2}^2 G_k^{(l)}(r;r_1) U_l(r_1, r_2) R_l(k;r_2), \tag{2.28}$$

where again $V_l(r_1, r_2)$ and $U_l(r_1, r_2)$ are related by a factor of two. In the presence of both a local potential $U_{\text{local}}(r)$ and a nonlocal potential the equation from above is generalized to

$$\begin{aligned} R_l(k;r) =& j_l(kr) + \int_0^\infty dr_1 r_1^2 G_k^{(l)}(r;r_1) U_{\text{local}}(r_1) R_l(k;r_1) \\ &+ \int_0^\infty dr_1 dr_2 r_1^2 {r_2}^2 G_k^{(l)}(r;r_1) U_l(r_1, r_2) R_l(k;r_2). \end{aligned} \tag{2.29}$$

Both the derivation of the radial Green function and the form of the radial LS equation in the presence of a nonlocal potential are simplified by some properties of spherical harmonics that we have gathered in the appendix to this chapter.

2.4 Photoemission

Here we start with a first-principles many-body description of the photoemission process to illustrate the approximations that are made on the way from a many-body to an effective one-body description of the photoelectron. Despite all simplifications, the single particle approximation still presents computational challenges, mainly in the computation of the final state.

2.4.1 From a many body description to a one body description

We follow the standard treatments in [6, 7]. The transition probability from an N-particle initial state $|\Psi_i^N\rangle$ to an N-particle final state $|\Psi_f^N\rangle$ that contains a photoelectron with energy E_{kin} and wavevector $\boldsymbol{k}$ is given by

$$I(\boldsymbol{k}) \propto |\langle \Psi_f^N | H_{\text{int}} | \Psi_i^N \rangle|^2 \delta(E_f^N - E_i^N - \hbar\omega), \tag{2.30}$$

where E_f^N and E_i^N are the final and initial state energies respectively. The delta function enforces energy conservation. The interaction Hamiltonian is approximated by

$$H_{\text{int}} \propto \boldsymbol{A}\boldsymbol{P}, \tag{2.31}$$

with the electromagnetic vector potential $\boldsymbol{A}$ and the momentum operator $\boldsymbol{P}$ of the N-electron system, i.e.

$$\boldsymbol{P} = \sum_i^N \boldsymbol{p}_i. \tag{2.32}$$

The expression neglects multiphoton processes and is only valid if the vector potential is spatially constant, which is approximately the case for light with photon energies below 100 eV, where the wavelength is $\lambda \approx 1.9$ nm, which is much larger than typical atomic dimensions of roughly 0.1 nm. This approximation is, however, invalid near the surface region where the fields vary on an atomic length scale [41]. We will nevertheless ignore this contribution in this thesis. This is the so-called dipole approximation. Also note that no scalar potential appears in the interaction Hamiltonian, which can always be achieved by a gauge choice, in this case the Weyl gauge [7].

To make progress, at this stage usually the sudden approximation is made. The photoelectron is assumed to be removed so quickly that it has no time to interact with the remaining system. This assumption breaks down at low kinetic energies of the photoelectron [42]. Within the sudden approximation, the final state contains one photoelectron of wavevector $\boldsymbol{k}$, while the rest of the system stays in one of the excited states of the remaining $N-1$ electron system, that is[1],

$$|\Psi_f^N\rangle = |\psi_{\boldsymbol{k}}\rangle\, |\Psi_m^{N-1}\rangle\,. \tag{2.33}$$

In most treatments, the initial state is assumed to be well approximated by a mean field theory and hence may be written as

$$|\Psi_i^N\rangle = |\psi_i\rangle\, |\Psi_i^{N-1}\rangle\,. \tag{2.34}$$

[1]The states are assumed to be properly antisymmetrized throughout this section.

The $N-1$ particle states $|\Psi_i^{N-1}\rangle$ are in general not eigenstates of the $N-1$ particle Hamilton operator. All initial and final states that lead to a photoelectron kinetic energy E_{kin} and wavevector $\boldsymbol{k}$ can contribute to the intensity I according to the formula

$$I(\boldsymbol{k}) \propto \sum_i |\langle\psi_{\boldsymbol{k}}|H_{\mathrm{int}}|\psi_i\rangle|^2 \sum_m |\langle\Psi_m^{N-1}|\Psi_i^{N-1}\rangle|^2 \delta(E_{\mathrm{kin}} + E_m^{N-1} - E_i^N - \hbar\omega). \quad (2.35)$$

The single particle description of photoemission is obtained from this expression if the initial state is assumed to be noninteracting. In this case the single determinant is exact and the $|\Psi_i^{N-1}\rangle$ are eigenstates of the $N-1$ particle Hamiltonian. This means that electron relaxation processes are neglected and the same orbitals make up the Slater determinant of the $N-1$ and N electron systems. Accordingly,

$$\langle\Psi_m^{N-1}|\Psi_i^{N-1}\rangle = \delta_{i,m}. \quad (2.36)$$

As a consequence, only single particle orbitals are needed to evaluate the photoemission intensity

$$I(\boldsymbol{k}) \propto \sum_i |\langle\psi_{\boldsymbol{k}}|H_{\mathrm{int}}|\psi_i\rangle|^2 \delta(E_{\mathrm{kin}} + |E_{\mathrm{bind,i}}| - \hbar\omega), \quad (2.37)$$

where E_{bind} is the binding energy of the orbital. Another way of looking at this expression is that the single-particle orbital appearing in Eq. (2.37) is the Dyson orbital [43]. The expression

$$M(\boldsymbol{k}) = \langle\psi_{\boldsymbol{k}}|H_{\mathrm{int}}|\psi_i\rangle \quad (2.38)$$

is called the photoemission matrix element.

2.4.2 The final state

To evaluate the matrix element, expressions are needed for both the initial and final state. We approximate the Dyson orbital introduced in Eq. (2.37) by a single Kohn-Sham orbital obtained from a DFT calculation for the initial state. This leaves the final state. In the simplest case, the final state is assumed to be a free particle state, i.e., a plane wave

$$|\psi_{\boldsymbol{k}}\rangle = |\boldsymbol{k}\rangle\,. \quad (2.39)$$

In this form the approach is known as photoemission orbital tomography (POT) [8]. It is the goal of this thesis to improve upon this simplest of approaches. A general expression for the single particle final state can be given by the LS equation

$$|\psi_{\boldsymbol{k}}\rangle = |\boldsymbol{k}\rangle + G_0^* V\,|\psi_{\boldsymbol{k}}\rangle\,, \quad (2.40)$$

where the complex conjugation of the Green function is needed to properly account for the boundary conditions [38, 40]. Since the plane-wave approximation (PAW) works surprisingly well, it is natural to assume that the Born approximation should be valid. This, however, is not the case [17], also see Chapter 4. The solution of the LS equation will be detailed in the chapters to come.

2.4.3 Three equivalent gauges

There are three different ways—so called "gauges"—to treat the interaction Hamiltonian appearing in the matrix element of the photoemission process. All three gauges should lead to the same value of the transition matrix element—provided that exact initial and final states are used for the evaluation [44, 45]. The three gauges are: length gauge ($\boldsymbol{Ar}$), velocity gauge ($\boldsymbol{Ap}$) and acceleration gauge ($\boldsymbol{A}\nabla V$), with the exact correspondence being[2]:

$$\langle \psi_{\boldsymbol{k}} | \boldsymbol{Ar} | \psi_i \rangle \propto \frac{1}{\omega} \langle \psi_{\boldsymbol{k}} | \boldsymbol{Ap} | \psi_i \rangle \tag{2.41}$$

and

$$\langle \psi_{\boldsymbol{k}} | \boldsymbol{A}\nabla V | \psi_i \rangle \propto \omega \langle \psi_{\boldsymbol{k}} | \boldsymbol{Ap} | \psi_i \rangle . \tag{2.42}$$

ω is the difference between the initial and final state energies, i.e. the photon frequency in units where $\hbar = 1$.

These expressions are usually derived in the presence of a purely local potential. Let us derive the form of the length gauge for a Hamiltonian containing a local potential as an illustration. Starting from

$$[H, \boldsymbol{r}] \propto [\boldsymbol{p}^2, \boldsymbol{r}] \propto \boldsymbol{p}, \tag{2.43}$$

we obtain

$$\langle \psi_f | \boldsymbol{p} | \psi_{\text{in}} \rangle \propto \langle \psi_f | H\boldsymbol{r} | \psi_{\text{in}} \rangle - \langle \psi_f | \boldsymbol{r}H | \psi_{\text{in}} \rangle . \tag{2.44}$$

In the first term H acts to the left, on ψ_f, while in the second term it acts to the right, on ψ_{in}. This gives

$$\langle \psi_f | \boldsymbol{p} | \psi_{\text{in}} \rangle \propto (E_f - E_{\text{in}}) \langle \psi_f | \boldsymbol{r} | \psi_{\text{in}} \rangle = \omega \langle \psi_f | \boldsymbol{r} | \psi_{\text{in}} \rangle \tag{2.45}$$

A nonlocal potential V_{nl} invalidates this equivalence as the commutation relation in Eq (2.43) would also contain the nonlocal potential term. The nonlocal potential would also appear in the interaction Hamiltonians of the length and acceleration gauges. This makes them somewhat impractical to use, and we will only use them in Chapter 4 where we are dealing with a purely local potential.

[2] Constant factors have been dropped for the sake of simplicity.

2.5 Appendix: some useful properties of spherical harmonics

Here, we collect some properties of spherical harmonics. The addition theorem [46] relates the angle between the vectors $\boldsymbol{r}$ and $\boldsymbol{k}$ to the angle θ between them:

$$\begin{aligned} Y_{l0}(\theta) = \sqrt{\frac{2l+1}{2\pi^2}} P_l(\cos\theta) =& \sqrt{\frac{4\pi}{2l+1}} \sum_{m=-l}^{l} Y_{lm}(\hat{\boldsymbol{k}}) Y^*_{lm}(\hat{\boldsymbol{r}}) \\ =& \sqrt{\frac{4\pi}{2l+1}} \sum_{m=-l}^{l} Y^*_{lm}(\hat{\boldsymbol{k}}) Y_{lm}(\hat{\boldsymbol{r}}), \end{aligned} \tag{2.46}$$

From this a simple but helpful formula can be derived:

$$\begin{aligned} \int d\hat{\boldsymbol{r}} Y_{l0}(\theta) Y_{l'm'}(\hat{\boldsymbol{r}}) =& \sqrt{\frac{4\pi}{2l+1}} \sum_{m=-l}^{l} Y_{lm}(\hat{\boldsymbol{k}}) \int d\hat{\boldsymbol{r}} Y^*_{lm}(\hat{\boldsymbol{r}}) Y_{l'm'}(\hat{\boldsymbol{r}}) \\ =& \sqrt{\frac{4\pi}{2l+1}} \sum_{m=-l}^{l} Y_{lm}(\hat{\boldsymbol{k}}) \delta_{ll'} \delta_{mm'}. \end{aligned} \tag{2.47}$$

Using this relation, we can furthermore write

$$\begin{aligned} \sum_{l'm'} Y^*_{l'm'}(\hat{\boldsymbol{r}}') \int d\hat{\boldsymbol{r}} Y_{l0}(\theta) Y_{l'm'}(\hat{\boldsymbol{r}}) =& \sqrt{\frac{4\pi}{2l+1}} \sum_{l'm'm} Y^*_{l'm'}(\hat{\boldsymbol{r}}') Y_{lm}(\hat{\boldsymbol{k}}) \delta_{ll'} \delta_{mm'} \\ =& \sqrt{\frac{4\pi}{2l+1}} \sum_{m} Y^*_{lm}(\hat{\boldsymbol{r}}') Y_{lm}(\hat{\boldsymbol{k}}). \end{aligned} \tag{2.48}$$

And, finally

$$\sum_{l'm'} Y^*_{l'm'}(\hat{\boldsymbol{r}}') \int d\hat{\boldsymbol{r}} Y_{l0}(\theta) Y_{l'm'}(\hat{\boldsymbol{r}}) = Y_{l0}(\theta'), \tag{2.49}$$

where θ' is the angle between $\boldsymbol{k}$ and $\boldsymbol{r}'$. Complex conjugation gives the equally valid form

$$\sum_{l'm'} Y_{l'm'}(\hat{\boldsymbol{r}}') \int d\hat{\boldsymbol{r}} Y_{l0}(\theta) Y^*_{l'm'}(\hat{\boldsymbol{r}}) = Y_{l0}(\theta'). \tag{2.50}$$

Chapter 3

Wavevector space formulation

We start with the formulation of the Lippmann-Schwinger (LS) equation in wavevector space that is geared toward describing the photoemission of periodic systems. The systems of interest range from 2D materials, such as graphene, to free-standing molecular surface layers to molecular surface layers deposited on metal substrates.

In the end, the methods in this chapter did not prove successful, and they are only included here because we spent a large amount of time on them and the derivations should be correct in principle. At this stage it is also not entirely clear whether some potential errors in the actual implementation of the code might be at fault or the entire approach is flawed. Maybe there is still some merit to these methods and so we briefly describe them. In the meantime a paper appeared which introduced a similar method [18]. Additionally, another group is actively pursuing this approach [47]. These approaches are superior to our approaches because they reduced the problem to the 1d Green function for the spatial component perpendicular to the surface, while we laboriously dragged the full 3d Green function along. They managed to do so by cleverly rewriting the Lippmann-Schwinger equation. As described in Chapter 3.3, this means that our approaches are plagued by the singularities of the 3d Green function, which are, however, absent in the 1d Green function. For these reasons, and to keep the unnecessary parts short, we refrain from showing failed attempts.

3.1 Approach 1: repeated slab approach for the final state

Most metal surfaces look very similar to their bulk truncated versions, except that the distance between layers changes [48]. This change in distance, however, is limited

to the first couple of layers, say two or three, after which the layer distance quickly reaches its bulk value. This gives rise to the "repeated slab" approach: only a handful of layers are included into a plane wave DFT calculation, and the first 2 or 3 layers are allowed to relax into their new equilibrium position, while the lower layers are fixed at their bulk value. The setup must also include sufficient vacuum on the surface side of the metal. The rationale behind this approach is that states of the slab will quickly decay into the vacuum region, thereby preventing interactions with the slab's periodic replica. In this approach, the potential is periodic in all three dimensions, even though a surface is only periodic in two dimensions. As a consequence, it can be expanded into plane waves [49]

$$V(\boldsymbol{r}) = \sum_{\boldsymbol{G}} V_{\boldsymbol{G}} e^{i\boldsymbol{G}\boldsymbol{r}}, \tag{3.1}$$

where $\boldsymbol{G}$ is a reciprocal lattice vector of the slab's unit cell. Next, we describe the repeated slab approach for the photoelectron final state.

The Lippmann-Schwinger integral equation $|\psi_{\boldsymbol{k}}\rangle = |\boldsymbol{k}\rangle + G_0 V |\psi_{\boldsymbol{k}}\rangle$ may also be solved in momentum space [38]

$$\psi_{\boldsymbol{k}}(\boldsymbol{k}') \equiv \langle \boldsymbol{k}'|\psi_{\boldsymbol{k}}\rangle = \delta_{\boldsymbol{k}',\boldsymbol{k}} + \langle \boldsymbol{k}'| G_0 V |\psi_{\boldsymbol{k}}\rangle , \tag{3.2}$$

where $\boldsymbol{k}$ is the photoelectron wavevector. The state $|\boldsymbol{k}\rangle$ denotes a plane wave state. The scalar product $\langle \boldsymbol{k}'|\boldsymbol{k}\rangle$ can be treated as a Kronecker delta function if the whole system is considered to be in a large box with periodic boundary conditions. Inserting a complete momentum basis into the second term leads to

$$\begin{aligned} \langle \boldsymbol{k}'| G_0 V |\psi_{\boldsymbol{k}}\rangle =& \sum_{\boldsymbol{k}_1} \langle \boldsymbol{k}'| G_0 |\boldsymbol{k}_1\rangle \langle \boldsymbol{k}_1| V |\psi_{\boldsymbol{k}}\rangle \\ =& G_0(k'; k) \langle \boldsymbol{k}'| V |\psi_{\boldsymbol{k}}\rangle , \end{aligned} \tag{3.3}$$

where the free particle Green function in momentum space is given by [38]

$$G_0(q; k) = \frac{2}{k^2 - q^2 + i\epsilon}. \tag{3.4}$$

In this expression, k denotes the fixed wavenumber of the photoelectron—or, in other words, just a parameter—while q is a genuine variable. The semicolon in $G_0(q; k)$ serves as a reminder of this distinction. The Green function depends on two arguments in real space—or their difference, to be more precise—but is diagonal in

reciprocal space. The $i\epsilon$ term in the denominator will be addressed later. Moving on with the evaluation of $\langle \boldsymbol{k}' | \, G_0 V \, | \psi_{\boldsymbol{k}} \rangle$ leads to

$$\begin{aligned} \langle \boldsymbol{k}' | \, G_0 V \, | \psi_{\boldsymbol{k}} \rangle =& G_0(k'; k) \, \langle \boldsymbol{k}' | \, V \, | \psi_{\boldsymbol{k}} \rangle \\ =& G_0(k'; k) \sum_{\boldsymbol{k}_1} \langle \boldsymbol{k}' | \, V \, | \boldsymbol{k}_1 \rangle \, \langle \boldsymbol{k}_1 | \, | \psi_{\boldsymbol{k}} \rangle \\ =& G_0(k'; k) \sum_{\boldsymbol{k}_1} V(\boldsymbol{k}', \boldsymbol{k}_1) \psi_{\boldsymbol{k}}(\boldsymbol{k}_1). \end{aligned} \tag{3.5}$$

Exploiting the periodicity of the local potential V, which is diagonal in real space but not reciprocal space, permits the following simplification for $V(\boldsymbol{k}', \boldsymbol{k}_1)$ [49]

$$\begin{aligned} V(\boldsymbol{k}', \boldsymbol{k}_1) = \langle k' | \, V \, | k_1 \rangle &= \frac{1}{\Omega} \int d^3 r V(\boldsymbol{r}) e^{i(\boldsymbol{k}_1 - \boldsymbol{k}')\boldsymbol{r}} \\ &= \frac{1}{\Omega} \sum_{\boldsymbol{G}} V_{\boldsymbol{G}} \int d^3 r e^{i(\boldsymbol{k}_1 + \boldsymbol{G} - \boldsymbol{k}')\boldsymbol{r}} = \sum_{\boldsymbol{G}} V_{\boldsymbol{G}} \delta_{\boldsymbol{k}_1 + \boldsymbol{G}, \boldsymbol{k}'}, \end{aligned} \tag{3.6}$$

where Ω denotes the volume of the large periodic box. With this, the above expression yields

$$\begin{aligned} \langle \boldsymbol{k}' | \, G_0 V \, | \psi_{\boldsymbol{k}} \rangle &= G_0(k'; k) \sum_{\boldsymbol{G}} V_{\boldsymbol{G}} \sum_{\boldsymbol{k}_1} \psi_{\boldsymbol{k}}(\boldsymbol{k}_1) \delta_{\boldsymbol{k}_1 + \boldsymbol{G}, \boldsymbol{k}'} \\ &= G_0(k'; k) \sum_{\boldsymbol{G}} V_{\boldsymbol{G}} \psi_{\boldsymbol{k}}(\boldsymbol{k}' - \boldsymbol{G}), \end{aligned} \tag{3.7}$$

or including the plane wave term

$$\psi_{\boldsymbol{k}}(\boldsymbol{k}') = \delta_{\boldsymbol{k}', \boldsymbol{k}} + G_0(k'; k) \sum_{\boldsymbol{G}} V_{\boldsymbol{G}} \psi_{\boldsymbol{k}}(\boldsymbol{k}' - \boldsymbol{G}). \tag{3.8}$$

In this form only values of $\boldsymbol{k}'$ that differ from $\boldsymbol{k}$ by reciprocal lattice vectors give a nonvanishing contribution (i.e. $\boldsymbol{k}' \stackrel{!}{=} \boldsymbol{k} + \boldsymbol{G}$). This can be established perturbatively: only terms with delta functions of the form $\delta_{\boldsymbol{k}', \boldsymbol{G}'}$ will appear in the expansion of $\psi_{\boldsymbol{k}}$. Thus, the only nonvanishing components are of the form $\psi_{\boldsymbol{k}}(\boldsymbol{k} + \boldsymbol{G})$:

$$\begin{aligned} \psi_{\boldsymbol{k}}(\boldsymbol{k} + \boldsymbol{G}) &= \delta_{\boldsymbol{G}, 0} + G_0(\boldsymbol{k} + \boldsymbol{G}) \sum_{\boldsymbol{G}'} V_{\boldsymbol{G}'} \psi_{\boldsymbol{k}}(\boldsymbol{k} + \boldsymbol{G} - \boldsymbol{G}') \\ &= \delta_{\boldsymbol{G}, 0} + G_0(\boldsymbol{k} + \boldsymbol{G}) \sum_{\boldsymbol{G}''} V_{\boldsymbol{G} - \boldsymbol{G}''} \psi_{\boldsymbol{k}}(\boldsymbol{k} + \boldsymbol{G}''), \end{aligned} \tag{3.9}$$

or

$$\sum_{\boldsymbol{G}''}(\delta_{\boldsymbol{G},\boldsymbol{G}''} - G_0(\boldsymbol{k}+\boldsymbol{G})V_{\boldsymbol{G}-\boldsymbol{G}''})\psi_{\boldsymbol{k}}(\boldsymbol{k}+\boldsymbol{G}'') = \delta_{\boldsymbol{G},0}. \tag{3.10}$$

The number of reciprocal lattice vectors has to be truncated, so a reciprocal lattice vector that is larger than the cutoff $\boldsymbol{G}_n$ gives only a negligible contribution. Crucially, we assume that $\psi_{\boldsymbol{k}}(\boldsymbol{k}+\boldsymbol{G})$ decreases faster than $V_{\boldsymbol{G}}$, which means that $\psi_{\boldsymbol{k}}(\boldsymbol{k}+\boldsymbol{G})$ has fewer components than $V_{\boldsymbol{G}}$. With this, Eq. (3.10) is a matrix equation of the form $M\boldsymbol{\psi} = \boldsymbol{b}$, with the following definitions:

$$\begin{aligned} \boldsymbol{\psi} &= (\psi_{\boldsymbol{k}}(\boldsymbol{k}), \psi_{\boldsymbol{k}}(\boldsymbol{k}+\boldsymbol{G}_1), \ldots, \psi_{\boldsymbol{k}}(\boldsymbol{k}+\boldsymbol{G}_n), \\ \boldsymbol{b} &= (\delta_{0,0}, \delta_{\boldsymbol{G}_1,0}, \ldots, \delta_{\boldsymbol{G}_n,0}) \text{ and} \\ M_{\boldsymbol{G},\boldsymbol{G}''} &= \delta_{\boldsymbol{G},\boldsymbol{G}''} - G_0(\boldsymbol{k}+\boldsymbol{G})V_{\boldsymbol{G}-\boldsymbol{G}''}. \end{aligned} \tag{3.11}$$

Had we not made the assumption of placing the system into a large periodic box we would have arrived at the same Eq. (3.8), except with Dirac delta functions in place of Kronecker deltas. The Dirac delta functions must be replaced by an appropriate continuous representation for a numerical evaluation.

3.2 Approach 2: taking the surface periodicity into account

The slab approach may be sufficient for the initial state calculation but it is probably not viable for the final state, as there is no way to obtain a spherically outgoing wave with periodic boundary conditions. Instead, the lack of periodicity in the direction perpendicular to the surface must be included in the description upfront. This is also the approach taken in [18], where, in contrast to our approach, the authors were able to use the 1d Green function instead of the full 3d Green function. Thus, the expansion of the Kohn-Sham potential is only periodic in the in-plane coordinate $\boldsymbol{r}_\parallel$ [48]:

$$V(\boldsymbol{r}) = \sum_{\boldsymbol{G}_\parallel} V_{\boldsymbol{G}_\parallel}(z)e^{i\boldsymbol{G}_\parallel \boldsymbol{r}_\parallel}, \tag{3.12}$$

where z is the coordinate normal to the surface. Similarly, the final state is given by

$$\psi_{\boldsymbol{k}}(\boldsymbol{r}) = e^{i\boldsymbol{q}_\parallel \boldsymbol{r}_\parallel} \sum_{\boldsymbol{G}_\parallel} u_{\boldsymbol{k}_\parallel \boldsymbol{G}_\parallel}(z)e^{i\boldsymbol{G}_\parallel \boldsymbol{r}_\parallel}, \tag{3.13}$$

where $\boldsymbol{q}_\parallel$ is the surface Brillouin zone component of $\boldsymbol{k}_\parallel$—i.e., $\boldsymbol{k}_\parallel = \boldsymbol{q}_\parallel + \Delta\boldsymbol{G}_\parallel$—and is conserved in the photoemission process. The coefficients $u_{\boldsymbol{k}_\parallel \boldsymbol{G}_\parallel}(z)$ may be found

implicitly by inserting this ansatz into the LS equation

$$\psi_{\boldsymbol{k}}(\boldsymbol{r}) = \phi_{\boldsymbol{k}}(\boldsymbol{r}) + \int d^3r' G_0(\boldsymbol{r}, \boldsymbol{r}') V(\boldsymbol{r}') \psi_{\boldsymbol{k}}(\boldsymbol{r}'). \tag{3.14}$$

Multiplying the final state by $e^{-i\boldsymbol{G}\boldsymbol{r}}$, where $\boldsymbol{G} = (\boldsymbol{q}_\parallel + \boldsymbol{G}_\parallel, k_\perp)$ with $k_\perp$ being arbitrary, and integrating over $\boldsymbol{r}$ projects out the Fourier transform of $u_{\boldsymbol{k}_\parallel \boldsymbol{G}_\parallel}(z)$ with respect to z, i.e.,

$$\int d^3r \psi_{\boldsymbol{k}}(\boldsymbol{r}) e^{-i\boldsymbol{G}\boldsymbol{r}} = A \int dz u_{\boldsymbol{k}_\parallel \boldsymbol{G}_\parallel}(z) e^{-ik_\perp z} \equiv A u_{\boldsymbol{k}_\parallel \boldsymbol{G}_\parallel}(k_\perp), \tag{3.15}$$

where the sample area A will drop out of the calculation eventually. We follow the standard, and somewhat sloppy, convention of not introducing another symbol for the Fourier transform. So, instead of denoting the Fourier transform as $\tilde{u}_{\boldsymbol{k}_\parallel \boldsymbol{G}_\parallel}(k_\perp)$ we simply write it as $u_{\boldsymbol{k}_\parallel \boldsymbol{G}_\parallel}(k_\perp)$. It is clear from the function argument whether the function is in real or Fourier space. On the right-hand side of the LS equation, the plane wave term gives the usual Kronecker delta function $A\delta_{\boldsymbol{k},\boldsymbol{G}}$. The second term

$$\int d^3r d^3r' G_0(\boldsymbol{r}, \boldsymbol{r}') e^{-i\boldsymbol{G}\boldsymbol{r}} V(\boldsymbol{r}') \psi_{\boldsymbol{k}}(\boldsymbol{r}') \tag{3.16}$$

can be simplified analytically as well

$$\int d^3r G_0(\boldsymbol{r}, \boldsymbol{r}') e^{-i\boldsymbol{G}\boldsymbol{r}} = -\frac{1}{2\pi} \int d^3r \frac{e^{ik|\boldsymbol{r}-\boldsymbol{r}'|}}{|\boldsymbol{r}-\boldsymbol{r}'|} e^{-i\boldsymbol{G}\boldsymbol{r}}. \tag{3.17}$$

The integral can be solved easily by transforming to spherical coordinates

$$\int d^3r \frac{e^{ik|\boldsymbol{r}-\boldsymbol{r}'|}}{|\boldsymbol{r}-\boldsymbol{r}'|} e^{-i\boldsymbol{G}\boldsymbol{r}} = e^{-i\boldsymbol{G}\boldsymbol{r}'} \int d^3\rho \frac{e^{ik\rho}}{\rho} e^{-i\boldsymbol{G}\boldsymbol{\rho}} = 2\pi e^{-i\boldsymbol{G}\boldsymbol{r}'} \int d\rho d(\cos\theta) e^{ik\rho} \rho e^{-iG\rho\cos\theta}. \tag{3.18}$$

The remaining integrals are elementary

$$\int d\rho d(\cos\theta) e^{ik\rho} \rho e^{-iG\rho\cos\theta} = \frac{1}{-iG} \int d\rho e^{ik\rho} (e^{-iG\rho} - e^{iG\rho}) = \frac{1}{iG} \left(\frac{1}{i(k-G)} - \frac{1}{i(k+G)} \right), \tag{3.19}$$

where, as in standard scattering theory accounts [38], k is assumed to contain a small imaginary part $i\epsilon$ to remove the indeterminacy from the integrand at infinity (see later in this chapter for more details). Collecting terms leads to

$$\int d\rho d(\cos\theta) e^{ik\rho} \rho e^{-iG\rho\cos\theta} = \frac{2}{G^2 - k^2}. \tag{3.20}$$

So, in the end

$$\int d^3r G_0(\boldsymbol{r},\boldsymbol{r}')e^{-i\boldsymbol{G}\boldsymbol{r}} = \frac{2}{k^2-G^2}e^{-i\boldsymbol{G}\boldsymbol{r}'}. \tag{3.21}$$

Finally, moving on to the integral over $\boldsymbol{r}'$

$$\int d^3r d^3r' G_0(\boldsymbol{r},\boldsymbol{r}')e^{-i\boldsymbol{G}\boldsymbol{r}}V(\boldsymbol{r}')\psi_{\boldsymbol{k}}(\boldsymbol{r}') = \frac{2}{k^2-G^2}\int d^3r' e^{-i\boldsymbol{G}\boldsymbol{r}'}V(\boldsymbol{r}')\psi_{\boldsymbol{k}}(\boldsymbol{r}'). \tag{3.22}$$

Inserting the expansions for $V(\boldsymbol{r})$ and $\psi_{\boldsymbol{k}}(\boldsymbol{r})$

$$\int d^3r' e^{-i\boldsymbol{G}\boldsymbol{r}'}V(\boldsymbol{r}')\psi_{\boldsymbol{k}}(\boldsymbol{r}') = \sum_{\boldsymbol{G}_{\parallel,1},\boldsymbol{G}_{\parallel,2}}\int dz u_{\boldsymbol{k}_\parallel \boldsymbol{G}_{\parallel,1}}(z')V_{\boldsymbol{G}_{\parallel,2}}(z')e^{-ik_\perp z'}\int d^2r_\parallel e^{-i\boldsymbol{G}_\parallel \boldsymbol{r}'_\parallel}e^{i(\boldsymbol{G}_{\parallel,1}+\boldsymbol{G}_{\parallel,2})\boldsymbol{r}'_\parallel}. \tag{3.23}$$

The integral over the parallel component gives the two-dimensional wave vector conservation

$$\int d^2r_\parallel e^{-i\boldsymbol{G}_\parallel \boldsymbol{r}'_\parallel}e^{i(\boldsymbol{G}_{\parallel,1}+\boldsymbol{G}_{\parallel,2})\boldsymbol{r}'_\parallel} = A\delta_{\boldsymbol{G}_\parallel,\boldsymbol{G}_{\parallel,1}+\boldsymbol{G}_{\parallel,2}}. \tag{3.24}$$

So,

$$\int d^3r' e^{-i\boldsymbol{G}\boldsymbol{r}'}V(\boldsymbol{r}')\psi_{\boldsymbol{k}}(\boldsymbol{r}') = A\sum_{\boldsymbol{G}_{\parallel,1}}\int dz u_{\boldsymbol{k}_\parallel \boldsymbol{G}_{\parallel,1}}(z')V_{\boldsymbol{G}_\parallel-\boldsymbol{G}_{\parallel,1}}(z')e^{-ik_\perp z'}. \tag{3.25}$$

Putting everything together, the LS equation reads

$$u_{\boldsymbol{k}_\parallel \boldsymbol{G}_\parallel}(k_\perp) = \delta_{\boldsymbol{k},\boldsymbol{G}} + \frac{2}{k^2-G^2}\sum_{\boldsymbol{G}_{\parallel,1}}\int dz u_{\boldsymbol{k}_\parallel \boldsymbol{G}_{\parallel,1}}(z)V_{\boldsymbol{G}_\parallel-\boldsymbol{G}_{\parallel,1}}(z)e^{-ik_\perp z}. \tag{3.26}$$

Inserting the Fourier transform on the right-hand side, that is, solving the whole system in wave vector space, gives

$$u_{\boldsymbol{k}_\parallel \boldsymbol{G}_\parallel}(k_\perp) = \delta_{\boldsymbol{k},\boldsymbol{G}} + \frac{2}{k^2-G^2}\sum_{\boldsymbol{G}_{\parallel,1}}\int dz V_{\boldsymbol{G}_\parallel-\boldsymbol{G}_{\parallel,1}}(z)e^{-ik_\perp z}\int \frac{dk}{2\pi}e^{ikz}u_{\boldsymbol{k}_\parallel \boldsymbol{G}_{\parallel,1}}(k). \tag{3.27}$$

With the abbreviation

$$V_{\boldsymbol{G}_\parallel-\boldsymbol{G}_{\parallel,1}}(k_\perp - k) = \int dz V_{\boldsymbol{G}_\parallel-\boldsymbol{G}_{\parallel,1}}(z)e^{-i(k_\perp-k)z} \tag{3.28}$$

the above equation becomes

$$u_{\boldsymbol{k}_\parallel \boldsymbol{G}_\parallel}(k_\perp) = \delta_{\boldsymbol{k},\boldsymbol{G}} + \frac{2}{k^2-G^2}\sum_{\boldsymbol{G}_{\parallel,1}}\int \frac{dk}{2\pi}V_{\boldsymbol{G}_\parallel-\boldsymbol{G}_{\parallel,1}}(k_\perp-k)u_{\boldsymbol{k}_\parallel \boldsymbol{G}_{\parallel,1}}(k). \tag{3.29}$$

In order to solve the above equation for $u_{\boldsymbol{k}_\parallel \boldsymbol{G}_\parallel}(k_\perp)$ we discretize the integral over k,

$$u_{\boldsymbol{k}_\parallel \boldsymbol{G}_\parallel}(k_\perp) = \delta_{\boldsymbol{k},\boldsymbol{G}} + \frac{2}{k^2 - G^2} \sum_{\boldsymbol{G}_{\parallel,1} i} \frac{w_i}{2\pi} V_{\boldsymbol{G}_\parallel - \boldsymbol{G}_{\parallel,1}}(k_\perp - k_i) u_{\boldsymbol{k}_\parallel \boldsymbol{G}_{\parallel,1}}(k_i), \tag{3.30}$$

with the integration weights w_i. In this approach the linear system of equations to be solved thus is

$$\sum_{\boldsymbol{G}_{\parallel,1} i} \left(\delta_{\boldsymbol{G}_\parallel,\boldsymbol{G}_{\parallel,1}} \delta_{k_\perp,k_i} + \frac{2}{G^2 - k^2} \frac{w_i}{2\pi} V_{\boldsymbol{G}_\parallel - \boldsymbol{G}_{\parallel,1}}(k_\perp - k_i) \right) u_{\boldsymbol{k}_\parallel \boldsymbol{G}_{\parallel,1}}(k_i) = \delta_{\boldsymbol{k},\boldsymbol{G}}. \tag{3.31}$$

In a more compact notation the above system is

$$\sum_{\boldsymbol{G}_i} M_{\boldsymbol{G},\boldsymbol{G}_i} \Psi_{\boldsymbol{G}_i} = \Phi_{\boldsymbol{G}}, \tag{3.32}$$

where

$$M_{\boldsymbol{G},\boldsymbol{G}_i} = G_0(G) V_{\boldsymbol{G}-\boldsymbol{G}_i}. \tag{3.33}$$

The changes compared to the repeated slab approach are rather minor and may have been foreseen. The main difference is that the discrete variable G_z is replaced by the continuous $k_\perp$. Numerically, this necessitates a finer mesh and hence increases the required computer memory.

Once the coefficients have been determined, the overlap and the matrix element with the initial state can be calculated rather simply. For that, the initial state also has to be expanded in a 2d basis:

$$\psi_{n\boldsymbol{q}_\parallel}(\boldsymbol{r}) = e^{i\boldsymbol{q}_\parallel \boldsymbol{r}_\parallel} \sum_{\boldsymbol{G}_\parallel} c_{n\boldsymbol{q}_\parallel \boldsymbol{G}_\parallel}(z) e^{i\boldsymbol{G}_\parallel \boldsymbol{r}_\parallel}. \tag{3.34}$$

The overlap is given by

$$\begin{aligned} \langle \psi_{\boldsymbol{k}} | \psi_{n\boldsymbol{q}_\parallel} \rangle &= \sum_{\boldsymbol{G}_{\parallel,1} \boldsymbol{G}_{\parallel,2}} \int dz u^*_{\boldsymbol{k}_\parallel \boldsymbol{G}_{\parallel,1}}(z) c_{n\boldsymbol{q}_\parallel G_{\parallel,2}}(z) \int d^2 r_\parallel e^{i(\boldsymbol{G}_{\parallel,2} - \boldsymbol{G}_{\parallel,1})\boldsymbol{r}_\parallel} \\ &= \sum_{\boldsymbol{G}_\parallel} \int dz u^*_{\boldsymbol{k}_\parallel \boldsymbol{G}_\parallel}(z) c_{n\boldsymbol{q}_\parallel \boldsymbol{G}_\parallel}(z) \\ &= \sum_{\boldsymbol{G}_\parallel} \int dk u^*_{\boldsymbol{k}_\parallel \boldsymbol{G}_\parallel}(k) c_{n\boldsymbol{q}_\parallel \boldsymbol{G}_\parallel}(k), \end{aligned} \tag{3.35}$$

and should be vanishingly small, which may be used as a check of the calculation. In contrast, the overlap between the initial state and plane wave final state will, in general, not vanish. The overlap in the plane-wave approximation for the final state can be determined from

$$\begin{aligned}\langle \boldsymbol{k}|\psi_{n\boldsymbol{q}_\parallel}\rangle =& \int dz e^{-ik_z z} c_{n\boldsymbol{q}_\parallel \boldsymbol{G}_\parallel}(z) \sum_{\boldsymbol{G}_\parallel} \int dr_\parallel e^{i(\boldsymbol{q}_\parallel+\boldsymbol{G}_\parallel-\boldsymbol{k}_\parallel)\boldsymbol{r}_\parallel} \\ =& \int dz e^{-ik_z z} c_{n\boldsymbol{q}_\parallel \Delta\boldsymbol{G}_\parallel}(z) \\ =& c_{n\boldsymbol{q}_\parallel \Delta\boldsymbol{G}_\parallel}(k_z),\end{aligned} \tag{3.36}$$

where $|\boldsymbol{k}\rangle$ denotes a plane wave and should not be confused with the LS final state $|\psi_{\boldsymbol{k}}\rangle$.

The matrix element can be determined similarly

$$\langle \psi_{\boldsymbol{k}}|\boldsymbol{p}|\psi_{n\boldsymbol{q}_\parallel}\rangle = \sum_{\boldsymbol{G}_{\parallel,1}\boldsymbol{G}_{\parallel,2}} \int dz u^*_{\boldsymbol{k}_\parallel \boldsymbol{G}_{\parallel,1}}(z) \int d^2 r_\parallel e^{-i(\boldsymbol{G}_{\parallel,1}+\boldsymbol{q}_\parallel)\boldsymbol{r}_\parallel} \boldsymbol{p} c_{n\boldsymbol{q}_\parallel \boldsymbol{G}_{\parallel,2}}(z) e^{i(\boldsymbol{G}_{\parallel,2}+\boldsymbol{q}_\parallel)\boldsymbol{r}_\parallel}. \tag{3.37}$$

The parallel component of the momentum just acts on the plane wave part and yields

$$\begin{aligned}\langle \psi_{\boldsymbol{k}}|\boldsymbol{p}_\parallel|\psi_{n\boldsymbol{q}_\parallel}\rangle =& \sum_{\boldsymbol{G}_\parallel} (\boldsymbol{G}_\parallel+\boldsymbol{q}_\parallel) \int dz u^*_{\boldsymbol{k}_\parallel \boldsymbol{G}_\parallel}(z) c_{n\boldsymbol{q}_\parallel \boldsymbol{G}_\parallel}(z) \\ =& \sum_{\boldsymbol{G}_\parallel} (\boldsymbol{G}_\parallel+\boldsymbol{q}_\parallel) \int dk u^*_{\boldsymbol{k}_\parallel \boldsymbol{G}_\parallel}(k) c_{n\boldsymbol{q}_\parallel \boldsymbol{G}_\parallel}(k).\end{aligned} \tag{3.38}$$

The perpendicular component is given by

$$\begin{aligned}\langle \psi_{\boldsymbol{k}}|p_\perp|\psi_{n\boldsymbol{q}_\parallel}\rangle =& -i \sum_{\boldsymbol{G}_\parallel} \int dz u^*_{\boldsymbol{k}_\parallel \boldsymbol{G}_\parallel}(z) \frac{\partial}{\partial z} c_{n\boldsymbol{q}_\parallel \boldsymbol{G}_\parallel}(z) \\ =& \sum_{\boldsymbol{G}_\parallel} \int dk u^*_{\boldsymbol{k}_\parallel \boldsymbol{G}_\parallel}(k) k c_{n\boldsymbol{q}_\parallel \boldsymbol{G}_\parallel}(k).\end{aligned} \tag{3.39}$$

In the plane wave case, the intensity simplifies to

$$\begin{aligned}\langle \boldsymbol{k}|\boldsymbol{p}_\parallel|\psi_{n\boldsymbol{q}_\parallel}\rangle =& (\Delta\boldsymbol{G}_\parallel+\boldsymbol{q}_\parallel) \int dz e^{-ik_z z} c_{n\boldsymbol{q}_\parallel \Delta\boldsymbol{G}_\parallel}(z) = \boldsymbol{k}_\parallel \int dz e^{-ik_z z} c_{n\boldsymbol{q}_\parallel \Delta\boldsymbol{G}_\parallel}(z) \\ =& \boldsymbol{k}_\parallel c_{n\boldsymbol{q}_\parallel \Delta\boldsymbol{G}_\parallel}(k_z)\end{aligned} \tag{3.40}$$

and

$$\begin{aligned}\langle \boldsymbol{k}|p_\perp|\psi_{n\boldsymbol{q}_\parallel}\rangle =& -i\int dz e^{-ik_z z}\frac{\partial}{\partial z}c_{n\boldsymbol{q}_\parallel\Delta\boldsymbol{G}_\parallel}(z)\\ =& k_z c_{n\boldsymbol{q}_\parallel\Delta\boldsymbol{G}_\parallel}(k_z),\end{aligned} \tag{3.41}$$

respectively. Or, in summary

$$\langle \boldsymbol{k}|\boldsymbol{p}|\psi_{n\boldsymbol{q}_\parallel}\rangle = \boldsymbol{k}c_{n\boldsymbol{q}_\parallel\Delta\boldsymbol{G}_\parallel}(k_z). \tag{3.42}$$

Including the nonlocal potential

The structure of the LS equation is the same as in Eq. (3.33), i.e.

$$\sum_{\boldsymbol{G}_i} M_{\boldsymbol{G},\boldsymbol{G}_i}\Psi_{\boldsymbol{G}_i} = \Phi_{\boldsymbol{G}}, \tag{3.43}$$

but the kernel, $M_{\boldsymbol{G},\boldsymbol{G}_i}$, needs to be generalized as follows

$$M_{\boldsymbol{G},\boldsymbol{G}_i} = G_0(G)(V_{\rm loc}(\boldsymbol{G}-\boldsymbol{G}_i) + V_{nl}(\boldsymbol{G},\boldsymbol{G}_i)). \tag{3.44}$$

Asymmetric damping

In a slightly different approach, the imaginary component of k has different values in the lower and upper half spaces. This should roughly account for the fact that damping is strong in the sample at kinetic energies of below 100 eV, with a typical mean free path of a couple of angstroms, while there should be no attenuation above the surface. Numerically, there still has to be a small imaginary component in k above the surface. In that approach, Eq. (3.19) is replaced by

$$\begin{aligned}\int d\rho d(\cos\theta)e^{ik\rho}\rho e^{-iG\rho\cos\theta} =& \frac{1}{-iG}\int d\rho\left(e^{i(k_1-G)\rho} - e^{i(k_2+G)\rho}\right) = \frac{1}{G}\left(\frac{1}{k_2+G} - \frac{1}{k_1-G}\right)\\ =& \frac{1}{G}\frac{2G-(k_1-k_2)}{(G+k_2)(G-k_1)}.\end{aligned} \tag{3.45}$$

k_1 and k_2 correspond to the damping in the upper and lower half spaces respectively. More specifically,

$$k_1 = k + i\epsilon_1 \tag{3.46}$$

and

$$k_2 = k + i\epsilon_2. \tag{3.47}$$

The case $G = 0$ must be considered separately. In this case, the above integral yields

$$\int d\rho d(\cos\theta) e^{ik\rho}\rho = -\left(\frac{1}{k_1^2} + \frac{1}{k_2^2}\right). \tag{3.48}$$

The LS equation in momentum space becomes

$$\sum_{\boldsymbol{G}_{\parallel,1} i} \left(\delta_{\boldsymbol{G}_\parallel,\boldsymbol{G}_{\parallel,1}}\delta_{k_\perp,k_i} + \frac{2}{G}\frac{G-(k_1-k_2)/2}{(G+k_2)(G-k_1)}\frac{w_i}{2\pi}V_{\boldsymbol{G}_\parallel-\boldsymbol{G}_{\parallel,1}}(k_\perp - k_i)\right) u_{\boldsymbol{k}_\parallel \boldsymbol{G}_{\parallel,1}}(k_i) = \delta_{\boldsymbol{k},\boldsymbol{G}}. \tag{3.49}$$

3.3 Removing the singularity in the Green function

The singularity of the Green function in Eq. (3.31) at $k = G$ must be avoided somehow in a numerical treatment. The singularity arises from using the 3d form of the Green function. There is no singularity in the 1d Green function used in [18]. In the following, we describe some possible approaches to remove the singularity.

3.3.1 Adding an imaginary part to the wavevector

The easiest way to remove the singularity would be to add an imaginary part to k or k^2. A glance at the free particle Green function in real space

$$G_0(R) \propto \frac{e^{ikR}}{R} \tag{3.50}$$

shows that adding an imaginary part to k would correspond to some kind of attenuation of the free particle propagation. The problem with this approach is that the damping should be highly anisotropic in real space, i.e., only relevant if the electron is close to the layer.

The imaginary part may also be added to k^2, which seems to be the most convenient option when dealing with the Green function in reciprocal space:

$$\frac{1}{G^2 - k^2} \to \frac{1}{G^2 - k^2 - i\epsilon}, \tag{3.51}$$

but of course it still could be added to just k here as well.

3.3.2 Isolating the singularity

It might be beneficial to rewrite the Green function term in k-space as

$$\frac{2}{G^2 - k^2} = \frac{1}{G}\left(\frac{1}{G+k} + \frac{1}{G-k}\right). \tag{3.52}$$

The first term is unproblematic, while the second diverges for $k = G$. Adding a small exponential to the wavevector k and splitting off real and imaginary parts yields

$$\frac{1}{G-k-i\epsilon} = \frac{G-k+i\epsilon}{(G-k)^2+\epsilon^2} = \frac{G-k}{(G-k)^2+\epsilon^2} + i\frac{\epsilon}{(G-k)^2+\epsilon^2}. \tag{3.53}$$

Even for very small values of ϵ the first term should vanish for $k = G$, while the second term furnishes a representation of the Dirac delta function [39]

$$i\frac{\epsilon}{(G-k)^2+\epsilon^2} = i\pi\delta(G-k). \tag{3.54}$$

Within this scheme, we work with the following replacement

$$\frac{2}{G^2-k^2} \to \frac{1}{G}\left(\frac{1}{G+k} + i\pi\delta(G-k)\right), \text{ for } k \approx G. \tag{3.55}$$

Different delta function representations should be tested. Ideally, the size of ϵ will not influence the result too much.

3.3.3 Averaging the Green function and the delta function

The denominator of the Green function can also be brought to the other side of the equation. In this case, the expression to be evaluated would be

$$(G^2 - k^2)\delta(\boldsymbol{G} - \boldsymbol{k}). \tag{3.56}$$

Averaging these term might yield a more reasonable result. Using some particular representation of the delta function, the above expression could be averaged.

3.4 Approach 3: treating the perpendicular component in real space

The derivation of Chapter 3.2 must be changed slightly to keep the z-dependence of the final state explicit. The projection is carried out only in the surface plane with

a factor of $e^{-i(\boldsymbol{G}_\parallel+\boldsymbol{q}_\parallel)\boldsymbol{r}_\parallel}$, that is

$$\int d^2r_\parallel \psi_{\boldsymbol{k}}(\boldsymbol{r})e^{-i\tilde{\boldsymbol{G}}_\parallel\boldsymbol{r}_\parallel} = \int d^2r_\parallel \phi_{\boldsymbol{k}}(\boldsymbol{r})e^{-i\tilde{\boldsymbol{G}}_\parallel\boldsymbol{r}_\parallel} + \int d^2r_\parallel d^3r' G_0(\boldsymbol{r},\boldsymbol{r}')e^{-i\tilde{\boldsymbol{G}}_\parallel\boldsymbol{r}_\parallel}V(\boldsymbol{r}')\psi_{\boldsymbol{k}}(\boldsymbol{r}'), \tag{3.57}$$

where $\tilde{\boldsymbol{G}}_\parallel = \boldsymbol{G}_\parallel + \boldsymbol{q}_\parallel$. Also, $\boldsymbol{k}_\parallel = \boldsymbol{q}_\parallel + \Delta\boldsymbol{G}_\parallel$. The first and second term yield

$$\int d^2r_\parallel \psi_{\boldsymbol{k}}(\boldsymbol{r})e^{-i\tilde{\boldsymbol{G}}_\parallel\boldsymbol{r}_\parallel} = Au_{\boldsymbol{k}_\parallel\boldsymbol{G}_\parallel}(z) \tag{3.58}$$

and

$$\int d^2r_\parallel \phi_{\boldsymbol{k}}(\boldsymbol{r})e^{-i\tilde{\boldsymbol{G}}_\parallel\boldsymbol{r}_\parallel} = A\delta_{\Delta\boldsymbol{G}_\parallel,\boldsymbol{G}_\parallel}e^{ik_z z} \tag{3.59}$$

respectively. The third term $\int d^2r_\parallel G_0(\boldsymbol{r},\boldsymbol{r}')e^{-i\tilde{\boldsymbol{G}}_\parallel\boldsymbol{r}_\parallel}$ is more challenging. It cannot be evaluated analytically[1] but the $\boldsymbol{r}'_\parallel$ dependence can be split off:

$$\int d^2r_\parallel G_0(\boldsymbol{r},\boldsymbol{r}')e^{-i\tilde{\boldsymbol{G}}_\parallel\boldsymbol{r}_\parallel} = -\frac{1}{2\pi}\int d^2r_\parallel \frac{e^{ik|\boldsymbol{r}-\boldsymbol{r}'|}}{|\boldsymbol{r}-\boldsymbol{r}'|}e^{-i\tilde{\boldsymbol{G}}_\parallel\boldsymbol{r}_\parallel} = -\frac{1}{2\pi}e^{-i\tilde{\boldsymbol{G}}_\parallel\boldsymbol{r}'_\parallel}\int d^2\rho_\parallel \frac{e^{ik\rho}}{\rho}e^{-i\tilde{\boldsymbol{G}}_\parallel\boldsymbol{\rho}_\parallel}. \tag{3.60}$$

The important point is that the integral does not depend on $\boldsymbol{r}'_\parallel$, i.e.

$$\int d^2r_\parallel G_0(\boldsymbol{r},\boldsymbol{r}')e^{-i\tilde{\boldsymbol{G}}_\parallel\boldsymbol{r}_\parallel} \equiv -\frac{1}{2\pi}e^{-i\tilde{\boldsymbol{G}}_\parallel\boldsymbol{r}'_\parallel}f_{\tilde{G}_\parallel}(z,z'), \tag{3.61}$$

where $f_{\tilde{G}_\parallel}(z,z')$ must be evaluated numerically. More specifically $f_{\tilde{G}_\parallel}(z,z')$ is given by

$$f_{\tilde{G}_\parallel}(z,z') = \int d^2\rho_\parallel \frac{e^{ik|\boldsymbol{\rho}_\parallel+(z-z')\boldsymbol{e}_z|}}{|\boldsymbol{\rho}_\parallel+(z-z')\boldsymbol{e}_z|}e^{-i\tilde{\boldsymbol{G}}_\parallel\boldsymbol{\rho}_\parallel}. \tag{3.62}$$

The two dimensional integral can be reduced to a one dimensional one by introducing cylindrical coordinates (denoted by ρ and ϕ)

$$f_{\tilde{G}_\parallel}(z,z') = \int d\rho d\phi \rho \frac{e^{ik\sqrt{\rho^2+(z-z')^2}}}{\sqrt{\rho^2+(z-z')^2}}e^{-i\tilde{G}_\parallel\rho\cos\phi}. \tag{3.63}$$

The integral over ϕ is an integral representation of the zeroth order Bessel function [46]

$$\int d\phi e^{-i\tilde{G}_\parallel\rho\cos\phi} = 2\pi J_0(-\tilde{G}_\parallel\rho) = 2\pi J_0(\tilde{G}_\parallel\rho). \tag{3.64}$$

[1]Maybe it can be done in cylindrical coordinates with the appropriate expression for the Green function in that coordinate system, but this seems to be very involved.

So

$$f_{\tilde{G}_\parallel}(z,z') = 2\pi \int d\rho\rho \frac{e^{ik\sqrt{\rho^2+(z-z')^2}}}{\sqrt{\rho^2+(z-z')^2}} J_0(\tilde{G}_\parallel \rho). \tag{3.65}$$

In addition $f_{\tilde{G}_\parallel}(z,z')$ depends only on $|z-z'|$, as may be seen from the above expression. This reduces the numerical load further.

With this, the third term can be simplified

$$\begin{aligned}
&\int d^2r_\parallel d^3r' G_0(\boldsymbol{r},\boldsymbol{r}') e^{-i\tilde{\boldsymbol{G}}_\parallel \boldsymbol{r}_\parallel} V(\boldsymbol{r}')\psi_{\boldsymbol{k}}(\boldsymbol{r}') = -\frac{c}{4\pi}\int d^3r' f_{\tilde{G}_\parallel}(z,z') e^{-i\tilde{\boldsymbol{G}}_\parallel \boldsymbol{r}'_\parallel} V(\boldsymbol{r}')\psi_{\boldsymbol{k}}(\boldsymbol{r}') \\
&= -\frac{1}{2\pi}\sum_{\boldsymbol{G}_{\parallel,1},\boldsymbol{G}_{\parallel,2}} \int dz' f_{\tilde{G}_\parallel}(z,z') V_{\boldsymbol{G}_{\parallel,2}}(z') u_{\boldsymbol{k}_\parallel \boldsymbol{G}_{\parallel,1}}(z') \int d^2r_\parallel e^{i\boldsymbol{r}_\parallel(\boldsymbol{G}_{\parallel,1}+\boldsymbol{G}_{\parallel,2}-\boldsymbol{G}_\parallel)} \\
&= -\frac{1}{2\pi}\sum_{\boldsymbol{G}_{\parallel,1},\boldsymbol{G}_{\parallel,2}} \int dz' f_{\tilde{G}_\parallel}(z,z') V_{\boldsymbol{G}_{\parallel,2}}(z') u_{\boldsymbol{k}_\parallel \boldsymbol{G}_{\parallel,1}}(z') A\delta_{\boldsymbol{G}_{\parallel,1}+\boldsymbol{G}_{\parallel,2},\boldsymbol{G}_\parallel} \\
&= -\frac{A}{2\pi}\sum_{\boldsymbol{G}_{\parallel,1}} \int dz' f_{\tilde{G}_\parallel}(z,z') V_{\boldsymbol{G}_\parallel-\boldsymbol{G}_{\parallel,1}}(z') u_{\boldsymbol{k}_\parallel \boldsymbol{G}_{\parallel,1}}(z').
\end{aligned} \tag{3.66}$$

In summary, the LS equation in this scheme reads

$$u_{\boldsymbol{k}_\parallel \boldsymbol{G}_\parallel}(z) = \delta_{\Delta\boldsymbol{G}_\parallel,\boldsymbol{G}_\parallel} e^{ik_z z} - \frac{1}{2\pi}\sum_{\boldsymbol{G}_{\parallel,1}} \int dz' f_{\tilde{G}_\parallel}(z,z') V_{\boldsymbol{G}_\parallel-\boldsymbol{G}_{\parallel,1}}(z') u_{\boldsymbol{k}_\parallel \boldsymbol{G}_{\parallel,1}}(z'). \tag{3.67}$$

On the vacuum side the upper limit of the integral over z', let's call it L, must be sufficiently large so that $V_{\boldsymbol{G}_\parallel-\boldsymbol{G}_{\parallel,1}}(z') \approx 0$ for $z' > L$. The potential, however, does not vanish in the bulk. So the lower limit of the integral must be chosen in such a way that the final state wavefunction itself becomes vanishingly small below that point. This can only be accomplished by including an artificial damping factor into the Green function.

Bearing the above considerations in mind, the discretization of the integral proceeds in the usual fashion:

$$\int_0^L dz' f_{\tilde{G}_\parallel}(z,z') V_{\boldsymbol{G}_\parallel-\boldsymbol{G}_{\parallel,1}}(z') u_{\boldsymbol{k}_\parallel \boldsymbol{G}_{\parallel,1}}(z') \approx \sum_j w_j f_{\tilde{G}_\parallel}(z,z_j) V_{\boldsymbol{G}_\parallel-\boldsymbol{G}_{\parallel,1}}(z_j) u_{\boldsymbol{k}_\parallel \boldsymbol{G}_{\parallel,1}}(z_j). \tag{3.68}$$

Evaluating the final state also for the discrete points z_i then gives the final form of the LS equation

$$u_{\boldsymbol{k}_\parallel \boldsymbol{G}_\parallel}(z_i) = \delta_{\Delta\boldsymbol{G}_\parallel,\boldsymbol{G}_\parallel} e^{ik_z z_i} - \frac{1}{2\pi}\sum_{\boldsymbol{G}_{\parallel,1},z_j} w_j f_{\tilde{G}_\parallel}(z_i,z_j) V_{\boldsymbol{G}_\parallel-\boldsymbol{G}_{\parallel,1}}(z_j) u_{\boldsymbol{k}_\parallel \boldsymbol{G}_{\parallel,1}}(z_j), \tag{3.69}$$

or

$$\sum_{\boldsymbol{G}_{\parallel,j},z_j} \left(\delta_{\boldsymbol{G}_\parallel,\boldsymbol{G}_{\parallel,j}} \delta_{z_i,z_j} + \frac{1}{2\pi} w_j f_{\tilde{G}_\parallel}(|z_i - z_j|) V_{\boldsymbol{G}_\parallel - \boldsymbol{G}_{\parallel,j}}(z_j) \right) u_{\boldsymbol{k}_\parallel \boldsymbol{G}_{\parallel,j}}(z_j) = \delta_{\Delta\boldsymbol{G}_\parallel,\boldsymbol{G}_\parallel} e^{ik_z z_i}. \tag{3.70}$$

In an horrible abuse of notation the above system of equations may be stated as

$$\sum_{\boldsymbol{G}'} M_{\boldsymbol{G}\boldsymbol{G}'} u_{\boldsymbol{G}'} = \phi_{\boldsymbol{G}}, \tag{3.71}$$

where $\boldsymbol{G}_\parallel$ and z have been lumped together into $\boldsymbol{G}$, i.e.

$$\boldsymbol{G} = (\boldsymbol{G}_\parallel, z). \tag{3.72}$$

The matrix M is given by

$$M_{\boldsymbol{G}\boldsymbol{G}'} = \delta_{\boldsymbol{G},\boldsymbol{G}'} + \frac{1}{2\pi} w' f_{\tilde{G}_\parallel}(|z - z'|) V_{\boldsymbol{G}_\parallel - \boldsymbol{G}'_\parallel}(z'), \tag{3.73}$$

while the inhomogeinity is

$$\phi_{\boldsymbol{G}} = \delta_{\Delta\boldsymbol{G}_\parallel,\boldsymbol{G}_\parallel} e^{ik_z z}. \tag{3.74}$$

3.4.1 Asymptotic behavior of the Green function

As a first step in solving the LS equation, the function $f_{G_\parallel}(z, z')$ in Eq. (3.65) must be evaluated. This can only be done numerically. Since there are no singularities in the integrand, the asymptotic behavior determines the convergence of the integral. For large values of ρ, the integrand in $f_{G_\parallel}(z, z')$ behaves like

$$e^{ik\rho} J_0(G_\parallel \rho). \tag{3.75}$$

Hence, the integral yields

$$\int_0^\infty d\rho e^{ik\rho} J_0(G_\parallel \rho) = \frac{i}{k^2 - G_\parallel^2}, \tag{3.76}$$

which diverges for $k = G_\parallel$ and therefore must be modified before attempting to solve the LS equation. One possibility is again to add an imaginary part $i\epsilon$ to k^2, i.e. $k^2 \to k^2 + i\epsilon$. This turns the result into

$$\int_0^\infty d\rho e^{ik\rho} J_0(G_\parallel \rho) = \frac{1}{\epsilon} \quad \text{for } G_\parallel = k, \tag{3.77}$$

which depends sensitively on ϵ. At the moment there seems to be no convincing physical argument for any particular value of ϵ, which again corresponds to the mean free path of the photoelectron. In this approach, ϵ is just a parameter.

3.5 Approach 4: the eigenfunction expansion of the Green function

The eigenfunction expansion of the Green function [39]

$$G(E_k) = \sum_{n\boldsymbol{q}} \frac{|\psi_{n\boldsymbol{q}}\rangle \langle\psi_{n\boldsymbol{q}}|}{E_k - \epsilon_{n\boldsymbol{q}} + i\epsilon} \tag{3.78}$$

might turn out to be very convenient. The Schrödinger equation for the Bloch states is given by

$$(H_{kin} + V)\,|\psi_{n\boldsymbol{q}}\rangle = \epsilon_{n\boldsymbol{q}}\,|\psi_{n\boldsymbol{q}}\rangle\,. \tag{3.79}$$

The Lippmann-Schwinger equation in terms of the complete Green function of the system reads

$$|\psi_{\boldsymbol{k}}\rangle = |\boldsymbol{k}\rangle + GV\,|\boldsymbol{k}\rangle\,. \tag{3.80}$$

The LS equation must be solved for every initial state $|\psi_{n\boldsymbol{q}}\rangle$. Due to momentum conservation $\boldsymbol{k}$ is related to $\boldsymbol{q}$ by

$$\boldsymbol{k} = \boldsymbol{q} + \Delta\boldsymbol{G}. \tag{3.81}$$

Inserting the eigenfunction expansion of the Green function leads to

$$GV\,|\boldsymbol{k}\rangle = \sum_{n\boldsymbol{q}} \frac{|\psi_{n\boldsymbol{q}}\rangle \langle\psi_{n\boldsymbol{q}}|}{E_k - \epsilon_{n\boldsymbol{q}} + i\epsilon} V\,|\boldsymbol{k}\rangle\,. \tag{3.82}$$

The potential in $\langle\psi_{n\boldsymbol{q}}|V|\boldsymbol{k}\rangle$ may also act to the left:

$$\langle\psi_{n\boldsymbol{q}}|V|\boldsymbol{k}\rangle = \langle\psi_{n\boldsymbol{q}}|\epsilon_{n\boldsymbol{q}} - H_{kin}|\boldsymbol{k}\rangle\,. \tag{3.83}$$

The kinetic energy of the state $|\boldsymbol{k}\rangle$ is just E_k. So,

$$\langle\psi_{n\boldsymbol{q}}|\epsilon_{n\boldsymbol{q}} - E_k|\boldsymbol{k}\rangle = (\epsilon_{n\boldsymbol{q}} - E_k)\,\langle\psi_{n\boldsymbol{q}}|\boldsymbol{k}\rangle\,. \tag{3.84}$$

$\langle\psi_{n\boldsymbol{q}}|\boldsymbol{k}\rangle$ on the other hand is just

$$\langle\psi_{n\boldsymbol{q}}|\boldsymbol{k}\rangle = \sum_{\boldsymbol{G}} c^*_{n\boldsymbol{q}}(\boldsymbol{G})\,\langle\boldsymbol{q} + \boldsymbol{G}|\boldsymbol{k}\rangle = c^*_{n\boldsymbol{q}}(\Delta\boldsymbol{G}). \tag{3.85}$$

This means that

$$GV\,|\boldsymbol{k}\rangle = -\sum_{n\boldsymbol{q}} c^*_{n\boldsymbol{q}}(\Delta\boldsymbol{G}) \frac{E_k - \epsilon_{n\boldsymbol{q}}}{E_k - \epsilon_{n\boldsymbol{q}} + i\epsilon}\,|\psi_{n\boldsymbol{q}}\rangle\,. \tag{3.86}$$

For most terms in the sum, the small imaginary part $i\epsilon$ in the denominator can be disregarded, that is

$$\frac{E_k - \epsilon_{n\boldsymbol{q}}}{E_k - \epsilon_{n\boldsymbol{q}} + i\epsilon} \approx 1. \tag{3.87}$$

For some terms, the above cancellation is invalid and the imaginary part $i\epsilon$ must be included. Introducing the abbreviation

$$\Delta E \equiv E_k - \epsilon_{n_s\boldsymbol{q}_s}, \tag{3.88}$$

which is ≈ 0 for the states $|\psi_{n_s\boldsymbol{q}_s}\rangle$ implies that

$$\frac{\Delta E}{\Delta E + i\epsilon} = \frac{\Delta E^2}{\Delta E^2 + \epsilon^2} - i\frac{\Delta E\epsilon}{\Delta E^2 + \epsilon^2}. \tag{3.89}$$

The first term gives 1 in the limit $\epsilon \to 0$. The second one allows one to introduce some artificial broadening into the system by replacing the delta function representation

$$\delta(x) = \frac{1}{\pi}\frac{\epsilon}{x^2 + \epsilon^2} \tag{3.90}$$

with a broadening curve of Lorentzian shape, i.e.

$$\frac{\Delta E}{\Delta E + i\epsilon} \approx 1 - i\pi\Delta E\delta_{\Delta E}. \tag{3.91}$$

In the simulation the broadened delta function might be replaced by a different type to accelerate the convergence (e.g. of Gaussian type). Returning to the original problem, it is clear that the terms $|\psi_{n_s\boldsymbol{q}_s}\rangle$ must be removed from the sum:

$$GV\,|\boldsymbol{k}\rangle = -{\sum_{n\boldsymbol{q}}}'\,|\psi_{n\boldsymbol{q}}\rangle\,\langle\psi_{n\boldsymbol{q}}|\boldsymbol{k}\rangle - \sum_{n_s\boldsymbol{q}_s}(|\psi_{n_s\boldsymbol{q}_s}\rangle\,\langle\psi_{n_s\boldsymbol{q}_s}|\boldsymbol{k}\rangle + i\pi\Delta E\delta(\Delta E)\,|\psi_{n_s\boldsymbol{q}_s}\rangle\,\langle\psi_{n_s\boldsymbol{q}_s}|\boldsymbol{k}\rangle). \tag{3.92}$$

The second term on the right-hand side can be moved inside the first sum, which then contains all states. That means that

$$\begin{aligned} GV\,|\boldsymbol{k}\rangle &= -\sum_{n\boldsymbol{q}}\,|\psi_{n\boldsymbol{q}}\rangle\,\langle\psi_{n\boldsymbol{q}}|\boldsymbol{k}\rangle + i\pi\Delta E\delta(\Delta E)\,|\psi_{n_s\boldsymbol{q}_s}\rangle\,\langle\psi_{n_s\boldsymbol{q}_s}|\boldsymbol{k}\rangle \\ &= -\,|\boldsymbol{k}\rangle + i\pi\sum_{n_s\boldsymbol{q}_s}\Delta E\delta(\Delta E)\,|\psi_{n_s\boldsymbol{q}_s}\rangle\,\langle\psi_{n_s\boldsymbol{q}_s}|\boldsymbol{k}\rangle\,. \end{aligned} \tag{3.93}$$

The final state is then just

$$|\psi_{\boldsymbol{k}}\rangle = i\pi\sum_{n_s\boldsymbol{q}_s}\Delta E\delta(\Delta E)\,|\psi_{n_s\boldsymbol{q}_s}\rangle\,\langle\psi_{n_s\boldsymbol{q}_s}|\boldsymbol{k}\rangle\,. \tag{3.94}$$

The required matrix element for the initial state $|\psi_{n_{in}\boldsymbol{q}_{in}}\rangle$ is then just

$$\langle\psi_{n_{in}\boldsymbol{q}_{in}}|\boldsymbol{p}|\psi_{\boldsymbol{k}}\rangle = i\pi \sum_s \Delta E_s \delta_{\Delta E_s} \langle\psi_{n_{in}\boldsymbol{q}_{in}}|\boldsymbol{p}|\psi_{n_s\boldsymbol{q}_s}\rangle \langle\psi_{n_s\boldsymbol{q}_s}|\boldsymbol{k}\rangle \,. \tag{3.95}$$

where the optical matrix element between Bloch states $\langle\psi_{n_{in}\boldsymbol{q}_{in}}|\boldsymbol{p}|\psi_{n_s\boldsymbol{q}_s}\rangle$ can be directly calculated by the employed DFT code. Only terms with $\boldsymbol{q}_{in} \approx \boldsymbol{q}_s$ will contribute to this sum.

3.6 Expanding the photoelectron final state into Bloch functions

Essentially, what the eigenfunction expansion of the Green function amounts to is the expansion of the final state into solutions of the crystal potential. A similar approach is taken in the paper [50], where the authors match the ansatz to a LEED state. The same problem can also be addressed via the free particle Green function formalism of the Lippmann-Schwinger equation, which is repeated here

$$|\psi_{\boldsymbol{k}}\rangle = |\boldsymbol{k}\rangle + G_0 V |\psi_{\boldsymbol{k}}\rangle \,. \tag{3.96}$$

The ansatz for the final state is

$$|\psi_{\boldsymbol{k}}\rangle = \sum_n a_n |\psi_{n\boldsymbol{q}}\rangle \,. \tag{3.97}$$

In principle, the sum should also include an index $\boldsymbol{q}$, but this is unnecessary because the matrix element with the initial state $|\psi_{n_{in}\boldsymbol{q}_{in}}\rangle$ would suppress all other contributions:

$$\langle\psi_{n_{in}\boldsymbol{q}_{in}}|\boldsymbol{p}|\psi_{n\boldsymbol{q}}\rangle = 0, \text{ for } \boldsymbol{q}_{in} \neq \boldsymbol{q}. \tag{3.98}$$

Here, $\boldsymbol{k}$ corresponds to $\boldsymbol{q}$ via $\boldsymbol{k} = \boldsymbol{q} + \Delta\boldsymbol{G}$. $V|\psi_{\boldsymbol{k}}\rangle$ can again be rewritten thanks to the Schrödinger equation

$$\begin{aligned} V|\psi_{\boldsymbol{k}}\rangle &= \sum_n a_n V |\psi_{n\boldsymbol{q}}\rangle = \sum_n a_n (\epsilon_{n\boldsymbol{q}} - H_{kin}) |\psi_{n\boldsymbol{q}}\rangle \\ &= \sum_{n\boldsymbol{G}} a_n c_{n\boldsymbol{q}}(\boldsymbol{G})(\epsilon_{n\boldsymbol{q}} - H_{kin}) |\boldsymbol{q}+\boldsymbol{G}\rangle \\ &= \sum_{n\boldsymbol{G}} a_n c_{n\boldsymbol{q}}(\boldsymbol{G})(\epsilon_{n\boldsymbol{q}} - E_{\boldsymbol{q}+\boldsymbol{G}}) |\boldsymbol{q}+\boldsymbol{G}\rangle \,, \end{aligned} \tag{3.99}$$

where

$$E_{\boldsymbol{q}} = \frac{\hbar^2 q^2}{2m}. \tag{3.100}$$

With this the Lippmann-Schwinger equation reads

$$\sum_n a_n \left|\psi_{n\boldsymbol{q}}\right\rangle = \left|\boldsymbol{k}\right\rangle + G_0 \sum_{n\boldsymbol{G}} a_n c_{n\boldsymbol{q}}(\boldsymbol{G})(\epsilon_{n\boldsymbol{q}} - E_{\boldsymbol{q}+\boldsymbol{G}}) \left|\boldsymbol{q}+\boldsymbol{G}\right\rangle. \tag{3.101}$$

Acting with $\langle \boldsymbol{q}+\boldsymbol{G}_1|$ turns the LS equation into

$$\sum_n a_n \left\langle \boldsymbol{q}+\boldsymbol{G}_1|\psi_{n\boldsymbol{q}}\right\rangle = \sum_{n\boldsymbol{G}} a_n c_{n\boldsymbol{q}}(\boldsymbol{G}) \left\langle \boldsymbol{q}+\boldsymbol{G}_1|\boldsymbol{q}+\boldsymbol{G}\right\rangle = \sum_n a_n c_{n\boldsymbol{q}}(\boldsymbol{G}_1) \tag{3.102}$$

on the left-hand side, while the right-hand side gives

$$\delta_{\boldsymbol{G}_1,\Delta\boldsymbol{G}} + G_0(\boldsymbol{q}+\boldsymbol{G}_1) \sum_n a_n c_{n\boldsymbol{q}}(\boldsymbol{G}_1)(\epsilon_{n\boldsymbol{q}} - E_{\boldsymbol{q}+\boldsymbol{G}_1}). \tag{3.103}$$

Putting both results together and dropping the index on $\boldsymbol{G}_1$:

$$\sum_n a_n c_{n\boldsymbol{q}}(\boldsymbol{G}) = \delta_{\boldsymbol{G},\Delta\boldsymbol{G}} + G_0(\boldsymbol{q}+\boldsymbol{G}) \sum_n a_n c_{n\boldsymbol{q}}(\boldsymbol{G})(\epsilon_{n\boldsymbol{q}} - E_{\boldsymbol{q}+\boldsymbol{G}}). \tag{3.104}$$

Bringing the Green function term to the other side results in

$$\sum_n c_{n\boldsymbol{q}}(\boldsymbol{G})(1 - G_0(\boldsymbol{q}+\boldsymbol{G})(\epsilon_{n\boldsymbol{q}} - E_{\boldsymbol{q}+\boldsymbol{G}}))a_n = \delta_{\boldsymbol{G},\Delta\boldsymbol{G}}. \tag{3.105}$$

Furthermore,

$$G_0(\boldsymbol{q}+\boldsymbol{G}) = \frac{1}{E_{\boldsymbol{k}} - E_{\boldsymbol{q}+\boldsymbol{G}} + i\epsilon}. \tag{3.106}$$

And so,

$$\begin{aligned} 1 - G_0(\boldsymbol{q}+\boldsymbol{G})(\epsilon_{n\boldsymbol{q}} - E_{\boldsymbol{q}+\boldsymbol{G}}) =& \frac{E_{\boldsymbol{k}} - E_{\boldsymbol{q}+\boldsymbol{G}} - (\epsilon_{n\boldsymbol{q}} - E_{\boldsymbol{q}+\boldsymbol{G}})}{E_{\boldsymbol{k}} - E_{\boldsymbol{q}+\boldsymbol{G}} + i\epsilon} \\ =& \frac{E_{\boldsymbol{k}} - \epsilon_{n\boldsymbol{q}}}{E_{\boldsymbol{k}} - E_{\boldsymbol{q}+\boldsymbol{G}} + i\epsilon}. \end{aligned} \tag{3.107}$$

The denominator can now be brought to the right-hand side:

$$\sum_n c_{n\boldsymbol{q}}(\boldsymbol{G})(E_{\boldsymbol{k}} - \epsilon_{n\boldsymbol{q}})a_n = \delta_{\boldsymbol{G},\Delta\boldsymbol{G}}(E_{\boldsymbol{k}} - E_{\boldsymbol{q}+\boldsymbol{G}} + i\epsilon). \tag{3.108}$$

Multiplying by $c^*_{n'\boldsymbol{q}}(\boldsymbol{G})$ and summing over $\boldsymbol{G}$ gives

$$\begin{aligned}\sum_n \sum_{\boldsymbol{G}} c^*_{n'\boldsymbol{q}}(\boldsymbol{G}) c_{n\boldsymbol{q}}(\boldsymbol{G})(E_{\boldsymbol{k}} - \epsilon_{n\boldsymbol{q}})a_n &= \sum_n \delta_{n,n'}(E_{\boldsymbol{k}} - \epsilon_{n\boldsymbol{q}})a_n \\ &= (E_{\boldsymbol{k}} - \epsilon_{n'\boldsymbol{q}})a_{n'}\end{aligned} \tag{3.109}$$

on the left-hand side. The delta function on the right-hand side picks out a single reciprocal lattice contribution:

$$\sum_{\boldsymbol{G}} c^*_{n'\boldsymbol{q}}(\boldsymbol{G})\delta_{\boldsymbol{G},\Delta\boldsymbol{G}}(E_{\boldsymbol{k}} - E_{\boldsymbol{q}+\boldsymbol{G}} + i\epsilon) = c^*_{n'\boldsymbol{q}}(\Delta\boldsymbol{G})(E_{\boldsymbol{k}} - E_{\boldsymbol{q}+\Delta\boldsymbol{G}} + i\epsilon). \tag{3.110}$$

Considering the relation between $\boldsymbol{q}$ and $\boldsymbol{k}$ the right-hand side would vanish in general were it not for the small imaginary part $i\epsilon$. Taking this factor into account the right-hand side is simply

$$c^*_{n'\boldsymbol{q}}(\Delta\boldsymbol{G})(E_{\boldsymbol{k}} - E_{\boldsymbol{q}+\Delta\boldsymbol{G}}) = c^*_{n'\boldsymbol{q}}(\Delta\boldsymbol{G})i\epsilon. \tag{3.111}$$

The coefficient a_n is determined by

$$a_n = c^*_{n\boldsymbol{q}}(\Delta\boldsymbol{G})\frac{i\epsilon}{E_{\boldsymbol{k}} - \epsilon_{n\boldsymbol{q}} + i\epsilon}. \tag{3.112}$$

Only terms with $E_{\boldsymbol{k}} - \epsilon_{n\boldsymbol{q}} \approx 0$ contribute to the expansion. In this case the fraction on the right-hand side yields

$$\frac{i\epsilon}{E_{\boldsymbol{k}} - \epsilon_{n\boldsymbol{q}} + i\epsilon} = \frac{\epsilon^2}{\Delta E^2 + \epsilon^2} + i\Delta E\frac{\epsilon}{\Delta E^2 + \epsilon^2}, \tag{3.113}$$

where $\Delta E = E_{\boldsymbol{k}} - \epsilon_{n\boldsymbol{q}}$. The first term vanishes for small ϵ and the second term again yields a delta function representation. Reinserting this into a_n leads to

$$a_n = i\pi c^*_{n\boldsymbol{q}}(\Delta\boldsymbol{G})\Delta E_n\delta(\Delta E_n). \tag{3.114}$$

In summary the final state in this approach is given by

$$|\psi_{\boldsymbol{k}}\rangle = i\pi\sum_n c^*_{n\boldsymbol{q}}(\Delta\boldsymbol{G})\Delta E_n\delta(\Delta E_n)\,|\psi_{n\boldsymbol{q}}\rangle\,. \tag{3.115}$$

This is identical to Eqn. (3.94).

Both eigenfunction expansion methods make heavy use of the orthonormality of the respective basis sets. This means that the implementation would either have

to employ a norm conserving pseudopotential, or explicitly take the all-electron effects of the PAW formalism into account. In principle this should be relatively straightforward. The optical matrix element in Eqn. (3.95), $\langle\psi_{n_{in}\boldsymbol{q}_{in}}|\boldsymbol{p}|\psi_{n_s\boldsymbol{q}_s}\rangle$, can be computed directly by the DFT code. The only remaining term to be considered is then $\langle\psi_{n_s\boldsymbol{q}_s}|\boldsymbol{k}\rangle$, but this is just

$$\langle\boldsymbol{k}|\psi_{n_s\boldsymbol{q}_s}\rangle = \langle\boldsymbol{k}|\mathcal{T}|\tilde{\psi}_{n_s\boldsymbol{q}_s}\rangle\,, \tag{3.116}$$

where $|\tilde{\psi}_{n_s\boldsymbol{q}_s}\rangle$ is the pseudowavefunction and $|\psi_{n_s\boldsymbol{q}_s}\rangle$ is the all-electron wavefunction. The transformation coefficients can probably be extracted from the DFT code.

3.7 The Lippmann-Schwinger equation for the initial state

The LS equation can also be used to calculate bound state properties [38]. In this case there is no solution for the free particle Hamiltonian and the LS equation takes the following form:

$$|\psi\rangle = G_0 V\,|\psi\rangle\,. \tag{3.117}$$

k must be replaced by $-i\alpha$ in the Green function and the energy of the state is given by $-\frac{\hbar^2\alpha^2}{2m}$. $|\psi\rangle$ is can be expressed as a Bloch wave in k-space:

$$|\psi_{\boldsymbol{q}}\rangle = \sum_{\boldsymbol{G}} u_{\boldsymbol{q}}\,|\boldsymbol{q}+\boldsymbol{G}\rangle\,. \tag{3.118}$$

The coefficients may be determined by projection:

$$\langle\boldsymbol{q}+\boldsymbol{G}|\psi_{\boldsymbol{q}}\rangle = u_{\boldsymbol{q}}(\boldsymbol{G}). \tag{3.119}$$

According to the LS equation this quantity is equal to

$$\langle\boldsymbol{q}+\boldsymbol{G}|G_0V|\psi_{\boldsymbol{q}}\rangle = -\frac{c}{4\pi}\int d^3r d^3r' e^{-i(\boldsymbol{q}+\boldsymbol{G})\boldsymbol{r}}\frac{e^{-\alpha|\boldsymbol{r}-\boldsymbol{r}'|}}{|\boldsymbol{r}-\boldsymbol{r}'|}V(\boldsymbol{r}')\psi_{\boldsymbol{q}}(\boldsymbol{r}'). \tag{3.120}$$

The integral over $\boldsymbol{r}$ can be calculated analytically

$$\int d^3r e^{-i(\boldsymbol{q}+\boldsymbol{G})\boldsymbol{r}}\frac{e^{-\alpha|\boldsymbol{r}-\boldsymbol{r}'|}}{|\boldsymbol{r}-\boldsymbol{r}'|} = e^{-i(\boldsymbol{q}+\boldsymbol{G})\boldsymbol{r}'}\int d^3\rho e^{-i(\boldsymbol{q}+\boldsymbol{G})\boldsymbol{\rho}}\frac{e^{-\alpha\rho}}{\rho}. \tag{3.121}$$

The integral can be evaluated in spherical coordinates

$$\int d^3\rho e^{-i(\boldsymbol{q}+\boldsymbol{G})\boldsymbol{\rho}}\frac{e^{-\alpha\rho}}{\rho} = 2\pi\int d\rho d\cos(\theta)e^{-iG\rho\cos(\theta)}e^{-\alpha\rho}\rho, \tag{3.122}$$

where $\boldsymbol{q}$ has been absorbed into $\boldsymbol{G}$ for the sake of brevity. The integration over θ yields

$$\int d\rho d\cos(\theta) e^{-iG\rho\cos(\theta)} e^{-\alpha\rho}\rho = \frac{1}{-iG}\int d\rho (e^{-iG\rho} - e^{iG\rho}) e^{-\alpha\rho}. \tag{3.123}$$

Moving on to the ρ integral

$$\int d\rho (e^{-(iG+\alpha)\rho} - e^{(iG-\alpha)\rho}) = -\left(\frac{1}{-iG-\alpha} - \frac{1}{iG-\alpha}\right) = -\frac{2iG}{G^2+\alpha^2}. \tag{3.124}$$

Collecting factors gives

$$\int d^3r e^{-i(\boldsymbol{q}+\boldsymbol{G})\boldsymbol{r}} \frac{e^{-\alpha|\boldsymbol{r}-\boldsymbol{r}'|}}{|\boldsymbol{r}-\boldsymbol{r}'|} = 4\pi \frac{e^{-i(\boldsymbol{q}+\boldsymbol{G})\boldsymbol{r}'}}{|\boldsymbol{G}+\boldsymbol{q}|^2+\alpha^2}. \tag{3.125}$$

Inserting this and the plane wave expansions of the state and the potential into the right-hand side of Eqn. (3.120) leads to

$$\begin{aligned}
\langle \boldsymbol{q}+\boldsymbol{G}|G_0 V|\psi_{\boldsymbol{q}}\rangle &= -\frac{c}{|\boldsymbol{G}+\boldsymbol{q}|^2+\alpha^2}\sum_{\boldsymbol{G}_1\boldsymbol{G}_2}\int d^3r' e^{-i(\boldsymbol{q}+\boldsymbol{G})\boldsymbol{r}'} u_{\boldsymbol{q}}(\boldsymbol{G}_1) e^{i(\boldsymbol{q}+\boldsymbol{G}_1)\boldsymbol{r}'} V_{\boldsymbol{G}_2} e^{i\boldsymbol{G}_2\boldsymbol{r}'} \\
&= -\frac{c}{|\boldsymbol{G}+\boldsymbol{q}|^2+\alpha^2}\sum_{\boldsymbol{G}_1\boldsymbol{G}_2}\delta_{\boldsymbol{G}_1+\boldsymbol{G}_2,\boldsymbol{G}} u_{\boldsymbol{q}}(\boldsymbol{G}_1) V_{\boldsymbol{G}_2} \\
&= -\frac{c}{|\boldsymbol{G}+\boldsymbol{q}|^2+\alpha^2}\sum_{\boldsymbol{G}_1} u_{\boldsymbol{q}}(\boldsymbol{G}_1) V_{\boldsymbol{G}-\boldsymbol{G}_1}.
\end{aligned} \tag{3.126}$$

So the LS equation is

$$u_{\boldsymbol{q}}(\boldsymbol{G}) = -\frac{c}{|\boldsymbol{G}+\boldsymbol{q}|^2+\alpha^2}\sum_{\boldsymbol{G}_1} V_{\boldsymbol{G}-\boldsymbol{G}_1} u_{\boldsymbol{q}}(\boldsymbol{G}_1). \tag{3.127}$$

Introducing the abbreviation

$$M_{\boldsymbol{G}\boldsymbol{G}_1} = -\frac{c}{|\boldsymbol{G}+\boldsymbol{q}|^2+\alpha^2} V_{\boldsymbol{G}-\boldsymbol{G}_1} \tag{3.128}$$

gives the compact expression

$$\sum_{\boldsymbol{G}_1} M_{\boldsymbol{G}\boldsymbol{G}_1} u_{\boldsymbol{q}}(\boldsymbol{G}_1) = u_{\boldsymbol{q}}(\boldsymbol{G}). \tag{3.129}$$

This is a special sort of eigenvalue problem $Mu = \lambda u$. For there to be a bound state the eigenvalue λ must be equal to 1, which gives the condition that the state has to satisfy.

Chapter 4

A simple toy model: particle in a spherical box

To illustrate the basic approach to the calculation of the photoelectron final state, the model of a particle in a spherical box will be used. The model is simpler to implement than the DFT examples of Chapters 5 and 6 while already displaying a surprisingly interesting photoemission behavior. In this case, the potential takes the simple form

$$V(\boldsymbol{r}) = \begin{cases} V_0 \text{ for } r < a \\ 0 \text{ for } r > a \end{cases} \tag{4.1}$$

with no nonlocal contribution. Although the problem cannot be solved analytically, the spherical symmetry allows accurate approximations to be obtained rather easily (see for example Ref. [51]).[1] The bound states $\psi_{nlm}(\boldsymbol{r})$ in a radial potential can be written in the form

$$\psi_{nlm}(\boldsymbol{r}) = R_{nl}(r)Y_{lm}(\Omega), \tag{4.2}$$

where n is the main quantum number, and l and m denote the orbital angular momentum and its projection. Here, $R_{nl}(r)$ is the solution of the radial equation, which must be finite for $r \to 0$ and must vanish for $r \to \infty$.

In order to assess the discretization errors, the Green function solution is compared to the full numerical solution of the Schröedinger equation as well. With the definition

$$\chi_{nl}(r) = \frac{R_{nl}(r)}{r}, \tag{4.3}$$

[1] We will nevertheless refer to this solution as "analytical" in order to distinguish it from the numerical solution of the discretized Schrödinger equation. This "analytical" wavefunction is obtained from the solution of an implicit equation [51].

the Schrödinger equation takes the form

$$\left[\frac{1}{2}\left(-\partial_r^2 + \frac{l(l+1)}{r^2}\right) + V(r)\right]\chi_{nl}(r) = E_{nl}\chi_{nl}(r). \tag{4.4}$$

In order for $R_{nl}(r)$ to be finite at the origin, χ_{nl} must vanish there, i.e.

$$\chi_{nl}(0) = 0. \tag{4.5}$$

This chapter deals solely with photoemission from the ground state s-orbital, so $n = 1$ and $l = 0$. To simplify the notation, we omit the indices on χ, i.e.

$$\left(-\frac{1}{2}\partial_r^2 + V(r)\right)\chi(r) = E\chi(r), \tag{4.6}$$

where the centrifugal potential term drops out since $l = 0$.

The discretization of the second derivative at the point j in the interior is accomplished by employing a three-point final difference form

$$\partial_r^2\chi_j \approx \frac{\chi_{j+1} - 2\chi_j + \chi_{j-1}}{\Delta r^2}, \tag{4.7}$$

where $\chi_j = \chi(r_j)$ is an abbreviation and Δr is the grid spacing. A grid with linear spacing will be used for the simulations.

4.1 The Lippmann-Schwinger equation for a spherically symmetric potential

To reduce the numerical load, and also for purpose of comparison with the full 3d scheme of Chapter 6, the LS equation may be reduced to the evaluation of just the radial part of the final state wavefunction. As we have seen in Chapter 2.3.2, this is achieved via the identity [38]

$$\begin{aligned}\frac{G(\boldsymbol{r}_1, \boldsymbol{r}_2)}{2} = -\frac{e^{ik|\boldsymbol{r}_1 - \boldsymbol{r}_2|}}{4\pi|\boldsymbol{r}_1 - \boldsymbol{r}_2|} &= \sum_{lm} G_k^{(l)}(r_1, r_2)Y_{lm}^*(\hat{\boldsymbol{r}}_1)Y_{lm}(\hat{\boldsymbol{r}}_2) \\ &= \sum_{lm} G_k^{(l)}(r_1, r_2)Y_{lm}(\hat{\boldsymbol{r}}_1)Y_{lm}^*(\hat{\boldsymbol{r}}_2),\end{aligned} \tag{4.8}$$

where

$$G_k^{(l)}(r; r') = -ikj_l(kr_<)h_l(kr_>). \tag{4.9}$$

Similarly, the scattering solution is expanded into spherical harmonics

$$\begin{aligned}\psi_{\boldsymbol{k}}(\boldsymbol{r}) =& \sum_l \sqrt{\frac{2l+1}{2\pi^2}} i^l R_l(k;r) Y_{l0}(\theta) \\ =& \sqrt{\frac{2}{\pi}} \sum_{lm} i^l R_l(k;r) Y_{lm}(\Omega_{\boldsymbol{k}}) Y^*_{lm}(\Omega_{\boldsymbol{r}}),\end{aligned} \tag{4.10}$$

where θ is the angle between $\boldsymbol{r}$ and $\boldsymbol{k}$. The first form of the final state wavefunction in Eq. (4.10) is appropriate for studying the emission intensity at fixed direction of $\boldsymbol{k}$, while the second is appropriate for the calculation of "momentum maps" (the term will be properly defined later in Chapter 4.3), where the direction, but not the magnitude, of $\boldsymbol{k}$ varies. Assuming a local potential $V(r)$ and introducing the abbreviation

$$U(r) = 2V(r) \tag{4.11}$$

leads to the following integral equation for the scattering states

$$R_l(k;r) = j_l(kr) + \int_0^\infty dr' r'^2 G_k^{(l)}(r;r') U(r') R_l(k;r'), \tag{4.12}$$

which has already been mentioned in Chapter 2.3.2.

Discretization then turns the radial LS equation into

$$R_l(k;r_i) = j_l(kr_i) + \sum_j r_j^2 G_k^{(l)}(r_i;r_j) U(r_j) R_l(k;r_j) w_j, \tag{4.13}$$

where the grid spacing is absorbed into the weight factors w_j. Due to Eq. (4.9) the kernel contains no singularities and may be used directly for the numerical evaluation, except for the term $G_k^{(l)}(r_i;r_j)$, when both arguments are zero. But since this expression gets multiplied by r_j^2 and

$$G_k^{(l)}(r;r) \to \frac{r^l}{r^{l+1}}, \tag{4.14}$$

this term may be safely set to 0 in the calculation.

The solution of Eq. (4.13) may be simplified further by applying the radial Born approximation, which leads to

$$R_l(k;r_i) \approx j_l(kr_i) + \sum_j r_j^2 G_k^{(l)}(r_i;r_j) U(r_j) j_l(kr_j) w_j. \tag{4.15}$$

This process may be further iterated:

$$R_l^{(n+1)}(k;r_i) = j_l(kr_i) + \sum_j r_j^2 G_k^{(l)}(r_i;r_j)U(r_j)R_l^{(n)}(k;r_j)w_j. \tag{4.16}$$

The advantage of the Born approximation (or series) is that the potential only needs to be applied to the known function, instead of being stored in a matrix as in the implicit LS equation. However, as we shall see, the Born approximation is of little value in practical calculations of the photoemission spectrum [17], because the potential cannot be considered to be small in general, leading to a divergent Born series.

4.2 Initial state from Lippmann-Schwinger formalism

Following the general procedure, the initial state can also be obtained from the LS equation by dropping the inhomogeinity [38], i.e., in

$$R_l(k;r) = \int_0^\infty dr' r'^2 G_k^{(l)}(r;r')U(r')R_l(k;r') \tag{4.17}$$

and replacing the real valued k by an imaginary value as follows

$$k \to i\alpha. \tag{4.18}$$

The binding energy is then given by

$$E_{bind} = -\frac{\alpha^2}{2}. \tag{4.19}$$

In operator form the LS equation reads

$$|R_l(k;r)\rangle = G^{(l)} r^2 U \, |R_l(k;r)\rangle = \lambda \, |R_l(k;r)\rangle \, . \tag{4.20}$$

This suggests that the eigenvalue λ of the operator $G^{(l)}r^2U$ must be 1, which gives the condition for the bound state. In general, only one l will yield unity at a given energy, which determines the angular momentum of the corresponding bound state. The numerical solution, even on an extremely fine grid, seems to deviate slightly from the analytical solution at the origin (either too large or too small with a kink). However, the behavior of the wavefunction at the origin in Fig. 4.1 seems to be

improved by treating the integral of the Green function around the origin (for both arguments) more carefully. The variation of the Hankel function in that region is probably too fast to ignore it completely. From the limiting expressions of the Bessel and Hankel functions [46]

$$\begin{aligned} j_l(x) &\approx \frac{x^l}{(2l+1)!!} \\ h_l(x) &\approx -i\frac{(2l-1)!!}{x^{l+1}} \end{aligned} \tag{4.21}$$

it is apparent that only the s-wave term ($l = 0$) needs to be modified. Since $r = 0$ and $r' > r$ in the integration range, this means

$$G^{(0)}(0, r')r'^2 \approx -ik1\frac{-i}{kr'}r'^2 = -r'. \tag{4.22}$$

The potential and the wavefunction are assumed to vary only slowly compared to the Hankel function so that they can be pulled out of the integral, i.e.

$$\int_0^{\Delta r} dr' r'^2 G_k^{(l)}(r; r')U(r')R_l(k; r') \approx cU(0)R_l(k; 0)\int_0^{\Delta r} dr'(-r') = -cU(0)R_l(k; 0)\frac{\Delta r^2}{2}. \tag{4.23}$$

The results are shown in Fig. 4.1. Note that the numerical solutions of the integral equations differs very little from the analytical solution.

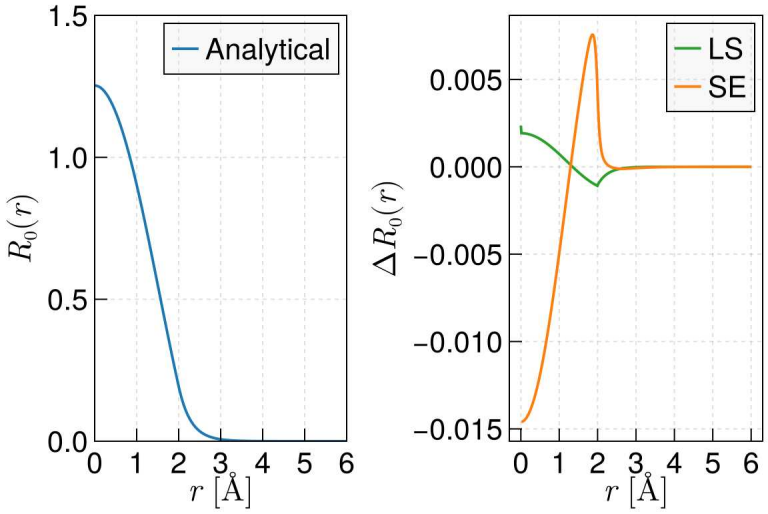

Figure 4.1: Initial state s-wave ground state wavefunction. The analytical solution ('Analytical') is shown in the left panel, while the differences of the numerical solutions to the analytical one are shown in the right panel.

4.3 Momentum maps and line scans

Photoemission intensity maps for a fixed initial state and photoelectron kinetic energy as a function of parallel momentum components k_x and k_y—so-called momentum maps—provide a visual way of displaying the photoemission intensity. Fig. 4.2a shows the normalized photoemission intensity from the ground state orbital into the LS final state calculated in the length gauge.

Momentum maps of this system are rather insensitive to the final state approximation employed, as will become clear soon (some important qualitative differences may appear in more complicated systems, though, see later) A line scan along a particular direction is another way to showcase the data. Fig. 4.2b shows such a line scan in the radial direction (i.e. $k_x = \alpha k_y$ with $E_{kin} = const.$) for the same parameters as in Fig. 4.2a.

The (normalized) matrix elements of a specific momentum map can also be calculated analytically. The calculation is easiest to carry out in the velocity gauge, as opposed to the length gauge that we used so far in this chapter. The results, however, are the same as we only use a local potential, see Chapter 2.4.3. For the system under investigation the initial state is

$$\psi_{\text{in}}(\boldsymbol{r}) = R_{0,\text{in}}(r)Y_{00}(\Omega). \tag{4.24}$$

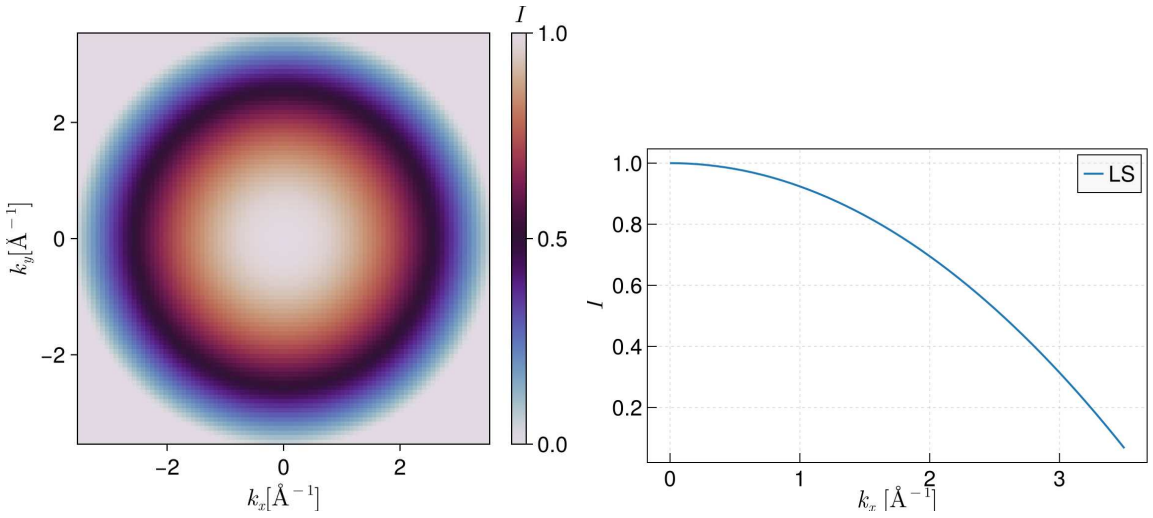

(a) Momentum map (b) Radial scan

Figure 4.2: Photoemission intensity of the ground state of a spherical box with depth $V_0 = -40$ eV and radial extension $a = 2$ Å into the LS final state. The polarization is in the z-direction. The photon energy is set to 83 eV. The calculation is in the length gauge.

Since the gradient acts on the spherically symmetric initial state, the z derivative in spherical coordinates simplifies to

$$\frac{\partial}{\partial z} = \cos(\theta)\frac{\partial}{\partial r}. \tag{4.25}$$

Since

$$\cos(\theta) \propto Y_{10}(\Omega), \tag{4.26}$$

the orthonormality of the spherical harmonics reduces the sum in the matrix element M to just one term:

$$\begin{aligned} M &\propto \langle \psi_{\boldsymbol{k}} | \partial_z | \psi_{\text{in}} \rangle \\ &\propto \sum_{lm} \int dr r^2 i^l R_l^*(k;r) \partial_r R_{0,\text{in}}(r) Y_{lm}(\Omega_{\boldsymbol{k}}) \int d\Omega Y_{lm}^*(\Omega) Y_{10}(\Omega) \\ &= i Y_{10}(\Omega_{\boldsymbol{k}}) \int dr r^2 R_1^*(k;r) \partial_r R_{0,\text{in}}(r). \end{aligned} \tag{4.27}$$

Every point on a momentum map has the same magnitude of the wave vector k, and therefore the radial integral drops out in the course of normalization of the

intensity. Thus, every final state, regardless of the approximation employed, gives rise to the same angular distribution in a momentum map. It should be noted that the radial state only drops out since we are considering photoemission from the s-wave ground state. Initial states with $l \neq 0$ display interference between final states with contributions from both $l+1$ and $l-1$ [45].

Summing up, the intensity of a specific point $\boldsymbol{k}$ on a normalized momentum map is determined solely by the polar direction of that wavevector, and regardless of the final state approximation, via

$$I(\boldsymbol{k}) \propto |Y_{10}(\Omega_{\boldsymbol{k}})|^2 \propto \cos^2(\theta_{\boldsymbol{k}}), \tag{4.28}$$

which is the same as Fig. 4.2.

4.4 Photon-energy dependence of the intensity

In contrast to momentum maps, the kinetic energy of the photoelectron changes in a constant-initial state (CIS)-scan over photon energies. While the emission features at a fixed photon energy show no dependence on the final state approximation (at least for emission from the s-wave ground state), the intensity as a function of the kinetic energy depends sensitively on it. This is illustrated in Fig. 4.3.

Note that the maxima of all functions have been separately normalized. The Born approximation differs only insignificantly from the plane-wave approximation (we will see later on that the Born series does, in fact, not converge). The difference between the plane-wave approximation and the Lippmann-Schwinger solution, on the other hand, is striking. The appearance of new maxima and minima is particularly noteworthy. Also, the two subplots of Fig. 4.3 demonstrates the strong influence of the potential depth on the intensity. Similarly, different values of the range of the potential, r_0, lead to qualitatively different results.

A bit of insight into this can be gleaned from the different gauges. The acceleration gauge, introduced in Chapter 2.4.3, is particularly useful for this simple potential. In order to not drown in a sea of details, the calculation is outlined for the specific case shown in the previous figures—even though it could be carried out much more generally. The ground state is described by

$$\psi_{\text{in}}(\boldsymbol{r}) = R_{0,\text{in}}(r)Y_{00}(\Omega) \tag{4.29}$$

where "in" stands for initial. ∇V simplifies to

$$\nabla V = \partial_r V(r)\boldsymbol{e}_r = -V_0\delta(r-a)\boldsymbol{e}_r. \tag{4.30}$$

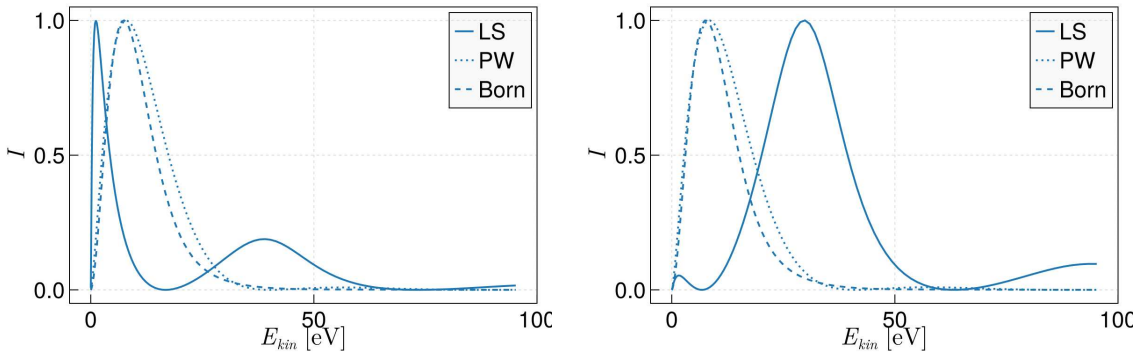

(a) $V_0 = -40$ eV (b) $V_0 = -50$ eV

Figure 4.3: Intensity of the ground state photoemission of a spherical box with depth V_0 and radial extension $r_0 = 2$ Å as a function of the kinetic energy of the photoelectron. The polarization in z-direction. The calculations are performed in the length gauge.

The linear z-polarization picks out the z-component of the gradient, i.e.,

$$\boldsymbol{A}\nabla V \propto -V_0\delta(r-a)\cos(\theta). \tag{4.31}$$

Thus, the matrix element in this case is

$$\langle\psi_{\boldsymbol{k}}|\boldsymbol{A}\nabla V|\psi_{in}\rangle = -V_0\sum_l \int dr\, d\Omega\, r^2 R_l^*(k;r)\delta(r-r_0)R_{0,in}(r)Y_{l0}^*\cos(\theta)Y_{00}(\Omega). \tag{4.32}$$

Since $\cos(\theta) \propto Y_{10}$, only the $l = 1$ contribution will survive , which is expected from the dipole selection rule,

$$\begin{aligned}\langle\psi_{\boldsymbol{k}}|\boldsymbol{A}\nabla V|\psi_{in}\rangle &\propto -V_0\int dr r^2 R_1^*(k;r)\delta(r-r_0)R_{0,in}(r)\\ &= -V_0 r_0^2 R_1^*(k;r_0)R_{0,in}(r_0).\end{aligned} \tag{4.33}$$

The points of vanishing intensity are determined by the final state radial wavefunction. In the case of a plane wave solution, $R_1(k;r) = j_1(kr)$, which is expected to be accurate at high kinetic energies, this means that the intensity will keep oscillating (with diminishing amplitude) as the kinetic energy is increased. The results of the three gauges are shown in Fig. 4.4. That the three gauges agree essentially provides some confirmation on the validity of the approach. Compare the points of vanishing

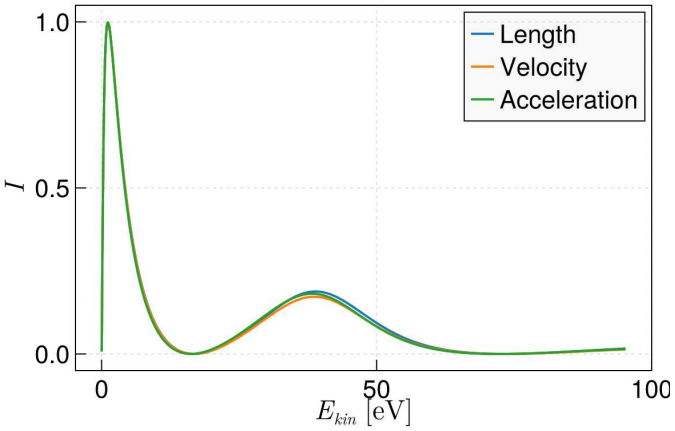

Figure 4.4: Intensity of the ground state photoemission as a function of the kinetic energy of the photoelectron. $V_0 = -40$ eV and $r_0 = 2$ Å. The polarization is in the z-direction.

intensity to the physics of Cooper minima [52], where different angular momentum contributions interfere destructively.

One may wonder whether it is just the first Born approximation that fails to account for the emission pattern and whether higher orders fare better. In general, the Born series is expected to converge for "weak" potentials. This is illustrated in Fig. 4.5. The Born approximation improves somewhat upon the plane-wave approximation for $V_0 = -5$ eV. In contrast, the photoemission calculation with a potential depth of $V_0 = -20$ eV is already better captured by the simple plane wave approach.

Let us investigate the convergence of the Born series more closely. In order for the Born series to be valid, the expression

$$C(k) = \frac{2}{k}\int_0^\infty dr e^{ikr} sin(kr) V(r) \tag{4.34}$$

has to fulfill the condition [38]

$$|C(k)| \ll 1. \tag{4.35}$$

For a spherical box, $|C(k)|$ comes out to be

$$|C(k)| = \frac{V_0}{k^2}\sqrt{\sin^2\frac{kr_0}{2} + r_0 k(r_0 k - \sin r_0 k)}. \tag{4.36}$$

For large enough k, the above expression behaves as $\frac{1}{k}$ and hence converges. For the two scenarios shown in Fig. 4.5, this yields for $E_{\text{kin}} = 10$ eV and hence $k \approx 1.62$ Å^{-1}

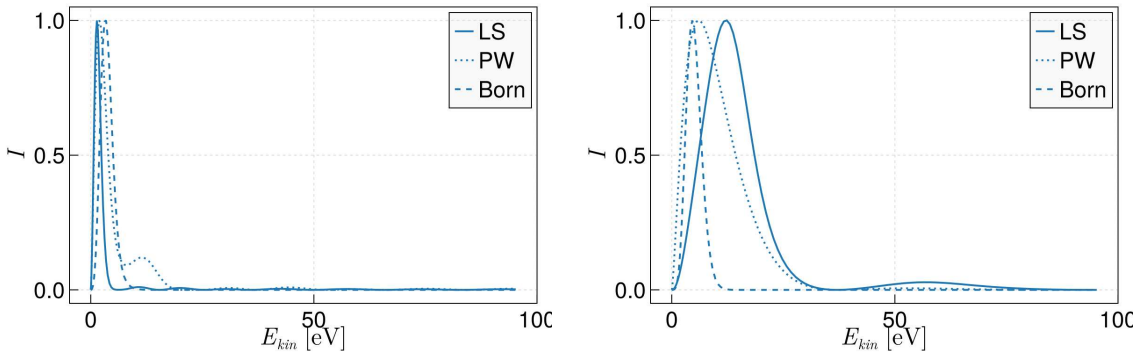

(a) $V_0 = -5$ eV (b) $V_0 = -20$ eV

Figure 4.5: Intensity of the ground state photoemission as a function of the kinetic energy of the photoelectron. $r_0 = 2$ Å in both plots. The polarization is in the z-direction. The tenth-order Born approximation is shown in both panels.

$|C(k)| \approx 0.86$ and 3.44, respectively, consistent with the convergence/nonconvergence shown in Fig. 4.5. Incidentally, this also demonstrates that the convergence at $V_0 = -5$ eV is already rather uncertain.

The Born approximation is thus probably of no relevance in a practical calculation (the same conclusion was reached by [17]). Interestingly, [53] claims the opposite to be true.

4.5 How general are the results?

How will the photoemission change when the rectangular potential is modified slightly? Consider a "smeared" box potential of the form

$$V(r) = c\frac{V_0}{2}\left[1 - \tanh\left(\frac{r-a}{\alpha}\right)\right], \tag{4.37}$$

where α is a length scale that characterizes the smearing of the potential, see Fig. 4.6. Note that c is a constant that properly normalizes the strength of the potential according to

$$\int drr^2 V_1(r) = \int drr^2 V_2(r). \tag{4.38}$$

In particular, if one of the potentials is a spherical box this implies

$$\frac{V_0 r_0^3}{3} = \int drr^2 V(r). \tag{4.39}$$

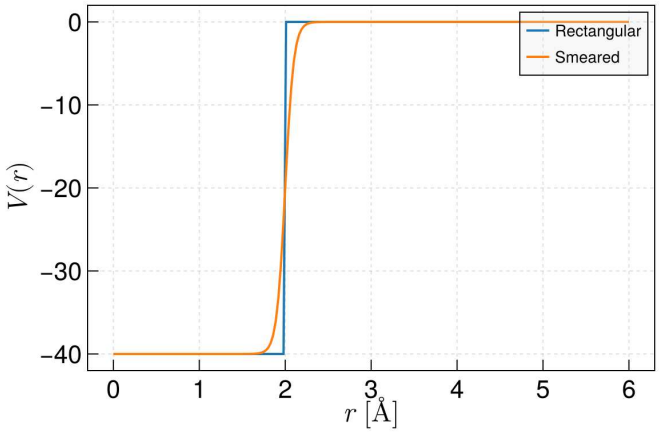

Figure 4.6: Rectangular and smeared box potential with $\alpha = 0.1$ Å.

Fig. 4.7 displays the emission pattern resulting from the potential with a step and the smeared potential with $\alpha = 0.1$ Å. The locations of the extrema roughly stay the same, but they become visibly flatter.

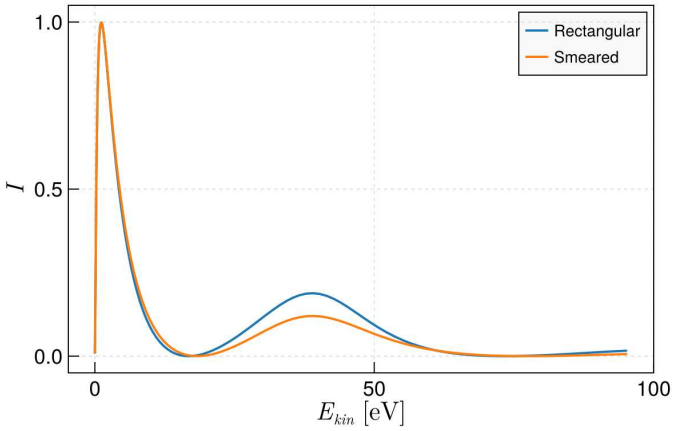

Figure 4.7: Intensity of the ground staate photoemission as a function of the kinetic energy of the photoelectron for two different potentials. The polarization is in the z-direction and the calculation is in the length gauge. The smeared box potential uses $\alpha = 0.1$ Å.

Chapter 5

Atoms as simple test cases

Although the photoemission of atoms is still an area of active research [54, 55]—and even whole books have been written about it [56]—our purpose in this chapter is more modest. The purpose of this chapter is not to obtain some new results, but to test the LS-scheme in a simplified setting, and, as it turns out, to already demonstrate some limitations of the employed method.

Although it is possible to treat atoms by considering the all-electron potential, we resort to pseudopotentials [27]. Specifically, we work with norm-conserving pseudopotentials in the Kleinman-Bylander form [36] introduced in Chapter 2.2. We begin with a short description of how the effect of this nonlocal potential needs to be taken into account.

5.1 Including the nonlocal potential

In comparison to the Chapter 4, the only new feature from a calculational point of view is that we have to include a nonlocal potential in addition to the local potential. The nonlocal potential is in the Kleinman-Bylander form, see Chapter 2.2. The nonlocal potential should be directly extracted from the initial-state DFT calculation. Since there are quite a few different conventions for how to store this quantity—mainly related to units and multiplication by various powers of the radial coordinate—we include some elementary tests to make sure we chose the right convention.

First, by virtue of Eq. (2.29), we can appy the Green function (GF) formalism also to reproduce the radial part of the initial state calculation. For this, the inhomogenous term, $j_l(r)$, has to be dropped [38]. The binding energies obtained in this manner are compared with the corresponding DFT calculations for four rep-

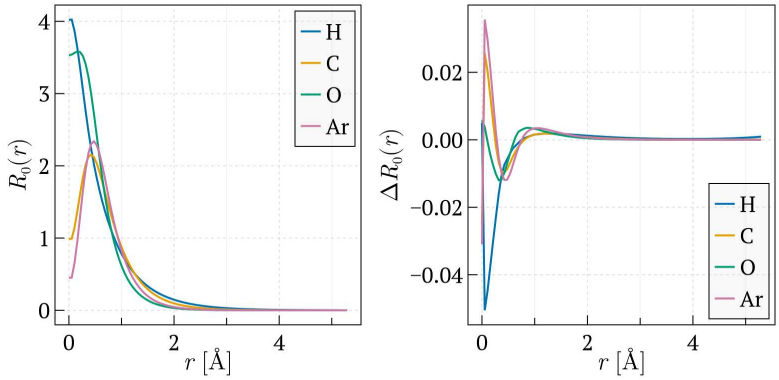

Figure 5.1: Left panel: atomic orbital pseudowavefunctions as calculated by the Green function formalism. Right panel: differences with the corresponding DFT solutions.

resentative atoms in Table 5.1. The energies calculated by the two methods are approximately, but not exactly, equal. The remaining difference is most likely due to a more sophisticated treatment of the nonlocal potential in the employed DFT code [57]. For our purposes, however, the agreement is good enough.

Table 5.1: Binding energies of atomic orbitals in eV calculated via DFT or Green function formalism (GF).

	E_{DFT}	E_{GF}
H 1s	6.47	6.52
C 2s	13.51	13.58
O 2s	24.64	24.79
Ar 3s	24.07	24.25

The pseudowavefunctions of the atomic orbitals in Table 5.1 calculated by the Green function formalism are shown in the left panel of Fig. 5.1, while the right panel shows the difference with the corresponding DFT simulations. The deviations are reasonably small and mainly confined to the origin, which again indicates a more sophisticated treatment of the nonlocal potential in the DFT code.

For a second test, we turn to the final state calculation. Eq. (2.29) must be modified slightly to incorporate the appropr iate boundary conditions for the photo-

electron [40]

$$\begin{aligned} R_l(k;r) =& j_l(kr) + \int_0^\infty dr_1 r_1^2 G_k^{*(l)}(r;r_1) U_{\text{local}}(r_1) R_l(k;r_1) \\ &+ \int_0^\infty dr_1 dr_2 r_1^2 {r_2}^2 G_k^{*(l)}(r;r_1) U_l(r_1,r_2) R_l(k;r_2), \end{aligned} \tag{5.1}$$

where the complex conjugate of the Green function appears. Since we are dealing with a Hermitean Hamilton operator, pseudowavefunctions belonging to different energies must necessarily be orthogonal. This provides an easy test for the LS-method: the resulting overlap with some initial state, which we directly take from a DFT simulation and which therefore automatically contains the nonlocal potential, should be significantly smaller than the overlap of the same initial state with the PW-final state. This is demonstrated in Fig. 5.2, where we plot the ratios

$$\frac{\langle \psi_{\text{ls}} | \psi_{\text{in}} \rangle}{\langle \psi_{\text{pw}} | \psi_{\text{in}} \rangle}. \tag{5.2}$$

Here, $|\psi_{\text{ls}}\rangle$ denotes the final state as calculated by the LS-equation, $|\psi_{\text{pw}}\rangle$ is the plane-wave solution and $|\psi_{\text{in}}\rangle$ is the initial state. As is clear from the figure, the value of the overlap decreases by at least a factor of roughly 10 upon including the nonlocal potential. Furthermore, from the right panel it is also clear that neglecting the nonlocal potential will most likely result in unreliable simulations for carbon and argon, while oxygen and especially hydrogen might stand a better chance.

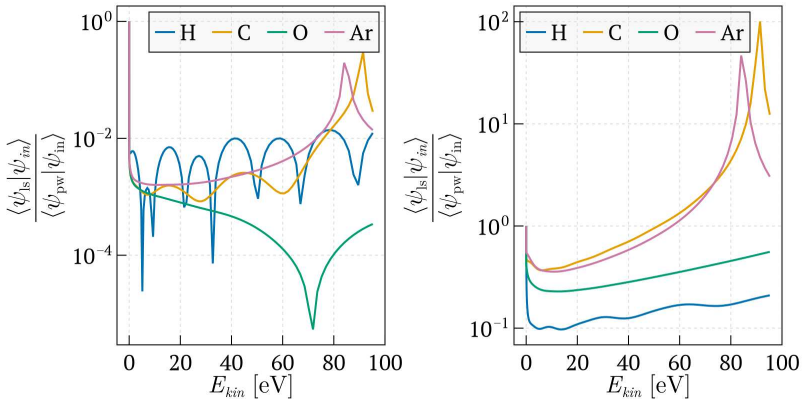

Figure 5.2: Overlap ratios with (left panel) and without (right panel) nonlocal contributions. The overlap in the numerator is calculated via the LS-equation; the denominator uses the plane wave final state. Note the different scales.

5.2 Hydrogen

The hydrogen atom provides the most direct test of the validity of the different final states. Both the initial and final state can be calculated analytically for the Coulomb potential. The pseudopotential with its nonlocal contributions constitutes the main approximation of the numerical method. Hydrogen, with its one electron, in particular suffers from the self-interaction error [27]. Nevertheless, it is the only atomic system that is tractable analytically, and therefore provides a valuable test.

As we have seen in the previous chapter, the momentum map of a s-wave state is independent of the final state. The corresponding momentum map of the 1s state is shown in Fig. 5.3a. A heatmap showing the difference between the simulation result and the analytical solution is displayed in Fig. 5.3b. The resulting difference is essentially just noise (note the scaling factor of the intensity). This is actually to be expected from Eq. (4.28), but nevertheless provides a consistency check.

In the simple case of hydrogen, it is possible to derive an analytical formula for the energy-dependent photoemission intensity [38]. The derivation of the formula uses the analytical form of the initial state [45]

$$\psi_{\mathrm{in}}(\boldsymbol{r}) \propto e^{-r/a_0}, \tag{5.3}$$

where a_0 is the Bohr radius. The final state is given by [38]

$$\psi_{\mathrm{f}}(\boldsymbol{r}) = \sum_{l=0}^{\infty} \sqrt{\frac{2l+1}{2\pi^2}} i^l C_l(k;r) Y_{l0}(\theta). \tag{5.4}$$

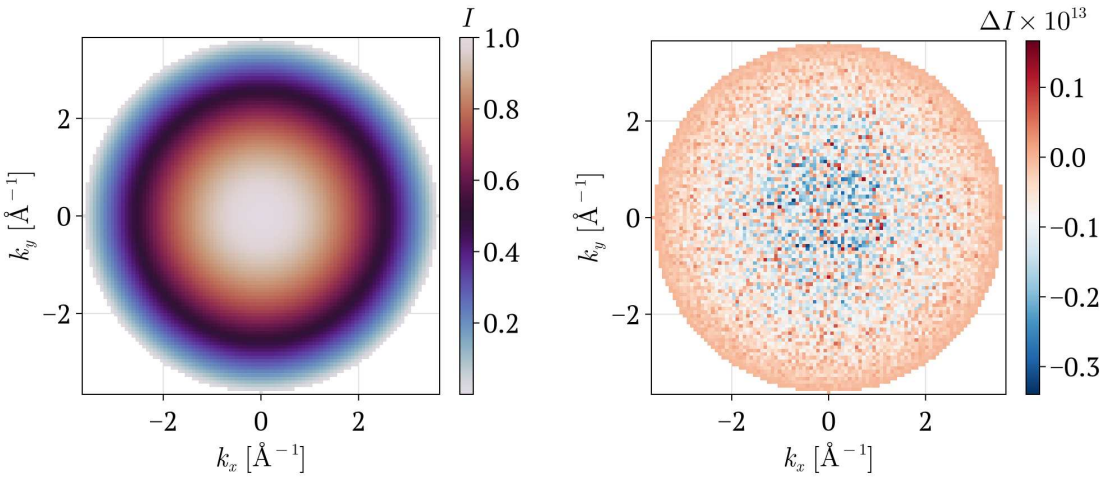

Figure 5.3: Intensity of the 1s photoemission of hydrogen. The polarization is in z-direction. The kinetic energy is 50 eV. The left panel shows the momentum map and the right pannel shows the difference with the analytical solution.

Here, the momentum of the photoelectron is assumed to be along the z-direction. The radial wave function can be expressed as [38]

$$C_l(k;r) \propto \frac{(kr)^l e^{ikr} e^{\pi\gamma/2}}{(2l+1)!}\Gamma(l+1-i\gamma)\,{}_1F_1(l+1-i\gamma;2l+2;-2ikr), \tag{5.5}$$

with the gamma function Γ and the confluent hypergeometric function ${}_1F_1$. γ is given by

$$\gamma = \frac{e^2}{4\pi v}, \tag{5.6}$$

which may be rewritten in a more compact fashion as

$$\gamma = \alpha\frac{c}{v}, \tag{5.7}$$

with α being the fine structure constant, i.e., $\alpha \approx 1/137$.

These two expressions are then plugged into the matrix element[1]

$$\langle\psi_\mathrm{f}|\boldsymbol{A}\boldsymbol{r}|\psi_\mathrm{in}\rangle \tag{5.8}$$

[1]These are exact eigenstates of the Hamilton operator, so it is permissible to use the length gauge.

to obtain

$$I \propto \frac{1}{k^4} \frac{e^{-4\gamma \mathrm{arccot}(\gamma)}}{1 - e^{-2\pi\gamma}}, \tag{5.9}$$

where k is the photon wavevector, i.e.,

$$\omega = ck = E_{\mathrm{ph}} = E_{\mathrm{kin}} + E_{\mathrm{bind}}, \tag{5.10}$$

with the binding energy $E_{\mathrm{bind}} = 13.6$ eV for the 1s orbital. Due to the dipole selection rule [38] only the $l = 1$ component contributes to the matrix element.

The dependence on the kinetic energy is therefore contained in the photon (not photoelectron) wavevector k and the velocity via

$$E_{\mathrm{kin}} = \frac{mv^2}{2}. \tag{5.11}$$

Fig. 5.4 shows the comparison between the analytical solution and the Lippmann-Schwinger and plane-wave approximations of the final state. The Lippmann-Schwinger curve is much narrower than the plane-wave solution. Also, the maximum is shifted to smaller kinetic energies. The Lippmann-Schwinger approximation still falls short of accounting for the maximum at threshold in the analytical expression. This, however, is a peculiarity of the Coulomb potential [38] and cannot be easily reproduced in a simulation, as can be seen from the expression for the photoemission intensity:

$$I(k) \propto k |\, \langle \psi_k | p | \psi_{\mathrm{in}} \rangle \,|^2. \tag{5.12}$$

The matrix element $\langle \psi_k | p | \psi_{\mathrm{in}} \rangle$ has to diverge for vanishingly small values of k, or, equivalently, for infinitely large values of the photoelectron wavelength $\lambda = \frac{2\pi}{k}$, to yield a finite result for the intensity. A finite simulation volume cannot provide this divergence.

As we have seen in the previous chapter, the photoemission intensity may depend sensitively on the concrete radial form of the potential. For now we limit ourselves to the two most commonly employed functionals, namely the local density approximation (LDA) [29, 30] and the generalized gradient approximation (GGA) [31]. Both of these functionals only partially correct the self-interaction error, which is particularly unphyisical for hydrogen with its one electron. To remove it, would require an exact-exchange functional, but we will not pursue this further in this thesis.

At least in the case of hydrogen, both functionals seem to lead to essentially the same results, as shown in Fig. 5.5.

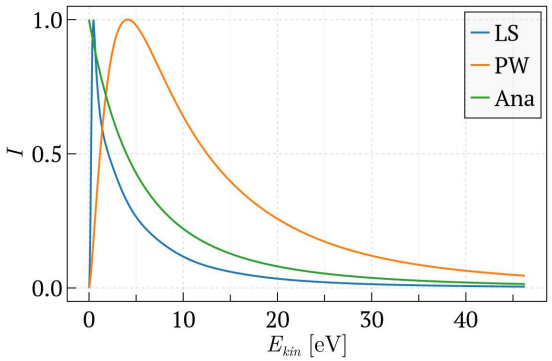

Figure 5.4: Photoemission intensity I as a function of the final state kinetic energy E_{kin} of the 1s orbital in hydrogen. The analytical solution ('Ana') is shown together with the Lippmann-Schwinger solution ('LS') and the plane-wave approximation ('PW').

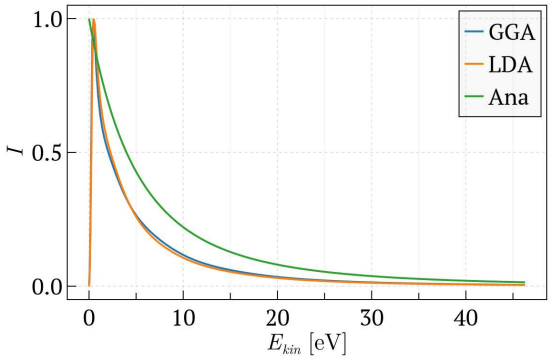

Figure 5.5: Photoemission intensity I as a function of the final state kinetic energy E_{kin} of the 1s orbital in hydrogen. The analytical solution ('Ana') is shown together with the Lippmann-Schwinger solution of the LDA ('LDA') and GGA functional ('GGA').

5.3 Argon

The photoemission intensity of argon's 3s state displays an unexpected behavior [58, 59]. In particular, there is a minimum at a certain photon energy due to "many-body effects", see [60] for more details. That it is challenging to capture this effect in a single particle approximation is corroborated by the fact that the analytical solution of the Hydrogen 3s state shows no sign of this minimum whatsoever, as illustrated in Fig. 5.6[2]. For this plot we used the following form of the 3s state [45]

$$R_{\text{in}}(\boldsymbol{r}) \propto \left(1 - \frac{2}{3a_0}r + \frac{2}{27a_0^2}r^2\right) e^{-r/3a_0}, \tag{5.13}$$

where a_0 is again the Bohr radius. The final state can be taken from Eq. (5.4). Although it is again possible to derive an analytical expression for the photoemission cross section [61, 62], it is easier to do the integral appearing in the matrix element numerically (as was done in the plot).

The DFT results in Fig. 5.7 differ markedly from the prediction of the hydrogen orbitals, but still fall short of reproducing the experimental data satisfactorily [58, 59]. Only the GGA simulation is shown, but LDA gives very similar results.

[2] An effective nuclear charge of one proton was used. It may be worthwile to redo the calculation for an effective charge of 6.75 calculated from Slater's rule.

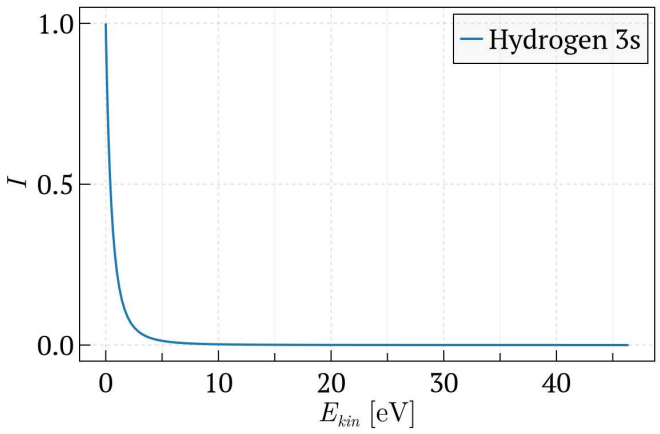

Figure 5.6: Photoemission intensity I as a function of the final state kinetic energy E_{kin} of the 3s orbital in hydrogen.

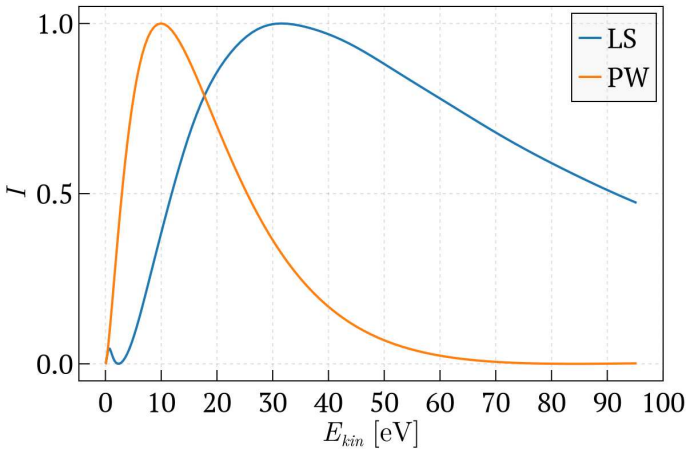

Figure 5.7: Photoemission intensity I as a function of the final state kinetic energy E_{kin} of the 3s orbital in argon. The plane wave prediction is shown together with the Lippmann-Schwinger result.

5.4 Discussion of the results for atoms

The above failure to account for the photon-energy dependence of the 3s orbital of argon might be due to a number of reasons.

All-electron effects. Pseudo wavefunctions smooth the behavior of valence all-electron wavefunctions around the center of the atom. If the photoemission matrix element depends sensitively on the behavior of the wavefunctions around the origin, then pseudo wavefunctions cannot provide a reliable description. With the PAW formalism (see Chapter 2.2), it is possible to reconstruct the all-electron wavefunctions from the resulting pseudowavefunctions. In principle this should also work for the final state.

We used the GPAW code [63] to test this hypothesis. GPAW provides functions to reconstruct the all-electron wavefunction and electrostatic potential. Extracting the corresponding Kohn-Sham potential was, however, less straightforward. We used the all-electron density to calculate the Kohn-Sham potential in the LDA according to the parameterization proposed by Perdew and Zunge [64], but unfortunately the resulting photoemission matrix element did not converge in a reasonable amount of time and effort. And so we refrain from including the results and have to leave it as an item for the to-do list. Incidentally, it might be advantageous to use a localized basis DFT code, such as NWChem [65], that employs all-electron calculations throughout, for an implementation.

Inaccurate functional. Regardless of whether pseudo or all-electron wavefunctions are used, more accurate functionals might also lead to an improvement. Both the Kohn-Sham wavefunctions and the binding energies are affected by the choice of the functional. As we have seen in Chapter 2.4.3, the binding energy directly affects the photoemission intensity as the photon frequency ω depends on it via

$$\omega = E_{\text{kin}} + E_{\text{bind}}. \tag{5.14}$$

This would mainly change the cross section at low photon, or equivalently, photoelectron kinetic, energies.
For the systems that we tested, it made practically no difference whether LDA or GGA was used. A hybrid functional might lead to noticeable differences. In particular, a range-separated long-range-corrected hybrid functional, such as CAM-B3LYP [66], which should exhibit the correct $\frac{1}{r}$ long-range behavior as opposed to LDA or GGA, which both decay exponentially, should be tested.

General failure of DFT. Even with an elusive exact functional the matrix element might still come out wrong for the simple reason that the Kohn-Sham orbitals and potential have no direct physical meaning.

5.5 Some numerical and technical details

All results reported here were obtained with the Julia DFTK code [57], which uses norm-conserving pseudopotentials. The Kohn-Sham pseudopotential can be extracted from the code and then used in the LS equation. We use the trapezoidal rule [67] for the discretization of the integrals. Since the method developed in this chapter only uses the radial coordinates, the resulting linear system of equations can be solved by direct methods as opposed to iterative methods.

Chapter 6

Real space approach

The method described in the previous chapter is only applicable to physical systems that exhibit radial symmetry, i.e., isolated atoms. The focus of this thesis, however, lies on the photoemission properties of more complex systems, such as molecules or molecules on surfaces. All experiments of interest to us in this thesis are performed on molecular films on metal substrates. Nevertheless, the photoemission properties of these systems are, for an adequate range of photoelectron energies relative to the photon energy, often dominated by the properties of the isolated molecule. That is, also effects arising from intermolecular interactions in the molecular film may be neglected.

We therefore here describe a method that is capable of handling isolated gas-phase molecules. The 3d real-space approach (as we will call this method) is, in comparison to the radial approach, more difficult to implement with regard to two aspects. First, the memory demand increases very rapidly with system size. And second, the singularity in the Green function must be dealt with more directly. For a radial potential, there is obviously no need to resort to the full 3d calculation, while it still provides an ideal benchmark for the 3d method, especially regarding the singularity subtraction scheme(s).

As we have seen in the toy model Chapter 4, the Born approximation, though more straightforward and simpler than solving the full Lippmann-Schwinegr equation, is not applicable and will therefore not be pursued here.

Turning to the full Lippmann-Schwinger equation (2.13), the three-dimensional integral necessitates the use of a rolled-up index, so (x_i, y_j, z_k) will be denoted by $\boldsymbol{r}_l$, where i is the fastest index and k the slowest one. Denoting $\psi_{\boldsymbol{k}}(\boldsymbol{r}_l)$ and $V(\boldsymbol{r}_l)$ as $\psi_{\boldsymbol{k},l}$

and V_l, respectively, leads to the following discretization of the integral

$$\int d^3r' G_0^*(\boldsymbol{r}, \boldsymbol{r}') V(\boldsymbol{r}') \psi_{\boldsymbol{k}}(\boldsymbol{r}') \approx \sum_l w_l G_0^*(\boldsymbol{r}, \boldsymbol{r}_l') V_l \psi_{\boldsymbol{k},l}. \tag{6.1}$$

Here, w_l is given by the product of the three weight functions ($w_l = w_i w_j w_k$). $\psi_{\boldsymbol{k}}(\boldsymbol{r})$ is now evaluated on the same grid points that are used for the computation of the integral, i.e., $\boldsymbol{r} = \boldsymbol{r}_i$. With $K_{il} \equiv w_l G_0^*(\boldsymbol{r}_i, \boldsymbol{r}_l') V_l$ the integral equation takes the following form [67]

$$\psi_{\boldsymbol{k},i} = \phi_i + \sum_l K_{il} \psi_{\boldsymbol{k},l}, \tag{6.2}$$

or, upon rearranging the equation

$$\sum_l (\delta_{il} - K_{il}) \psi_{\boldsymbol{k},l} = \phi_{\boldsymbol{k},i}. \tag{6.3}$$

The solution of this system of linear equations only yields the wave function at the grid points of the integration. The values at other positions, however, can be obtained from Eqn.(6.2) as needed. The evaluation of the matrix element also proceeds by discretization. Working in the velocity gauge, we get

$$\langle \psi_{\boldsymbol{k}} | \, \boldsymbol{Ap} \, | \psi_{\text{ini}} \rangle \approx \sum_l w_l \psi_{\boldsymbol{k},l} \boldsymbol{Ap}_l \psi_{\text{ini},l} \tag{6.4}$$

The diagonal matrix elements in K need a bit more care. The Green function in real space diverges at $\boldsymbol{r}' \approx \boldsymbol{r}$; nevertheless the integral around $\boldsymbol{r}' \approx \boldsymbol{r}$ only gives a vanishingly small contribution. This can be easily seen in spherical coordinates:

$$\int d^3r G_0^*(\boldsymbol{r}) \propto \int_\epsilon d^3r \frac{e^{-ik|\boldsymbol{r}|}}{|\boldsymbol{r}|} \propto \int_0^\epsilon dr r e^{-ikr} \approx \epsilon^2, \tag{6.5}$$

where ϵ denotes the radius of a spherical region around the origin that is used for the evaluation of the integral (numerically ϵ is proportional to the grid spacing employed in the code). The last step above follows from dimensional analysis.

Proceeding somewhat more carefully the integral appearing in (6.1)

$$\int d^3r' G_0^*(\boldsymbol{r}, \boldsymbol{r}') V(\boldsymbol{r}') \psi_{\boldsymbol{k}}(\boldsymbol{r}') \tag{6.6}$$

is split into an unproblematic part

$$\int_{|\boldsymbol{r}' - \boldsymbol{r}| > \epsilon} d^3r' G_0^*(\boldsymbol{r}, \boldsymbol{r}') V(\boldsymbol{r}') \psi_{\boldsymbol{k}}(\boldsymbol{r}') \tag{6.7}$$

that can be solved by discretization as described above and another part around $|\boldsymbol{r}' - \boldsymbol{r}| < \epsilon$

$$\int_{|\boldsymbol{r}'-\boldsymbol{r}|<\epsilon} d^3r' G_0^*(\boldsymbol{r}, \boldsymbol{r}') V(\boldsymbol{r}') \psi_{\boldsymbol{k}}(\boldsymbol{r}'). \tag{6.8}$$

This part can only be evaluated approximately. First, it is assumed that both V and $\psi_{\boldsymbol{k}}$ vary comparatively little in the small region $|\boldsymbol{r}' - \boldsymbol{r}| < \epsilon$, so that they can be pulled out of the integral

$$\int_{|\boldsymbol{r}'-\boldsymbol{r}|<\epsilon} d^3r' G_0^*(\boldsymbol{r}, \boldsymbol{r}') V(\boldsymbol{r}') \psi_{\boldsymbol{k}}(\boldsymbol{r}') \approx V(\boldsymbol{r}) \psi_{\boldsymbol{k}}(\boldsymbol{r}) \int_{|\boldsymbol{r}'-\boldsymbol{r}|<\epsilon} d^3r' G_0^*(\boldsymbol{r}, \boldsymbol{r}'). \tag{6.9}$$

$G_0^*(\boldsymbol{r}, \boldsymbol{r}')$ depends only on $|\boldsymbol{r} - \boldsymbol{r}'|$ so that the integral over the solid angle can be carried out trivially

$$\int_{|\boldsymbol{r}'-\boldsymbol{r}|<\epsilon} d^3r' G_0^*(\boldsymbol{r}, \boldsymbol{r}') = 4\pi \int_0^\epsilon dr_1 r_1^2 G_0^*(r_1). \tag{6.10}$$

Here, we subsitute $\boldsymbol{r}_1 = \boldsymbol{r} - \boldsymbol{r}'$ and denote the Green function by $G_0^*(\boldsymbol{r}, \boldsymbol{r}') = G_0^*(|\boldsymbol{r} - \boldsymbol{r}'|) = G_0^*(r_1)$. The remaining integral can be done analytically

$$4\pi \int_0^\epsilon dr_1 r_1^2 G_0^*(r_1) = -2 \int_0^\epsilon dr_1 r_1 e^{-ikr_1} = -2 \left(\frac{i\epsilon e^{-ik\epsilon}}{k} + \frac{1}{k^2}(e^{-ik\epsilon} - 1) \right). \tag{6.11}$$

Finally, the result is

$$\int_{|\boldsymbol{r}'-\boldsymbol{r}|<\epsilon} d^3r' G_0^*(\boldsymbol{r}, \boldsymbol{r}') V(\boldsymbol{r}') \psi_{\boldsymbol{k}}(\boldsymbol{r}') \approx -2 \left(\frac{i\epsilon e^{-ik\epsilon}}{k} + \frac{1}{k^2}(e^{-ik\epsilon} - 1) \right) V(\boldsymbol{r}) \psi_{\boldsymbol{k}}(\boldsymbol{r}). \tag{6.12}$$

At the photoemission threshold (i.e. $k = 0$) this expression must be replaced by

$$\int_{|\boldsymbol{r}'-\boldsymbol{r}|<\epsilon} d^3r' G_0^*(\boldsymbol{r}, \boldsymbol{r}') V(\boldsymbol{r}') \psi_{\boldsymbol{k}}(\boldsymbol{r}') \approx -\epsilon^2 V(\boldsymbol{r}) \psi_{\boldsymbol{k}}(\boldsymbol{r}). \tag{6.13}$$

ϵ is choosen in such a way that the volume of the sphere ($\frac{4}{3}\pi\epsilon^3$) is equal to the volume of the grid spacing δ (δ^3), i.e.

$$\epsilon = \delta \left(\frac{3}{4\pi} \right)^{1/3}. \tag{6.14}$$

6.1 Implementation using hierarchical matrices

Since we are dealing with pseudoorbitals, and hence a nonlocal potential, we will exclusively use the velocity gauge for the interaction Hamiltonian appearing in the photoemission matrix element, see Chapter 2.4.3. Also, as elucidated in Chapter 2.4.1, we will restrict ourselves to the dipole approximation.

6.1.1 Initial state calculations

If not otherwise mentioned, the initial state calculations are all carried out with the Julia [68] DFT code [57], with a GGA functional [31] and an energy cutoff of 15 Hartree. The pseudopotentials are taken from PseudoDojo, see [69]. See listing 6.1 for an example of an initial state calculation.

Listing 6.1: Initial state code

```
orbitals = [:homo4, :homo3, :homo2, :homo1, :homo, :lumo, :lumo1, :lumo2]
orbital_numbers = [116, 117, 118, 119, 120, 121, 122, 123]
extend_ccordinates = true

# Pseudopotential from Pseudodojo site
family_upf = PseudoFamily("dojo.nc.sr.pbe.v0_4_1.standard.upf")

E_cut = 15 # Hartree
temperature = 0.01
k_grid = [1, 1, 1]

data_path = joinpath(@__DIR__, "../../../../data/Molecules/C60")
# Load an xyz file; typically from a database
system = AtomsIO.load_system(joinpath(data_path, "213.xyz"))

# Specifiy the calculation parameters and carry out a self consistent
    calculation
model = model_DFT(
    system; functionals=PBE(), temperature, symmetries=true, pseudopotentials=
        family_upf
)
basis = PlaneWaveBasis(model; Ecut=E_cut, kgrid=k_grid)
scfres = self_consistent_field(basis)

# Obtain the Kohn-Sham hamiltonian
E, ham = energy_hamiltonian(basis, scfres.ψ, scfres.occupation; ρ=scfres.ρ)

# Extract the local potential
V_local = DFTK.total_local_potential(ham)

# Extract the desired orbitals
ψ_k_orbital = scfres.ψ[1][:, orbital_number]
ψ_real_orbital = ifft(basis, basis.kpoints[1], ψ_k_orbital)

# Extract the desired Kohn-Sham eigenvalues
E_bind_orbital = scfres.eigenvalues[1][orbital_number]
```

6.1.2 Memory Requirements

Since the storage demand increases rapidly with the system size, it becomes necessary to reduce the demand numerically. As a specific example, suppose our grid contains

one million coordinates—and most molecules in this thesis contain at least that many— then the LS-matrix (6.3) contains 10^{12} entries. Each entry is a complex number and hence the number of bytes is 16×10^{12}, which corresponds to 16 TB of RAM. The VSC-5 cluster, on which most of the simulations were run, has nodes with a maximum RAM of 2048 GB. As the method of this chapter is a proof-of-principle study at the moment, we wanted to avoid complications arising from sophisticated parallelization methods. Moreover, in this direct approach the number of grid points grows very rapildy with the cutoff energy of the initial state DFT calculation. The number of real space grid points is proportional to the number of wavevectors, which in turn is proportional to $E_{\text{cut}}^{3/2}$. This means that the storage demand of the LS-matrix increases as E_{cut}^{3}.

Two approaches have been tested to reduce the storage demand. The first method is the matrix-free operator approach, as implemented in the Julia SciML package [70]. This method would have been very convenient as it entails no further approximations, as opposed to the H-matrix method that we ended up using. Unfortunately, the resulting code was too slow to be useful, however.

The approach that is used throughout this chapter, however, is based on hierarchical matrices described next.

6.1.3 Hierarchical matrices

The basic idea of the hierarchical matrices, or H-matrices, is to divide the original matrix into submatrices, which are subsequently approximated to reduce the storage demand [71]. The basic algorithm behind this reduction of storage is the adaptive cross approximation (ACA) method. Here, we only give a very rough outline of the method based on the clear presentation in [72]. More detailed accounts can be found in [71, 73, 74]. The basic idea is to approximate the effect of the original submatrix multiplication by the direct product of one column and row of that submatrix. After this initial step, the same procedure is applied to the residual matrix until convergence is reached. This procedure can also be used to calculate (approximate) LU-factorizations and the eigenvalue spectrum of the original matrix [71].

It should be mentioned that a similar method exists to compress matrices, namely the H^2 method, see Ref. [71]. This method is more suitable for the oscillating kernels that we are dealing with [75], but unfortunately no Julia implementation is available yet. Nevertheless, by employing the H-matrix technique, we were able to decrease the storage demand by around two orders of magnitude, which is sufficient for our purposes.

For the actual Julia implementation of the H-matrix method, see [76]. The pack-

age is still relatively immature. Although the LU-factorization is implemented, it is slow because it is so far restricted to running on a single core. As a result, the momentum maps that we will show in this chapter each took around one day of computing time. The constant-initial state (CIS)-scans with 100 points took similarly long. Another limitation of the Julia package is that it is not yet capable of calculating the eigenvalue spectrum of H-matrices, which would be very useful to test the initial state calculation in the LS-formalism.

6.1.4 Momentum maps

The magnitude of the wavevector is constant across a momentum map. It is therefore computationally expedient to factorize the LS-equation (6.3) once and use the factorized matrix to solve the LS-equation for every point on the momentum map. Fortunately, the LU-decomposition is implemented in the H-matrix package [76]. Once the final state for a particular $\boldsymbol{k}_{\parallel}$ has been determined, the matrix element (6.4) can be calculated for a given polarization configuration. The extra computational cost of calculating more than one polarization configuration is negligible.[1] See listing 6.2 for an example of how to run a momentum map calculation.

Listing 6.2: Momentum map code

```
molecule_name = :PTCDA
orbital = :homo
E_cut = 15
use_nonlocal_potential_in_final_state = true # Using the nonlocal potential
    might take a good deal longer

# Calc parameters
E_kin = 30
nx = 101 # number of x componetns of momentum map
ny = 101
kx_max = 2.7
ky_max = 2.7

# Define the poalrization configurations
polarizations = (
    x_lin = RealSpacePhotoemission.linear_polarization(0.0, 0.0),
    y_lin = RealSpacePhotoemission.linear_polarization(0.0, 90.0),
    z_lin = RealSpacePhotoemission.linear_polarization(90.0, 0.0),
    nano_esca_x = RealSpacePhotoemission.linear_polarization(65.0, 0.0),
    nano_esca_y = RealSpacePhotoemission.linear_polarization(65.0, 90.0),
    right_circ_x = [0, -im, 1],
    left_circ_x = [0, im, 1],
    right_circ_y = [im, 0, 1],
    left_circ_y = [-im, 0, 1],
```

[1] This is an advantage over the time-dependent density functional theory to be introduced later.

```
    right_circ_z = [1, im, 0],
    left_circ_z = [1, -im, 0],
    toroidal=RealSpacePhotoemission.linear_polarization(40.0, 0.0),
)

# Beginning of code
kx_vec = collect(range(-kx_max, kx_max, length=nx))
ky_vec = collect(range(-ky_max, ky_max, length=ny))
k_parallel = RealSpacePhotoemission.WavevectorParallel(kx_vec, ky_vec)

# Load the initial state data
data_path = joinpath(@__DIR__, "../../../data/Molecules/$molecule_name/")
grid_coordinates = Serialization.deserialize(joinpath(data_path, "
    grid_coordinates_$(E_cut).jls"))
V_local = Serialization.deserialize(joinpath(data_path, "V_local_$(E_cut).jls"))
# nonlocal_pot = Serialization.deserialize(joinpath(data_path, "V_nonlocal_$(
    E_cut).jls"))
psi_in = Serialization.deserialize(joinpath(data_path, "psi_initial_$(orbital)
    _$(E_cut).jls"))
E_bind = Serialization.deserialize(joinpath(data_path, "E_bind_$(orbital)_$(
    E_cut).jls"))
nonlocal_potential_struct = if use_nonlocal_potential_in_final_state
    Serialization.deserialize(joinpath(data_path, "V_nonlocal_struct_$(E_cut).
        jls"))
else
    nothing
end

# Calculate the matrix elements (only the velocity gauge is used, but the length
     gauge is still calculated)
me_pw_vel, me_ls_vel, overlap_pw, overlap_ls, me_pw_length, me_ls_length =
    RealSpacePhotoemission.calculate_momentum_map(
    k_parallel, E_kin, grid_coordinates, psi_in, V_local,
        nonlocal_potential_struct, polarizations
)
```

6.1.5 Constant-initial state scans

For CIS-scans it makes more sense to use iterative matrix methods. Krylov space methods are the method of choice. The Julia implementation can be found in [77]. The BICGSTAB- and GMRES-algorithms seem to work equally well. Although a preconditioner could significantly boost the performance, none is used for this thesis. Since the different final state kinetic energy calculations are completely independent of each other, it is straightforward to let the computation run on more than one computing node. See listing 6.3 for an example of how to run a CIS-scan calculation.

Listing 6.3: CIS-scan code

```
use_nonlocal_potential_in_final_state = true # Using the nonlocal potential
    might take a good deal longer
molecule_name = :PTCDA
E_cut = 15 # refers to the initial state calculation
orbital = :homo

# Calc parameters
k_parallel_fixed = [1.24, 0.7]
n_ph = 100 # number of photon energies

azimuth = atand(k_parallel_fixed[2], k_parallel_fixed[1])
polarizations = (
    x_lin = RealSpacePhotoemission.linear_polarization(0.0, 0.0),
    y_lin = RealSpacePhotoemission.linear_polarization(0.0, 90.0),
    z_lin = RealSpacePhotoemission.linear_polarization(90.0, 0.0),
    nano_esca_x = RealSpacePhotoemission.linear_polarization(65.0, 0.0),
    nano_esca_y = RealSpacePhotoemission.linear_polarization(65.0, 90.0),
    right_circ_x = [0, -im, 1],
    left_circ_x = [0, im, 1],
    right_circ_y = [im, 0, 1],
    left_circ_y = [-im, 0, 1],
    right_circ_z = [1, im, 0],
    left_circ_z = [1, -im, 0],
    toroidal=RealSpacePhotoemission.linear_polarization(40.0, azimuth),
)

# load the initial state data
data_path = joinpath(@__DIR__, "../../../data/Molecules/$molecule_name")
grid_coordinates = Serialization.deserialize(joinpath(data_path, "
    grid_coordinates_$(E_cut).jls"))
V_local = Serialization.deserialize(joinpath(data_path, "V_local_$(E_cut).jls"))
# nonlocal_pot = Serialization.deserialize(joinpath(data_path, "V_nonlocal_$(
    E_cut).jls"))
psi_in = Serialization.deserialize(joinpath(data_path, "psi_initial_$(orbital)
    _$(E_cut).jls"))
E_bind = Serialization.deserialize(joinpath(data_path, "E_bind_$(orbital)_$(
    E_cut).jls"))
nonlocal_potential_struct = if use_nonlocal_potential_in_final_state
    Serialization.deserialize(joinpath(data_path, "V_nonlocal_struct_$(E_cut).
        jls"))
else
    nothing
end

# Define the desired kz or E_kin range
k_parallel_norm = LinearAlgebra.norm(k_parallel_fixed)
E_kin_min = 1/E_kin_to_k_squared * k_parallel_norm^2
E_kin = collect(range(E_kin_min, 60.0, length=n_ph))
k_abs = sqrt.(E_kin*E_kin_to_k_squared)
kz = sqrt.(abs.(k_abs.^2 .- k_parallel_norm^2))
abs(kz[1]) >= 1e-5 && error("kz[1] should be 0 by construction, but is $(kz[1])
    instead")

# Calculate the matrix elements (only the velocity gauge is used, but the length
     gauge is still calculated)
me_pw_vel, me_ls_vel, overlap_pw, overlap_ls = RealSpacePhotoemission.
```

```
    calculate_constant_initial_state_scan(
    kz, k_parallel_fixed, grid_coordinates, psi_in, V_local,
        nonlocal_potential_struct, polarizations, io
)
```

6.1.6 Discretization and singularity subtraction

We exclusively use the trapezoidal rule [67] to approximate the integrals in the LS-equation. The final state wave function is then evaluated on the same grid as the initial state calculation. This way, there is no need to adapt the weights of the integration scheme upon including the singularity subtraction method described in the beginning of this chapter.

6.2 Some simple tests

The radial method from the previous chapter allows for a simple comparison to assess the validity of the 3d approach. The discretization in the radial method, in contrast to the 3d approach, can be chosen arbitrarily small. Also, there is no need to resort to H-matrix methods there. Let us consider two simple examples.

First, the momentum map of hydrogen calculated by the new 3d method is shown in Fig. 6.1a. More revealingly, the difference to the results from the "radial" implementation according to Eq. (5.1) is shown in Fig. 6.1b. The agreement is satisfactory, but the slight asymmetry is unexpected. Small differences in the initial state calculation are amplified in the H-matrix method[2].

Second, and as a more stringent test, the constant-initial state (CIS)-scan is shown in Fig. 6.2a. Experimentally, this corresponds to a series of measurements where the photon energy is varied while keeping the initial state, classified by its binding energy relative to the vacuum energy, fixed. Fig. 6.2b depicts the relative difference of the two approaches in percent. The agreement is again satisfactory.

These examples demonstrate that the resulting photoemission spectra are already converged at the rather low initial state calculation energy cutoff of 15 Hartree, which serves as a standard cutoff in this chapter.

[2] Alternatively, there might still, alas, be an error in the code somewhere.

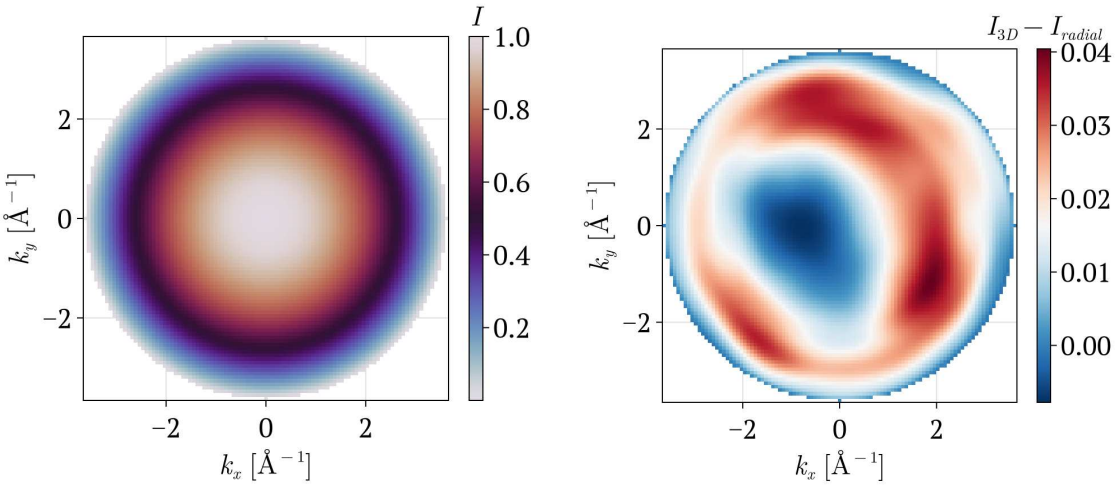

(a) 3d approach

(b) Difference between the methods.

Figure 6.1: Intensity of the 1s photoemission of hydrogen. The polarization is in z-direction. The kinetic energy is 50 eV.

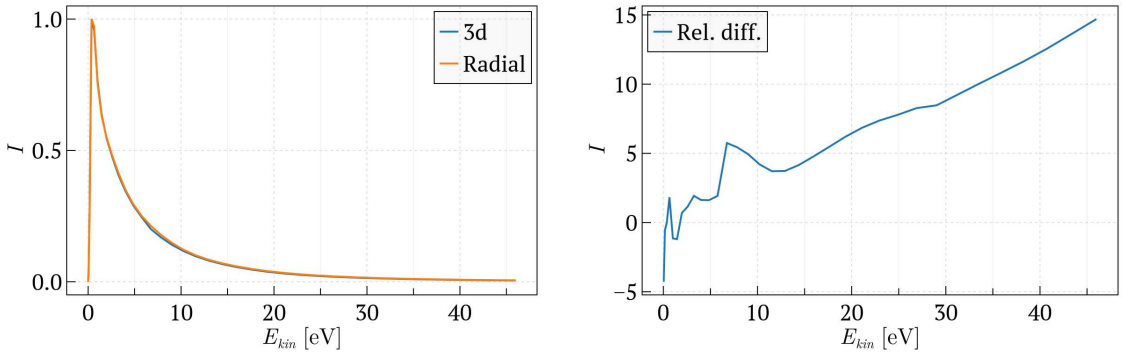

(a) CIS-scan

(b) Relative difference of plots in %.

Figure 6.2: Intensity of the 1s photoemission of hydrogen as a function of the kinetic energy. The polarization is in z-direction.

6.3 Addressing shortcomings of the plane-wave approximation

To illustrate the method, we turn to some well-known shortcomings of the plane-wave approximation for the final state [13]. These shortcomings are both of a qualitative nature, such as the failure to account for circular dichroism and certain polarization configurations, and a quantitative nature in, e.g., the photon-energy dependence of the intensity.

6.3.1 $\boldsymbol{A} \perp \boldsymbol{k}$ gives vanishing intensity

In the plane-wave approximation, the photoemission intensity perpendicular to the polarization vector $\boldsymbol{A}$ vanishes. This can be easily seen from the matrix element:

$$\langle \boldsymbol{k}|\boldsymbol{A}\boldsymbol{p}|\psi_{\text{in}}\rangle = \boldsymbol{A}\,\langle \boldsymbol{k}|\boldsymbol{p}|\psi_{\text{in}}\rangle = \boldsymbol{A}\boldsymbol{k}\,\langle \boldsymbol{k}|\psi_{\text{in}}\rangle\,, \tag{6.15}$$

which vanishes for $\boldsymbol{A} \perp \boldsymbol{k}$. However, both from experiment and more sophisticated simulation methods [19], it is known that the intensity does not vanish in general when the wavevector of the photoelectron is perpendicular to the polarization direction. Two molecules will serve to illustrate this point.

PTCDA

Perylenetetracarboxylic dianhydride (PTCDA) is a widely studied molecule in the field of organic electronics and has also been studied in the photoemission community, e.g. [78] and [79]. Of particular interest to us, PTCDA exhibits pronounced emission lobes perpendicular to the polarization direction [19].

The molecular structure of PTCDA is illustrated in Fig. 6.3. For simulating the photoemission intensity, we choose the polarization parallel to the long axis of the molecule, that is, the y-direction. The prediction of the plane-wave approximation is shown in the left panel of Fig. 6.4. Owing to the $\boldsymbol{A}\boldsymbol{k}$ polarization factor in the plane-wave approximation, the emission features along the x-axis are suppressed. The Lippmann-Schwinger solution, shown in the right panel of Fig. 6.4, in contrast, displays pronounced features along this direction. Experimental results, together with a time dependent density function theory (TDDFT) simulation [19], show a very similar pattern. Based on the plane-wave momentum map alone, it would be hard to attribute the emission features to the HOMO of PTCDA.

Incidentally, the additional spots orthogonal to the polarization direction in the momentum map display a strong dependence on the photon energy, in contrast to

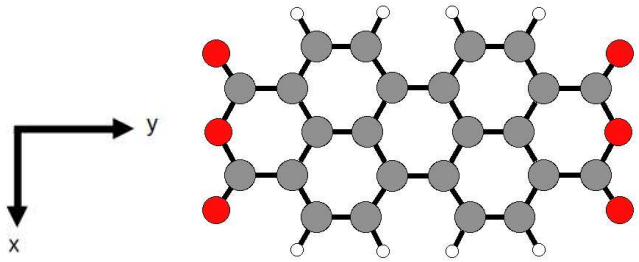

Figure 6.3: Molecular structure of PTCDA.

the plane-wave features of the map (i.e. those parts of the map that also appear in the plane-wave approximation). This is illustrated in Fig. 6.5, which shows a lower kinetic energy of 15 eV. The difference between the plane-wave and Lippmann-Schwinger approaches tends to zero for high kinetic energies, but the decrease need not be monotonic, as is illustrated by this example. This observation is stressed in Ref. [80].

Bisanthene

Another example illustrating this point is provided by bisanthene, whose molecular structure is shown in Fig. 6.6. For a recent photoemission study of bisanthene, see Ref. [81]. Depending on the polarization vector, the HOMO momentum maps calculated with the two approaches can show significant differences, as can be seen in Fig. 6.7. The emission features along the k_y-axis are completely absent in the PWA. Even points slightly removed from k_y-axis, which need not vanish by construction, barely show any intensity. Since the PWA fails even on qualitative level here, another comparison is called for to assess whether the new features in the LS momentum maps are qualitatively correct. For a more detailed comparison we turn to unpublished time dependent density functional theory (TDDFT) data from Christian Kern, obtained with the Octopus code [82]. We focus on the HOMO and HOMO-1 orbitals. As can be seen in Fig. 6.8, the difference between the three approaches is negligible when the polarization vector points along the z-direction.

In contrast, the differences are striking for polarization vectors pointing along either the x-axis or the y-axis, see Figs. 6.9 and 6.10 respectively. Owing to the $\boldsymbol{Ak}$ polarization factor, the plane-wave approximation (PWA) cannot account for features orthogonal to the polarization vector. But the differences extend beyond this obvious shortcoming. The shape of the main lobes in the PWA of the HOMO in Fig. 6.9 are spherical, while they are noticeably distorted in both the LS and TDDFT

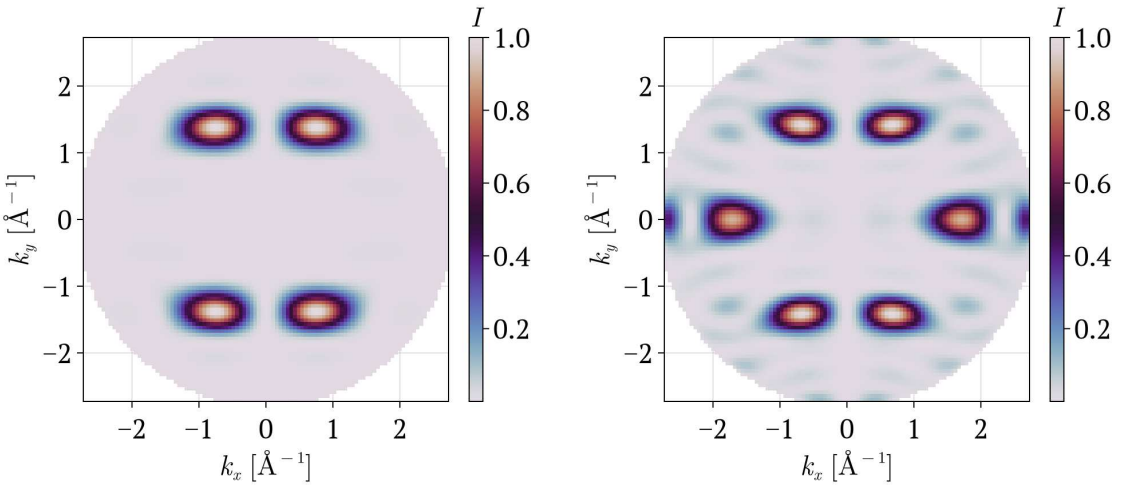

(a) Plane-wave approximation

(b) Lippmann-Schwinger

Figure 6.4: Intensity of the HOMO photoemission of PTCDA. The polarization is in y-direction. The kinetic energy is 30 eV.

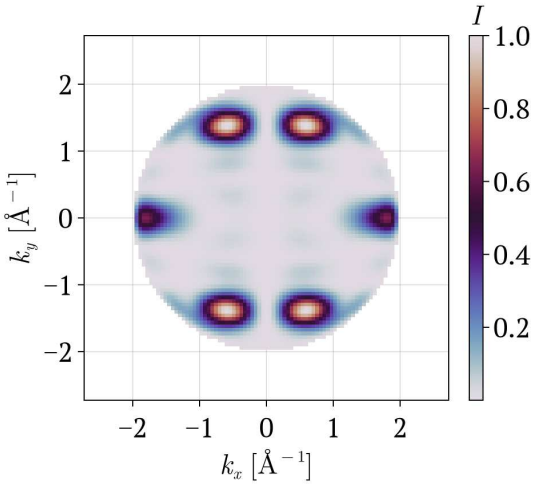

Figure 6.5: Same as Fig. 6.4b, but with a kinetic energy of 15 eV instead of 30 eV.

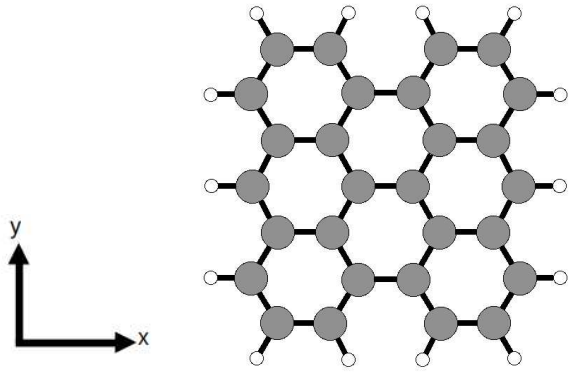

Figure 6.6: Molecular structure of bisanthene.

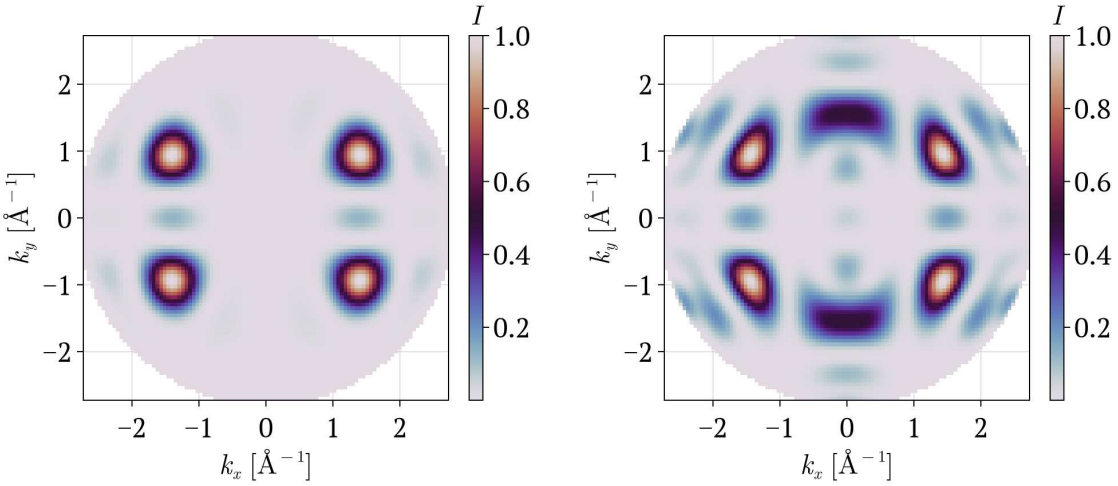

(a) Plane-wave approximation

(b) Lippmann-Schwinger

Figure 6.7: Intensity of the HOMO photoemission of bisanthene. The polarization is in x-direction. The kinetic energy is 30 eV.

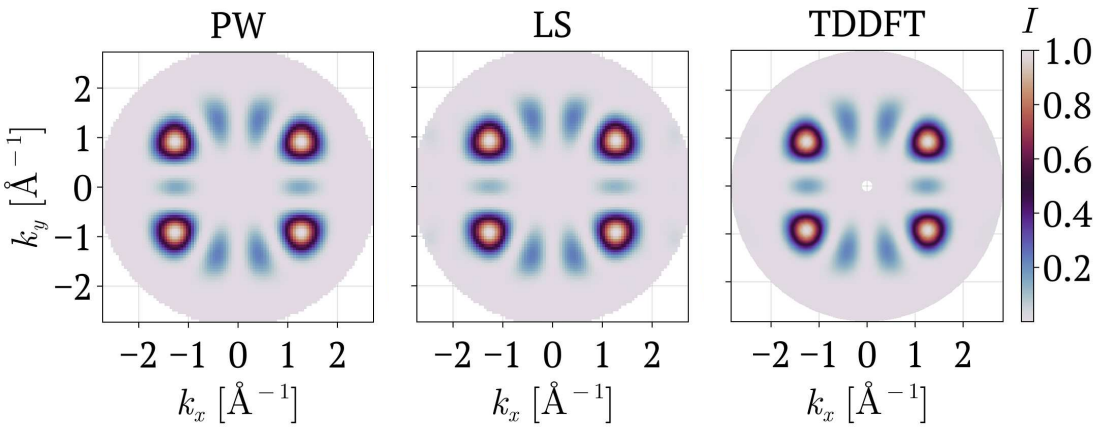

(a) HOMO

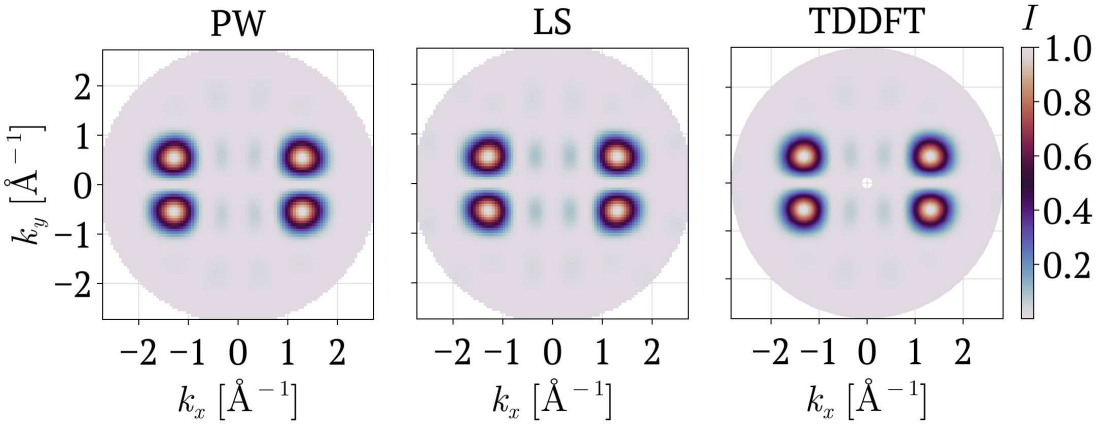

(b) HOMO-1

Figure 6.8: Bisanthene momentum maps. The polarization points in the z-direction. The kinetic energy of the photoelectrons is 30 eV. The orbitals are specified in the subfigure captions.

approaches. The additional features in the HOMO differ somewhat between the LS and TDDFT methods: the additional TDDFT features are more connected than they are in the LS calculation. The HOMO-1 differs mainly in the relative intensity of the new features; their intensity is higher in the LS simulation. The same observation applies to the HOMO of Fig. 6.10. The main features of the HOMO-1 agree in the LS and TDDFT approaches, but their intensity distribution differs markedly.

Our LS-approach, however, exhibits a clear advantage over the TDDFT method when it comes to the simulation of photoemission momentum maps for orbitals which are unoccupied in the gas-phase. While experimentally, there is often static charge transfer into the LUMO orbital, thereby making it observable in the photoemission, TDDFT cannot deal with such previously unoccupied orbitals. The PWA and LS predictions for the LUMO are shown in Fig. 6.11. No difference is discernible for a polarization vector pointing along the z-direction. The difference is again most pronounced for a polarization vector along the x-axis. New features appear, and the relative intensity of these features also shifts. In contrast, only some side features around $|k_x| \approx 1.5$ Å and $|k_y| \approx 1.0$ Å are enhanced in Fig. 6.10c.

A measurement campaign is planned for March 2026 in Japan to investigate bisanthene on Cu(110) [83]. The HOMO-1, HOMO and LUMO should all be visible in this experiment and will provide a benchmark for our prediction from the LS approach.

6.3.2 Circular dichroism

The plane-wave approximation is similarly incapable of accounting for the circular dichroism seen in the photoemission of both chiral and achiral molecules [19, 84, 85]. This is easy to demonstrate for a light beam along the z-direction. In this case

$$\boldsymbol{Ak} \propto k_x \pm ik_y \tag{6.16}$$

and so

$$|\boldsymbol{Ak}|^2 \propto k_x^2 + k_y^2, \tag{6.17}$$

independent of whether right- or left-handed circularly polarized light is employed. We will use the following normalization convention for the dichroism signal:

$$I_{cd} = \frac{I_{\text{right}}}{I_{\text{right,max}}} - \frac{I_{\text{left}}}{I_{\text{left,max}}}, \tag{6.18}$$

i.e. each intensity distribution is first normalized by its corresponding maximum. For momentum maps, the effect goes under the name of circular dichroism in the angular distribution (CDAD).

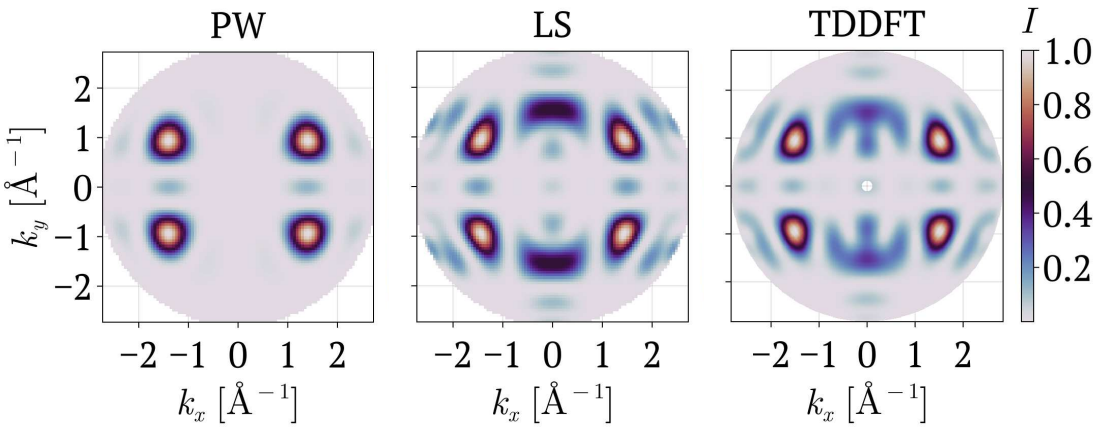

(a) HOMO

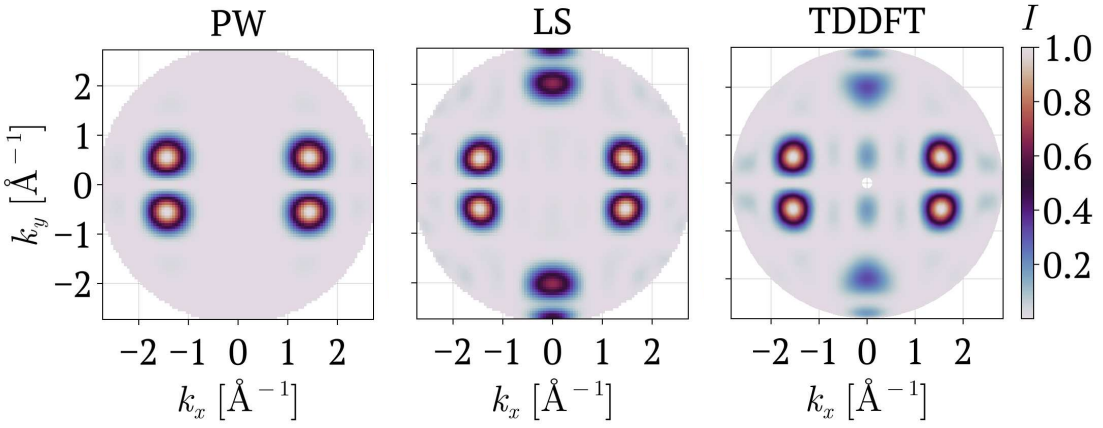

(b) HOMO-1

Figure 6.9: Bisanthene momentum maps. The polarization points in the x-direction. The kinetic energy of the photoelectrons is 30 eV. The orbitals are specified in the subfigure captions.

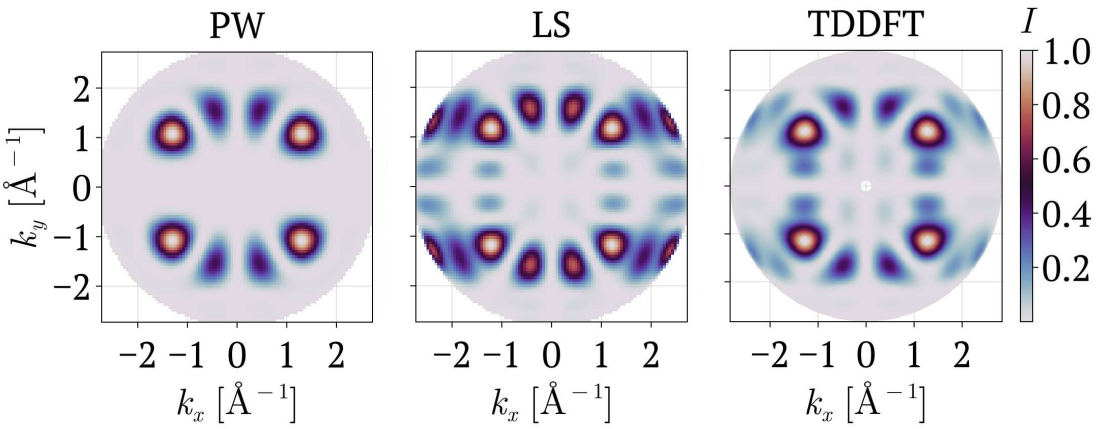

(a) HOMO

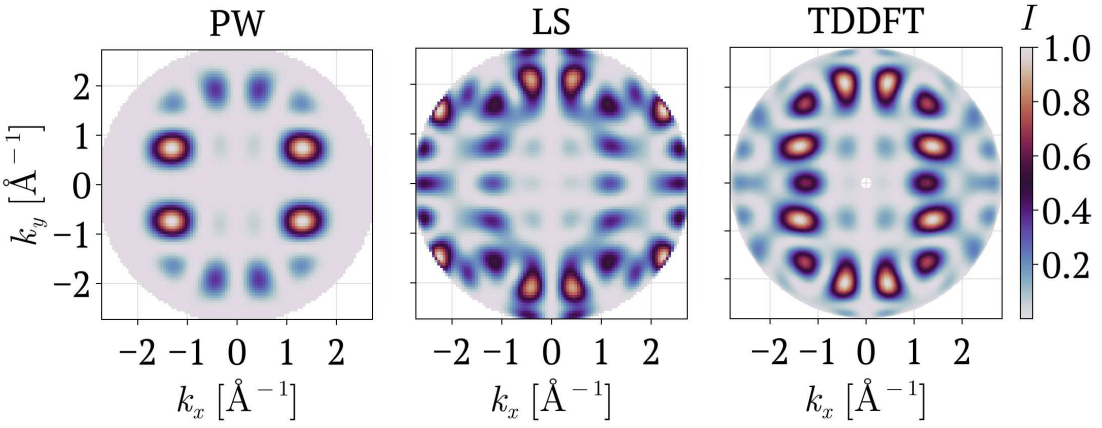

(b) HOMO-1

Figure 6.10: Bisanthene momentum maps. The polarization points in the y-direction. The kinetic energy of the photoelectrons is 30 eV. The orbitals are specified in the subfigure captions.

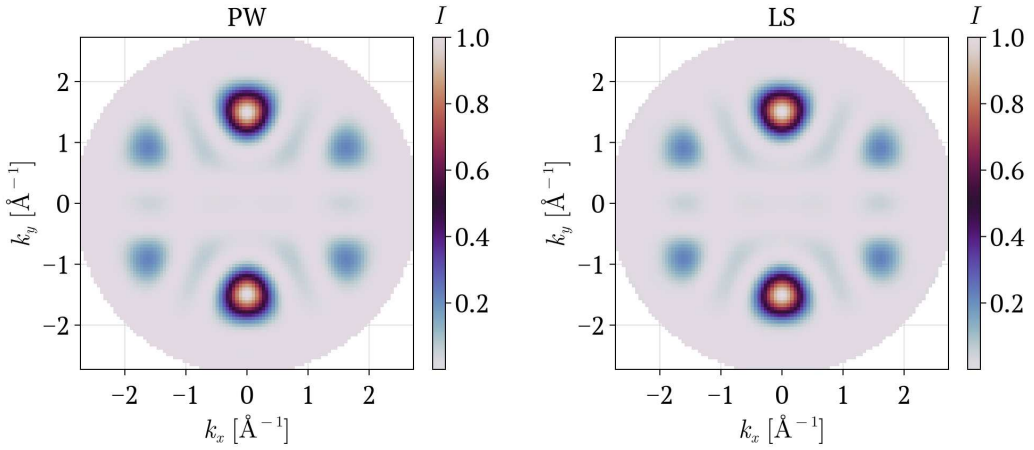

(a) Polarization vector points along the z-direction.

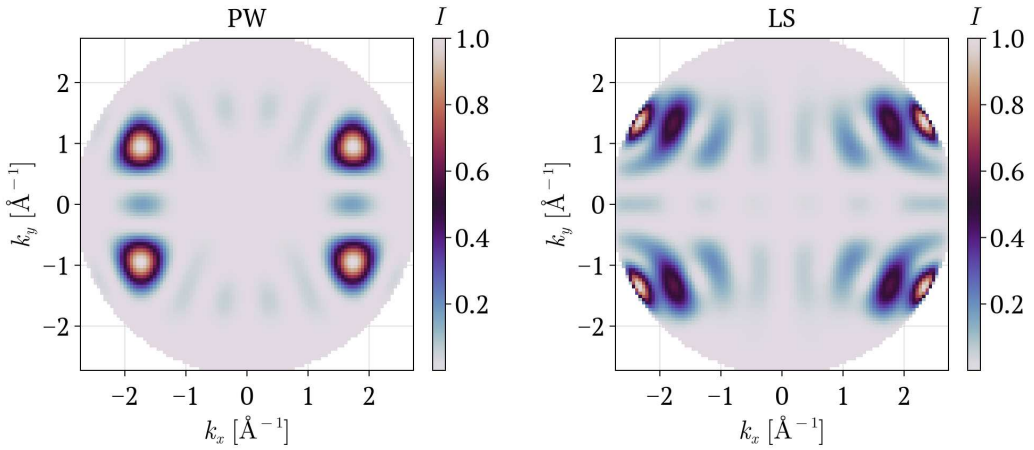

(b) Polarization vector points along the x-direction.

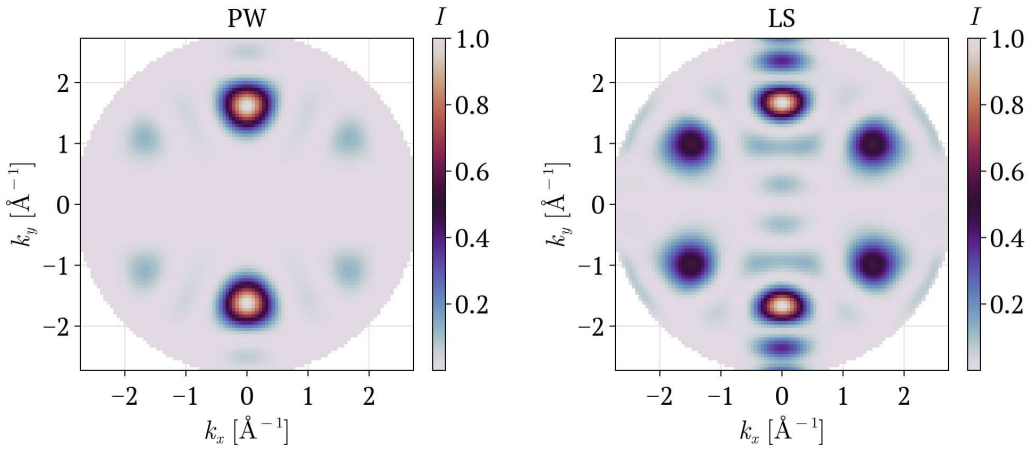

(c) Polarization vector points along the y-direction.

Figure 6.11: LUMO Bisanthene momentum maps. The kinetic energy of the photoelectrons is 30 eV. The direction of the polarization vector is indicated in the subfigure captions.

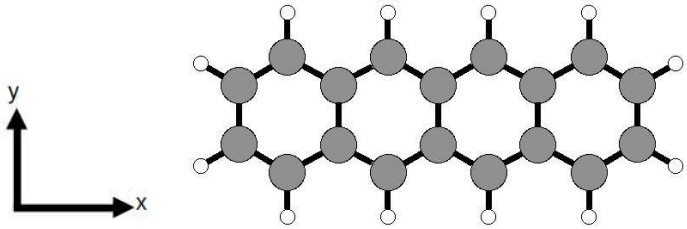

Figure 6.12: Molecular structure of tetracene.

Tetracene

Contrary to the prediction of the plane-wave approximation, the CDAD can be substantial. We illustrate the size of the effect with tetracene, see Fig. 6.12 for the molecular structure. A detailed comparison with another method [85], time dependent density functional theory (TDDFT), is shown in Fig. 6.13. Two things are apparent. First, the overall sign of the maps is wrong for the maps in Figs. 6.13b and c, but not in Fig. 6.13a. The opposite sign in the CDAD maps may be due to a different convention regarding the handedness of circularly polarized light applied in Ref. [85] compared to our choice. Unfortunately, this issue could not be resolved before finalizing this thesis. In addition, the shapes of the maps differ significantly. The TDDFT maps in Figs. 6.13a and b show more bent features than the rather straight features of the corresponding LS maps. The two approaches, however, lead to very similar results in Fig. 6.13c, apart from the sign issue. The results are promising and should be further investigated in the future.

6.3.3 Photon-energy dependence

Yet another shortcoming of the PWA is its inability to properly account for the photon-energy dependence of the intensity. As a rule, the PWA often only exhibits one maximum in a constant-initial state (CIS)-scan, while in reality many more maxima can appear. Also, since the Fourier transform of an odd orbital with respect to reflection in z vanishes for $k_z = 0$, i.e.,

$$\tilde{\psi}(k_x, k_y, k_z = 0) \propto \int dz \psi(x, y, z) = 0, \tag{6.19}$$

the PWA at threshold, that is, $k_z = 0$, must necessarily vanish for such an orbital, even if the parallel momentum component of the plane-wave is nonvanishing.

In the following, we will perform simulations that are suitable for comparison with experimental data from a toroidal electron energy analyzer [86]. For such an

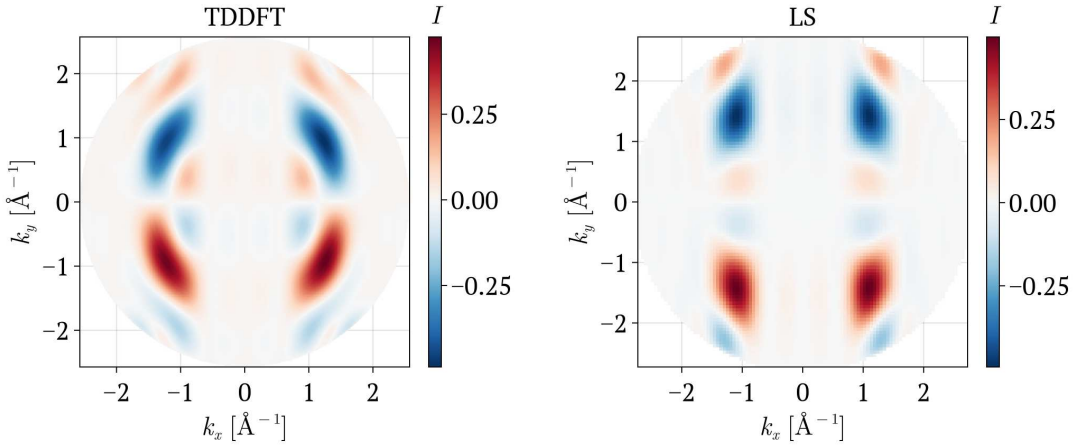

(a) $\boldsymbol{A} \propto (0, \mp i, 1)$

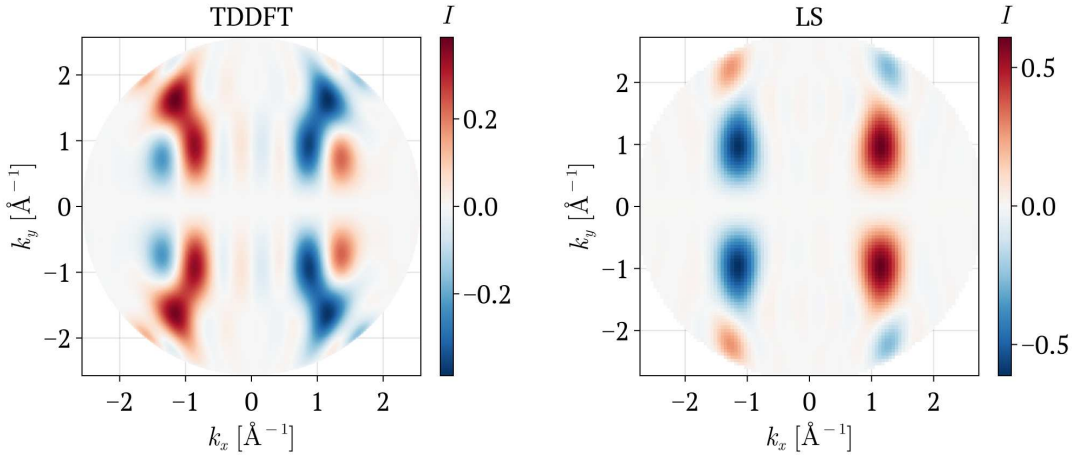

(b) $\boldsymbol{A} \propto (\pm i, 0, 1)$

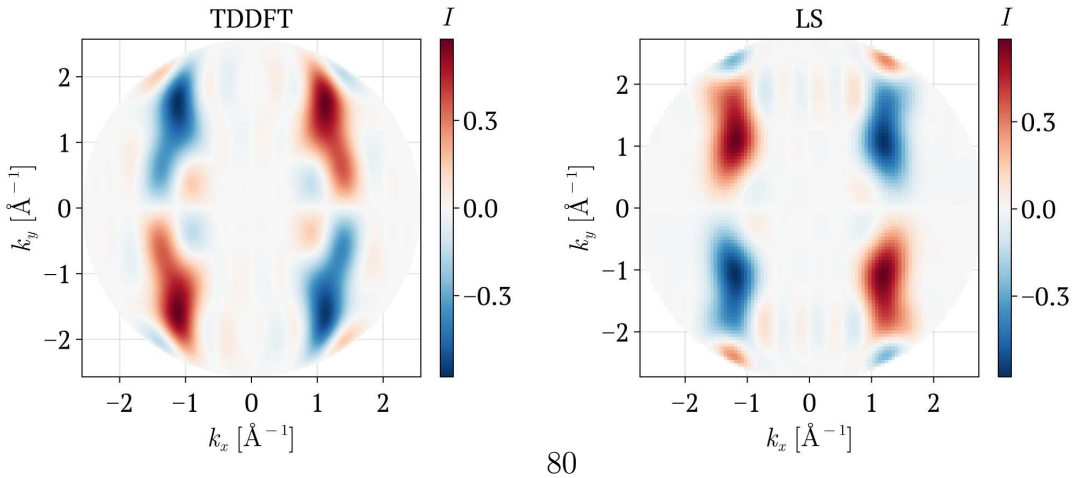

(c) $\boldsymbol{A} \propto (1, \pm i, 0)$

Figure 6.13: Intensity of the HOMO CDAD of tetracene. The kinetic energy is 30 eV. The polarization vector is given in the subfigure captions; the upper sign corresponds to right-handed circularly polarized light. The TDDFT simulations and polarization directions are taken from [85].

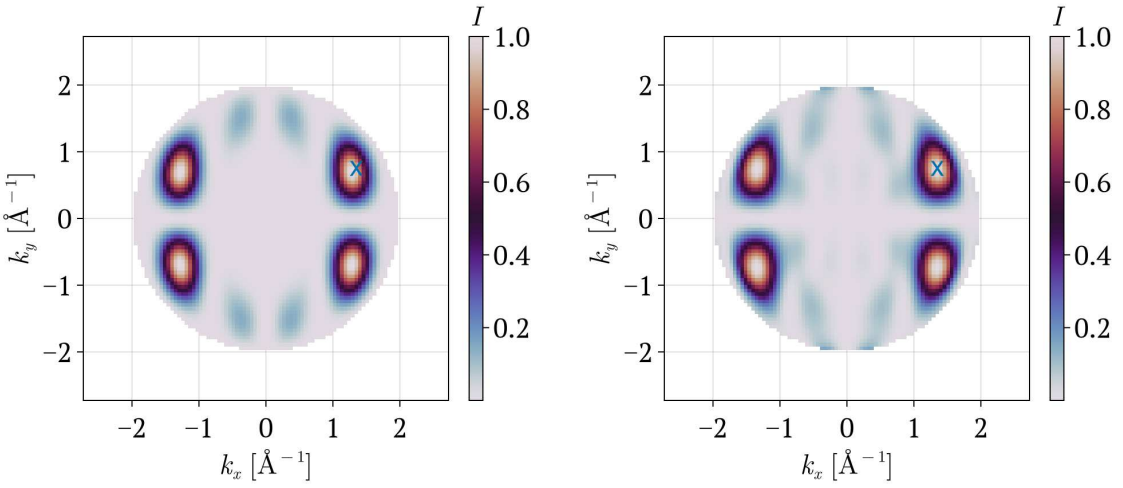

(a) Plane-wave approximation

(b) Lippmann-Schwinger

Figure 6.14: Intensity of the HOMO photoemission of gas-phase PTCDA. The polarization geometry is toroidal (see main text). The kinetic energy is 15 eV.

analyzer, a full (k_x, k_y)-momentum map is obtained by rotating the sample around the azimuth and collecting the photoelectrons in the plane of incidence. The angle of incidence relative to the z-axis is 40 degree.

To begin with, Fig. 6.14 shows a momentum map of gas-phase PTCDA. This molecule was investigated in [87] on a Ag(110) surface. Upon adsorption, the geometry of the molecule will, due to the new chemical environment, undergo changes. In particular, the oxygen atoms of the previously flat PTCDA molecule shift their position; some approach the surface, while others move up. The overall distance in z between the closest and farthest O-atom is roughly 0.2 Å [88]. Are these changes discernible in the photoemission spectra? Fig. 6.15 shows the momentum maps in the adsorption geometry. The momentum maps in the PWA are almost indistinguishable, while the changes in the LS approach are more marked, but still rather small. Specifically, the main lobes are a slightly more stretched into the y-direction and the side features between the main lobes appear to be slightly more pronounced and connected.

For the CIS-scans we investigate the intensity at the $\boldsymbol{k}_\parallel$ corresponding to the maximum of each momentum map shown (the maximum with positive k_x and k_y to be precise, i.e., $k_x \approx 1.3$ Å and $k_y \approx 0.7$ Å, see the crosses in Fig. 6.14) and keep it

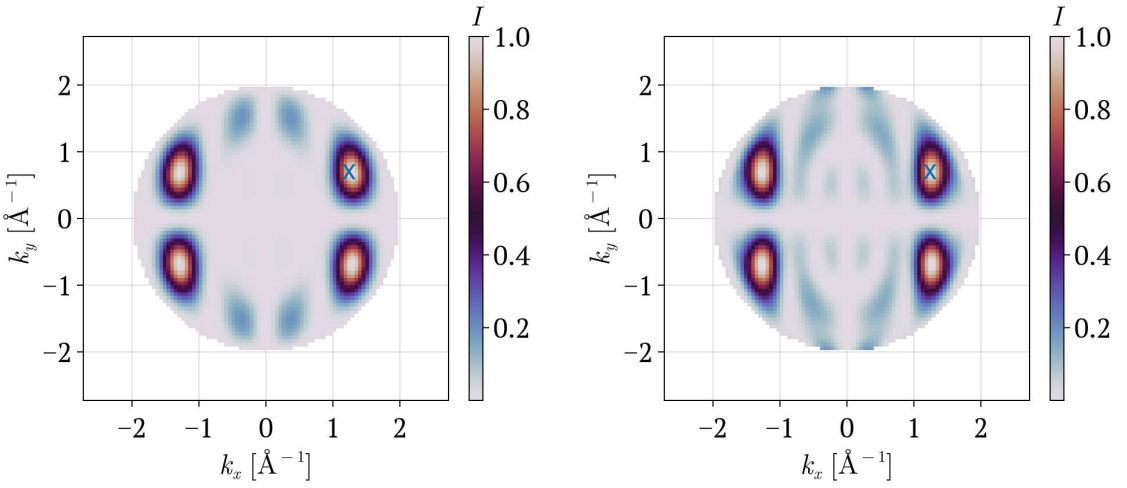

(a) Plane-wave approximation

(b) Lippmann-Schwinger

Figure 6.15: Same as in Fig. 6.14, but with the molecule in the adsorption geometry.

fixed as the photon energy varies.[3] The CIS-scan of gas-phase PTCDA is shown in Fig. 6.16a. The LS-curve differs significantly from the PW solution. First, the LS-curve is considerably more structured, with several maxima, than the PW-solution, which exhibits a single maximum around 20 eV final state kinetic energy. Second, in contrast to the PW-curve, the LS-curve does not vanish at threshold.

Fig. 6.16b shows the CIS-scan of PTCDA in the adsorption geometry. The $\boldsymbol{k}_{\parallel}$ at which the CIS-scan is taken is shown in Fig. 6.15 with crosses. Comparing Figs. 6.16a and 6.16b, it is clear that no drastic changes occur in the PW-solution upon adsorption. There is, however, quite a noticeable difference in the LS-solutions. In particular, the intensity of the second maximum at ≈ 22 eV increases significantly when taking into account the correct adsorption geometry.

For a more stringent test of the new method, we turn to the experimental data in [87]. The authors of the paper raised the issue whether the observed photon-energy dependence is due to some molecule-surface interaction or whether it simply results from the neglected final-state effects (the authors employed the PWA in their simulations). For an appropriate comparison with the experimental data, we average our simulation results by considering five (k_x, k_y)-points—namely $(k_x, k_y) = (1.3, 0.7)$

[3] The $\boldsymbol{k}_{\parallel}$ of the maximum may vary with the photon energy, but this effect is neglected here. The best option would be to average momentum maps over the region of interest. Later on we will include some form of averaging.

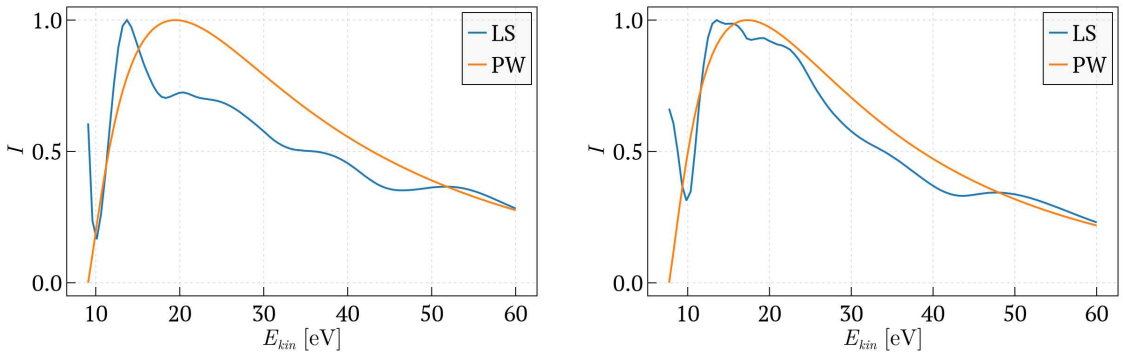

(a) Gas-phase geometry.

(b) Adsorption geometry.

Figure 6.16: Intensity of HOMO of PTCDA as a function of the kinetic energy of the photoelectron. The polarization geometry is toroidal (see main text). The crosses ("x") in Figs. 6.14 and 6.15 show the respective $\boldsymbol{k}_{\parallel}$ of the CIS-scan.

Å^{-1} for the gas phase and $(k_x, k_y) = (1.2, 0.7)$ Å^{-1} for the adsorption geometry - and the four neighboring points defined by $k_x \pm 0.1$ and $k_y \pm 0.1$ Å^{-1}. The results for the gas-phase and surface adsorbed LS solutions are shown in Fig. 6.17. Averaging apparently leads to the same qualitative features as solely including the maximum. The experimental data is taken from the paper [87]. In order to convert the photon energy of the radiation to the kinetic energy of the photoelectrons, we subtract the binding energy of the HOMO and the workfunction of the system, that is,

$$E_{\text{offset}} = E_{\text{bind}} + \Phi = 1.93 + 4.23 = 6.16 \text{ eV}, \tag{6.20}$$

where the data is from [79]. From the plot it is clear[4] that neither the gas-phase nor the surface configuration gets all features right. The gas-phase CIS-scan captures the shape of the curve around the first maximum well, but fails to give a second maximum of similar intensity as the first one. The adsorbed molecule CIS-scan indeed delivers a second maximum of comparable intensity, but falls short of reproducing the general shape of the curve after the first maximum. It should also be noted that the experimental data points around the second maximum become increasingly sparse with increasing kinetic energy, so the behavior is less certain there.

It should be mentioned that there are at least three different, but ultimately equivalent, ways of plotting CIS-scans. The x-axis can either correspond to the kinetic energy of the photoelectrons, as in the plots above, or to the perpendicular

[4]Note that we also normalize the simulation data to the maximum of the experimental data.

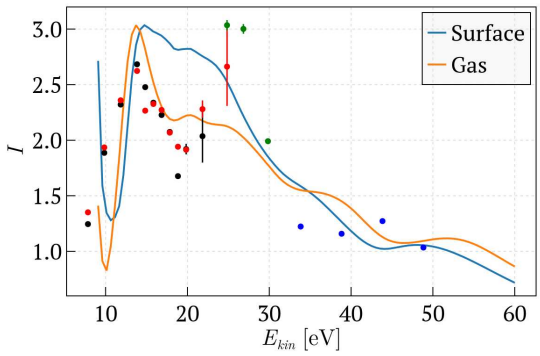

Figure 6.17: Same as Fig. 6.16, but only the Lippmann-Schwinger solutions, which are averaged as described in the main text, are shown, together with the experimental data as dots [79].

component of the wavevector, or to the photon energy. They are related by simple relations, such as

$$E_{\text{kin}} = \frac{\hbar^2}{2m}(k_{\parallel}^2 + k_{\perp}^2), \tag{6.21}$$

and

$$E_{\text{ph}} = E_{\text{kin}} + |E_{\text{bind}}|, \tag{6.22}$$

where E_{bind} is the binding energy of the orbital under consideration. The photon energy will lead to systematic deviations, however, as the binding energy always comes out too small in a DFT calculation.

6.3.4 Nonplanar molecules

While the PWA is often capable of accounting for the main photoemission features of planar [8, 13] or slightly nonplanar molecules [10], it seems to struggle with genuineley three dimensional molecules [14, 20]. The photoelectron-molecule interaction is not included in the PWA. Since this interaction is enhanced for a three-dimensional molecule, as the trajectory of the photoelectron gets closer to the molecule, the deviation from the experimental photoemission pattern is expected to be more pronounced in this case.

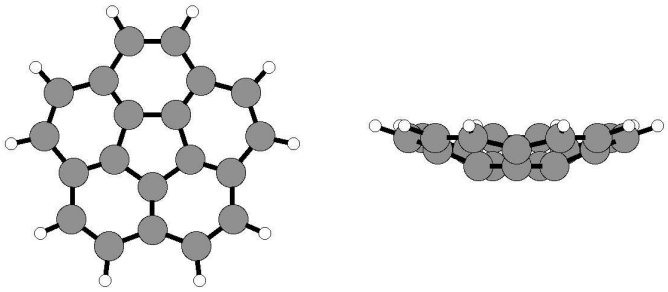

(a) xy-plane (b) xz-plane

Figure 6.18: Molecuar structure of corannulene.

Corannulene

Corannulene may be thought of as part of a fullerene/C60 molecule, in which a central pentagon of C atoms is surrounded by six hexagons. The unsaturated carbon atoms at the periphery are paired of with hydrogen atoms, see Fig. 6.18.

Note that the HOMO is two-fold degenerate. Therefore, a proper simulation of the photoemission pattern from such an initial state requires averaging over the degenerate manifold. Nevertheless, it is instructive to analyze the two states, HOMO-a and HOMO-b, individually. Fig. 6.19 shows the momentum maps for incident light polarized along the z-direction. In both cases the LS-simulation only deviates slightly from the PW-simulation.

Due to the degeneracy, what should be observed experimentally is the sum of the two orbital contributions. This is illustrated in Fig. 6.20. The symmetry of the molecule becomes only apparent in the momentum maps of the sum of the degenerate orbitals.

Fig. 6.21 shows simulated momentum maps with p-polarized light incident at an angle of 65° from the normal, which corresponds to the typical situation encountered in NanoESCA momentum microscopes. Again, the differences between the two approaches are only minor. The deviation between the two approaches seems to be more pronounced for higher $\boldsymbol{k}_{\parallel}$, or, equivalently, lower k_z. A handwaving argument can be put forward why this might be the case. Photoelectrons with smaller perpendicular wavevectors are more subject to the pull and push of the molecular potential as they have to pass closer to the molecule for longer periods of time. Incidentally, this is also true for flat molecules, but the effect seems stronger for nonplanar molecules.

Based on the results shown here, it seems worthwile to investigate the system experimentally. There are indeed plans for such a measurement campaign, but no

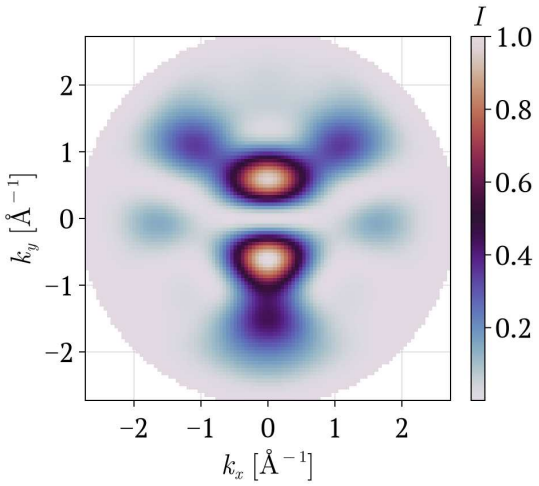

(a) Plane-wave approximation

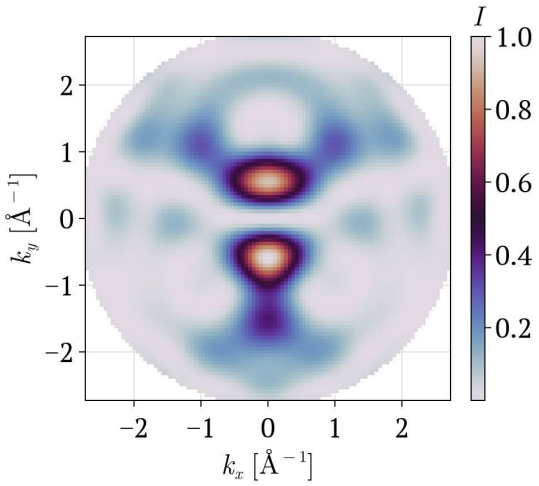

(b) Lippmann-Schwinger

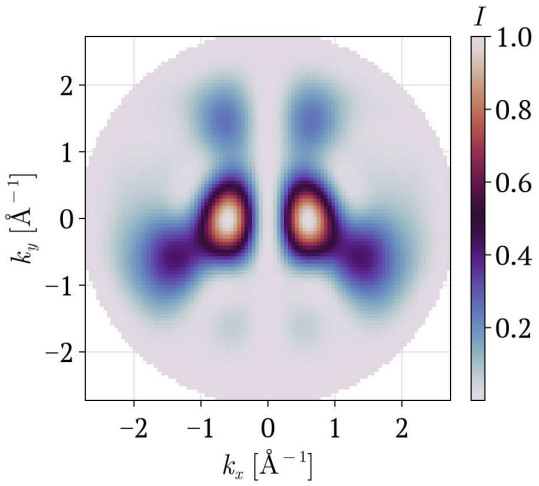

(c) Plane-wave approximation

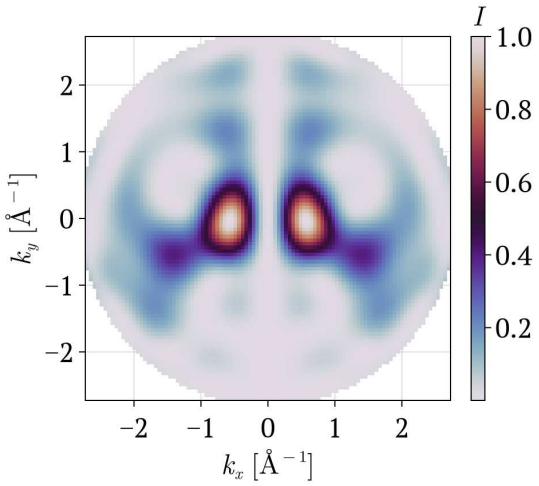

(d) Lippmann-Schwinger

Figure 6.19: Momentum maps of degenerate HOMO of corannulene. Top row, HOMO-a. Bottom row, HOMO-b. The polarization points in the z-direction. The kinetic energy of the photoelectrons is 30 eV.

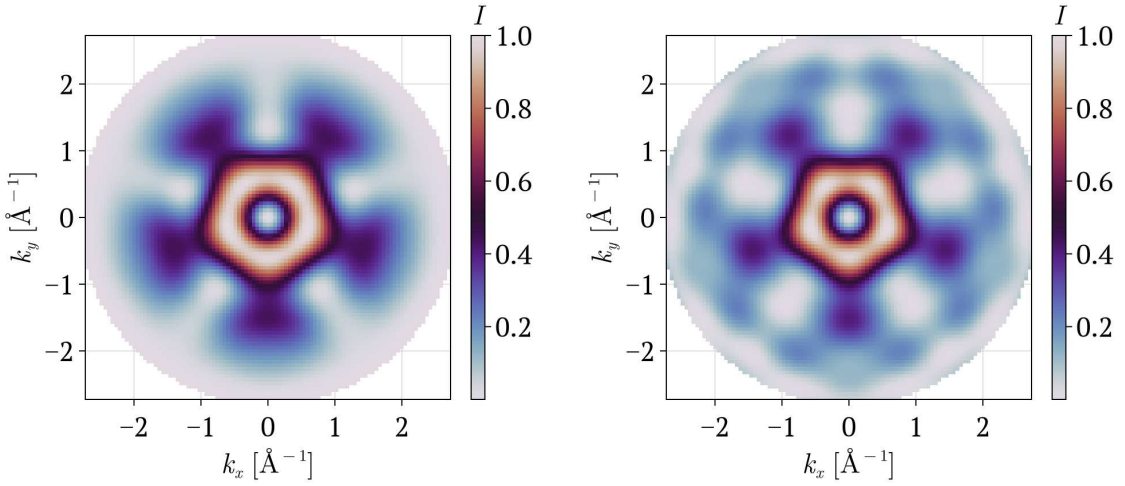

(a) Plane-wave approximation

(b) Lippmann-Schwinger

Figure 6.20: Momentum map of HOMO of corannulene. The polarization points in the z-direction. The kinetic energy of the photoelectrons is 30 eV.

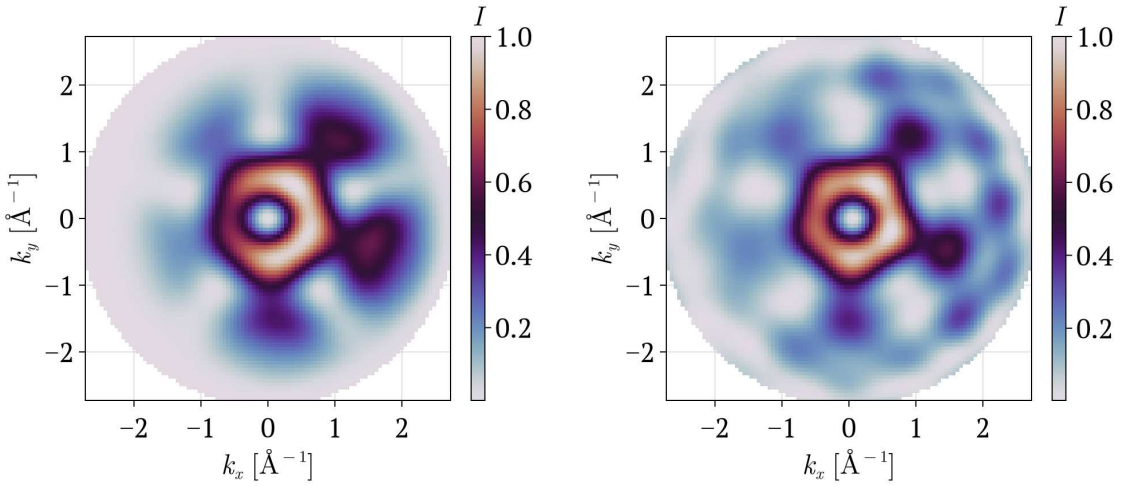

(a) Plane-wave approximation

(b) Lippmann-Schwinger

Figure 6.21: Momentum map of HOMO of corannulene. NanoESCA experimental configuration corresponding to p-polarized light incident in the xz-plane at an angle of 65° to the normal. The kinetic energy of the photoelectrons is 30 eV.

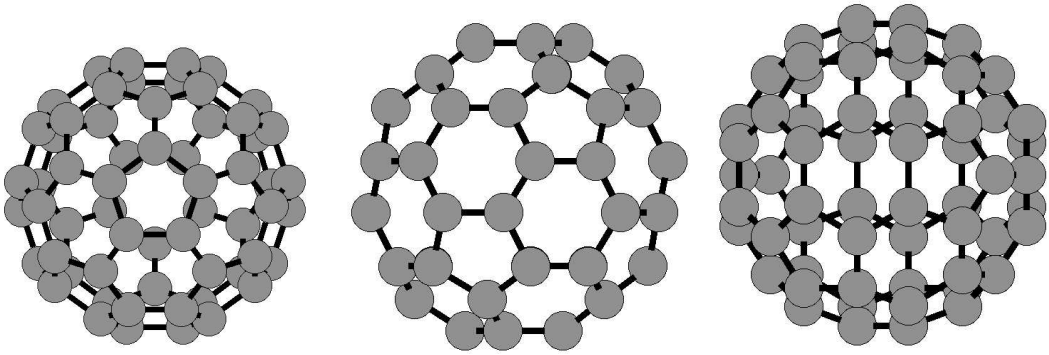

(a) xy-plane (b) yz-plane (c) zx-plane

Figure 6.22: Molecular structure of fullerene.

specific date has been set yet.

Fullerene

After investigating a building block of C_{60} in the previous chapter, we now turn to C_{60} proper. The photoemission spectra will depend sensitively on the actual adsorption geometry, where typically the energy difference between possible geometrical configurations are small, see [20] for numerical examples. For this thesis, we investigate the molecule in the "corannulene configuration", see Fig. 6.22, that is, with a pentagon facing the substrate.

For gas-phase C_{60}, the HOMO is five-fold degenerate. We therefore average the photoemission intensity over these five degenerate states, which is shown in Figs. 6.23-6.25. For all polarization configurations, the difference between the two approaches is striking. Focusing on Fig. 6.23, the central pentagon star in the PWA gets distored noticeably. In addition, the "ring" features around $k_{\|} \approx 2$ Å^{-1}acquire a much higher intensity.

Comparing the corannulene and C_{60} momentum maps in Figs. 6.20 and 6.23, it is clear that the central pentagon remains present but gets flipped. Also, the circular features alluded to above are more pronounced in the C_{60} momentum map.

In contrast to most flat molecules, the photon-energy dependence is directly visible in the momentum maps, see Fig. 6.26 for an example. Interestingly, in both the PWA and the LS solution the symmetry is not visible in the momentum maps at low kinetic energy, see Fig. 6.26a. In going from 30 to 45 eV in Figs. 6.26b and c the central pentagon splits into separate parts and the ring features around $k_{\|} \approx 2$ Å^{-1} vanish almost entirely.

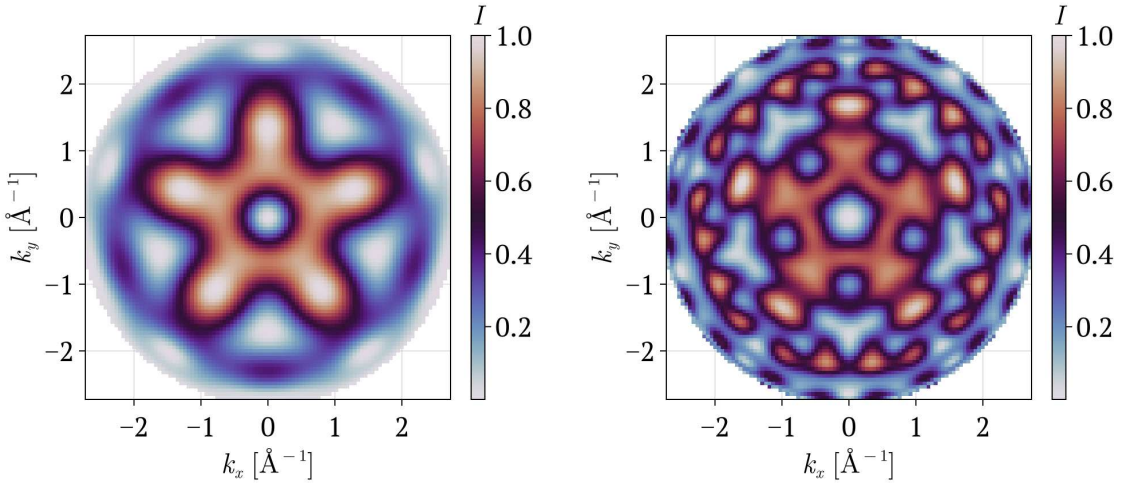

(a) Plane-wave approximation

(b) Lippmann-Schwinger

Figure 6.23: HOMO C_{60} momentum map. The polarization points in the z-direction. The kinetic energy of the photoelectrons is 30 eV.

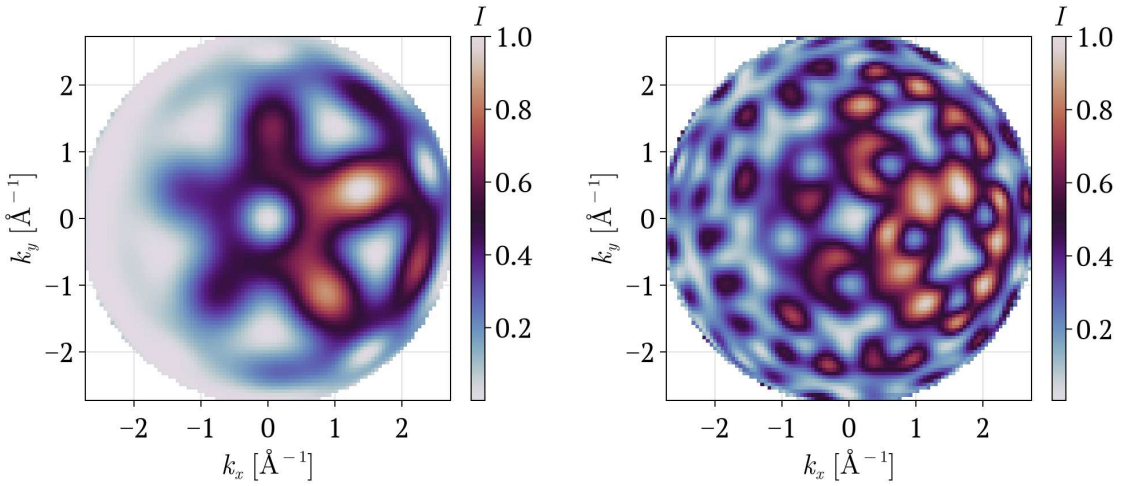

(a) Plane-wave approximation

(b) Lippmann-Schwinger

Figure 6.24: HOMO C_{60} momentum map. NanoESCA experimental configuration with p-polarized light incident in the xz-plane at an angle of 65°. The kinetic energy of the photoelectrons is 30 eV.

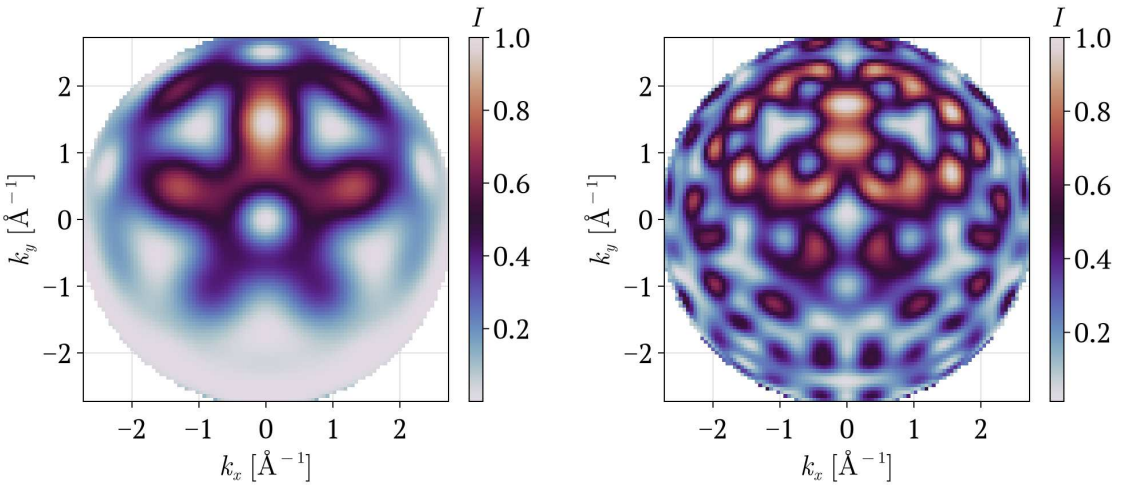

(a) Plane-wave approximation

(b) Lippmann-Schwinger

Figure 6.25: HOMO C_{60} momentum map. NanoESCA experimental configuration with p-polarized light incident in the yz-plane at an angle of 65°. The kinetic energy of the photoelectrons is 30 eV.

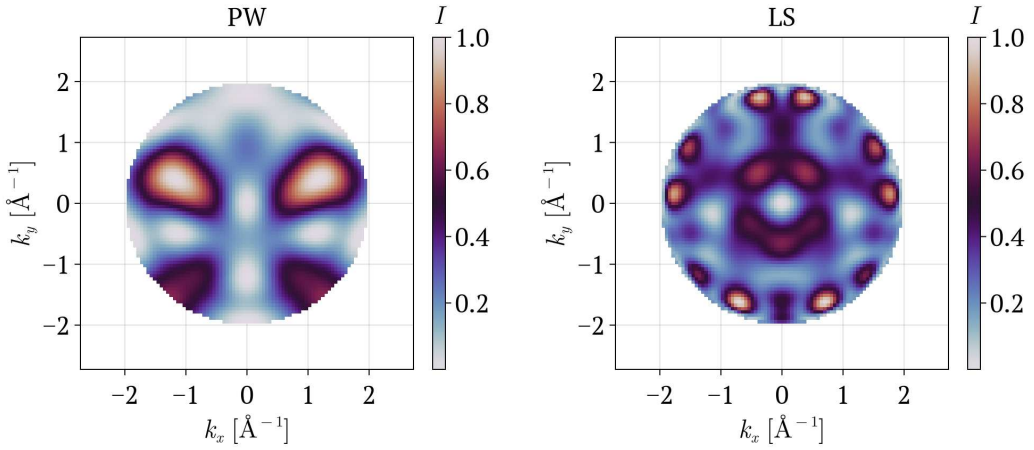

(a) Kinetic energy 15 eV.

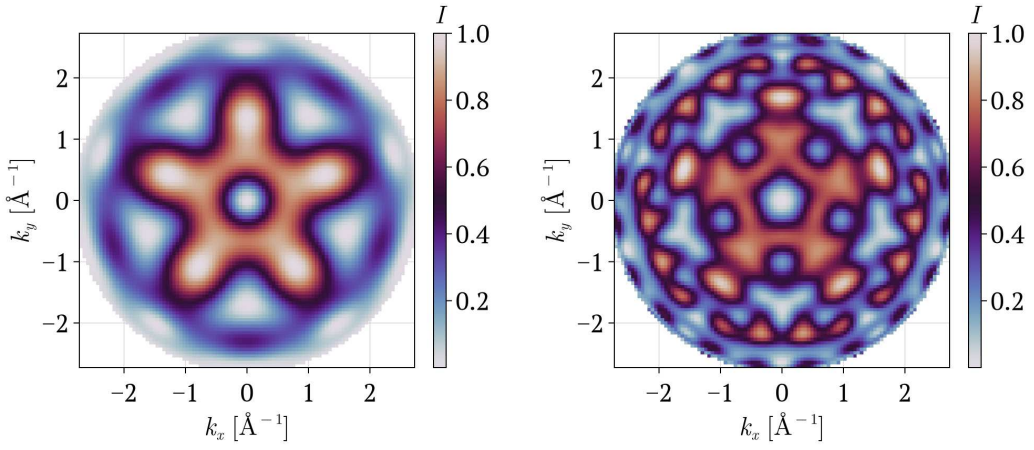

(b) Kinetic energy 30 eV.

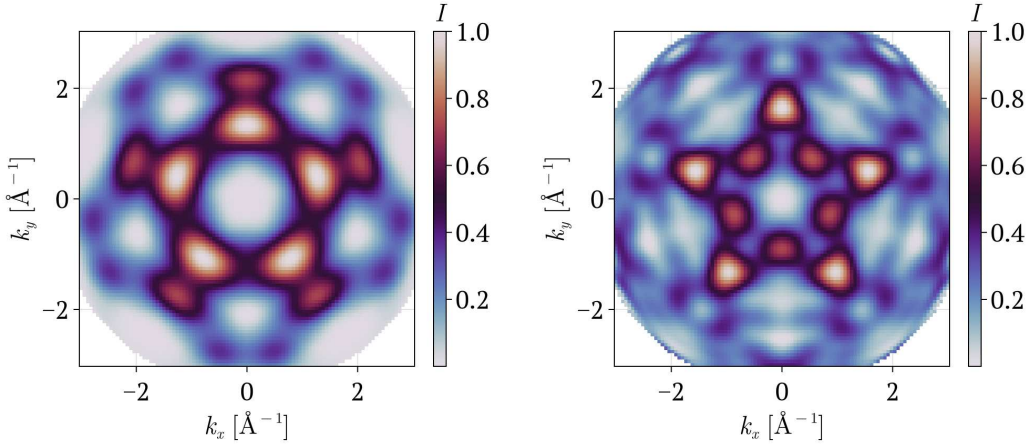

(c) Kinetic energy 45 eV.

Figure 6.26: HOMO C_{60} momentum map. The polarization points in the z-direction. The kinetic energy of the photoelectrons is indicated in the subfigure captions.

6.4 Lessons learned for standard photoemission orbital tomography

Momentum maps. As long as the experimental setup does not explicitly violate some obvious limitations of the PWA, such as the $\boldsymbol{A} \perp \boldsymbol{k}$ and circular dichroism failures, it seems to be remarkably robust, at least for planar or close to planar molecules. Most, though by no means all, experiments do not depend vitaly on the $\boldsymbol{A} \perp \boldsymbol{k}$ constraint, so this is less severe than the CDAD failure. The failure to account for the CDAD weighs more heavily. CDAD has been linked to the Berry curvature [89] and has been thoroughly investigated as a result, see e.g. [25, 90]. Therefore it is crucial to address this failure directly.

CIS-scans. The qualitative features of CIS-scans in the PWA seem to be remarkably independent of the initial state. In contrast, the dependence on the final state is quite pronounced. Unfortunately, while our approach reproduces some qualitative features of the spectrum in Fig.6.17, it still falls short of accounting for it quantitatively. The shape of CIS-scans is most likely strongly affected by the presence or absence of the nonlocal potential in the final state, which we unfortunately had to neglect, see Chapter 6.5. It remains to be seen whether other approaches, such as TDDFT, fare better in comparison.

6.5 The (disregarded) influence of the nonlocal potential

So far, for ease of implementation and to reduce the computational cost, we have neglected the nonlocal potential in the calculation of the photoelectron state Eq. (6.3). In the initial state calculation, the nonlocal potential is only applied to the wavefunction in the Schrödinger equation—that is, it is not stored directly [91]. Although it is straightforward in principle to include the nonlocal potential contribution into the LS-equation, in practice the deterioration of performance was too severe to do so. The LS-equation with only the local potential contribution reads

$$\phi_{\boldsymbol{k}}(\boldsymbol{r}') + \int d^3r' G_0^*(\boldsymbol{r}, \boldsymbol{r}') V(\boldsymbol{r}') \psi_{\boldsymbol{k}}(\boldsymbol{r}') = \psi_{\boldsymbol{k}}(\boldsymbol{r}), \tag{6.23}$$

while the total potential would also involve a nonlocal contribution, that is,

$$\phi_{\boldsymbol{k}}(\boldsymbol{r}') + \int d^3r' G_0^*(\boldsymbol{r}, \boldsymbol{r}') V(\boldsymbol{r}') \psi_{\boldsymbol{k}}(\boldsymbol{r}') + \int d^3r' d^3r_1 G_0^*(\boldsymbol{r}, \boldsymbol{r}_1) V_{\mathrm{nl}}(\boldsymbol{r}_1, \boldsymbol{r}') \psi_{\boldsymbol{k}}(\boldsymbol{r}') = \psi_{\boldsymbol{k}}(\boldsymbol{r}). \tag{6.24}$$

So far, we have neglected the third term in the above equation, i.e.,

$$\int d^3r' d^3r_1 G_0^*(\boldsymbol{r}, \boldsymbol{r}_1) V_{\mathrm{nl}}(\boldsymbol{r}_1, \boldsymbol{r}') \psi_{\boldsymbol{k}}(\boldsymbol{r}'). \tag{6.25}$$

Upon discretization, this term involves a matrix multiplication between the Green function and the nonlocal potential. The nonlocal potential is given in Kleinman-Bylander form, see Chapter 2.2. Explicitly, it is given by

$$V_{\mathrm{nl}}(\boldsymbol{r}_1, \boldsymbol{r}') = \sum_{lmn} E_{ln} \psi_{ln}(r_1) \psi_{ln}^*(r') Y_{lm}(\hat{\boldsymbol{r}}_1) Y_{lm}^*(\hat{\boldsymbol{r}}'), \tag{6.26}$$

with the projectors χ_{ln}. We use the shorthand

$$\psi_{ln}(r) = \frac{\chi_{ln}(r)}{r} \tag{6.27}$$

to lessen clutter. The matrix multiplication thus reduces to the multiplication by a projector, which is also centered around an atom and falls off quite rapidly.

In somewhat more detail, the radial expansion of the Green function can be used to carry out the angular integrals. The expansion was introduced in Chapter 2.3.2 and is repeated here for convenience with minor modifications in the indices:

$$G^*(\boldsymbol{r}, \boldsymbol{r}_1) = -\frac{e^{-ik|\boldsymbol{r}-\boldsymbol{r}_1|}}{4\pi|\boldsymbol{r}-\boldsymbol{r}_1|} = \sum_{lm} G_k^{*(l)}(r, r_1) Y_{lm}(\hat{\boldsymbol{r}}) Y_{lm}^*(\hat{\boldsymbol{r}}_1). \tag{6.28}$$

The matrix multiplication $P(\boldsymbol{r}, \boldsymbol{r}') = \int d^3r_1 G^*(\boldsymbol{r}, \boldsymbol{r}_1) V_{\mathrm{nl}}(\boldsymbol{r}_1, \boldsymbol{r}')$ then gives

$$P(\boldsymbol{r}, \boldsymbol{r}') = \sum_{lmn} E_{ln} \psi_{ln}^*(r') Y_{lm}(\hat{\boldsymbol{r}}) Y_{lm}^*(\hat{\boldsymbol{r}}') \int dr_1 r_1^2 G_k^{*(l)}(r, r_1) \psi_{ln}(r_1), \tag{6.29}$$

due to the orthonormality of the spherical harmonics. Introducing the abbreviation

$$\xi_{ln}(r) = \int dr_1 r_1^2 G_k^{*(l)}(r, r_1) \psi_{ln}(r_1), \tag{6.30}$$

leads to

$$P(\boldsymbol{r}, \boldsymbol{r}') = \sum_{lmn} E_{ln} \xi_{ln}(r) \psi_{ln}^*(r') Y_{lm}(\hat{\boldsymbol{r}}) Y_{lm}^*(\hat{\boldsymbol{r}}'). \tag{6.31}$$

This term has the same form as the nonlocal potential itself and can therefore be evaluated in the same manner. In contrast to $\psi_{ln}(r)$, $\xi_{ln}(r)$ is not, however, a strongly

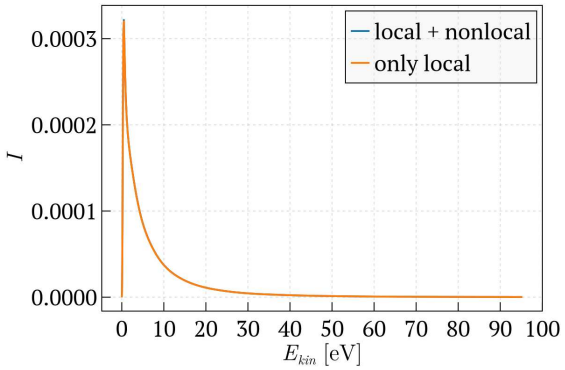

Figure 6.27: Intensity of the 1s-state of hydrogen as a function of the kinetic energy of the photoelectron. The polarization vector is in the z-direction. Note that the difference between the two curves is only directly visible at the maximum.

localized function around the atomic center. The numerical cost will be correspondingly higher.

The performance penalty in the construction of the LS H-matrix was unfortunately prohibitive. Therefore, this term had to be omitted.
In order to assess the error incurred by this omission, we turn to the radial method of Chapter 5. First, the binding energies deviate significantly, as Table 6.1 demonstrates. With the exception of hydrogen, all orbital energies are wildly off. Next we

Table 6.1: Binding energies of atomic orbitals in eV calculated with (E_{DFT}) and without the nonlocal potential (E_{local}).

	E_{DFT}	E_{local}
H 1s	6.47	5.79
C 2s	13.51	32.99
O 2s	24.64	51.62
Ar 3s	24.07	49.54

investigate the influence of the nonlocal potential on CIS-scans. In the case of hydrogen it practically makes no difference whether the nonlocal potential is included or not, as can be seen from Fig. 6.27. This is not true in general, however, as the CIS-scan of the argon 3s-orbital in Fig. 6.28 makes clear. We can conclude from this that on physical grounds there is no justification for omiting the nonlocal potential. Whether the results of the thus distorted LS-equation are still usefull will have to be decided on a case-by-case basis.

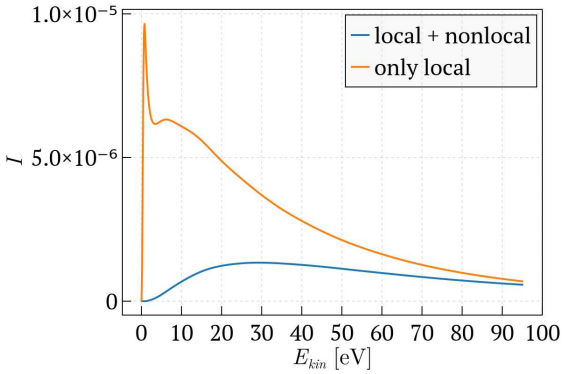

Figure 6.28: Intensity of the 3s-state of argon as a function of the kinetic energy of the photoelectron. The polarization vector is in the z-direction.

Let us find out whether the situation with regards to the omission of the nonlocal potential for molecules is as bleak as for atoms. A glance at Table 6.2 reveals that the differences are not as stark as with atoms.

Table 6.2: Binding energies of the HOMO in eV calculated with (E_{DFT} and without the nonlocal potential (E_{local}).

	E_{DFT}	E_{local}
Benzene	6.05	5.02
Tetracene	4.11	4.46
Bisanthene	3.57	4.23
PTCDA	5.37	3.72

6.5.1 Neglecting the nonlocal potential also in the initial state

In the absence of a complete final state calculation, let us investigate the consequences of the omission of the nonlocal contribution in the initial state calculation on photoemission spectra of molecules. The hope is that the effect of the nonlocal potential is minor, at least for momentum maps. In turn, this would imply that omitting it in the final state will not cause severe problems.

Unfortunately, Fig. 6.29 makes it clear that it is essential to include the nonlocal potential at least in the initial state. The momentum maps that result from omitting the nonlocal potential from both the initial and final state are simply wrong, see

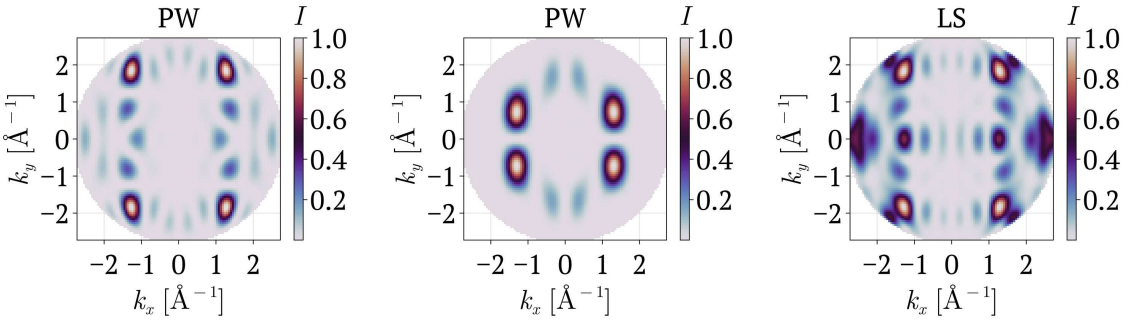

(a) Local (b) Total (c) Local

Figure 6.29: PTCDA momentum maps. The polarization points in the z-direction. The kinetic energy of the photoelectrons is 30 eV. The nonlocal potential contribution in the initial state is specified in the subfigure captions.

Fig. 6.29a for the PWA and Fig. 6.29c for the LS-approach. It should be noted that Fig. 6.29b depicts the PWA of the initial state with the total potential, and that the PWA is appropriate for this polarization configuration.

The takeaway from this section is that it is necessary to include the nonlocal potential into the initial state calculation and that leaving it out in the final state is fraught with uncertainties.

On a more positive note, the shape of momentum maps, which after all serve as the main signature of ARPES experiments, seems less affected by the omission of the nonlocal potential in the final state calculation. This can be seen from the rather close agreemenet between the TDDFT and LS maps in Figs. 6.9 and 6.10 for example. To what extent the remaining difference is due to the omission of the nonlocal potential in the final state is unclear.

The question of how to incorporate the nonlocal potential into the final state is still open. There is probably a clever way to include it into the LS H-matrix, but, alas, so far our attempts have failed. And finally, while the Born series is a hopeless endeavor for the total potential, it might be worthwile to try it for the nonlocal potential separately, i.e. to first solve the LS-equation without the nonlocal contribution, and then, in a second step, to apply it perturbatively.

6.6 Postscript: Including the nonlocal potential after all.

Ultimately, the only way to ascertain whether it is justified to leave out the nonlocal potential is to compare results from simulations with and without nonlocal contributions in the final state. Here we intend to demonstrate the effect of the nonlocal potential in the final state[5] on the CDAD maps of tetracene, since the deviations from the TDDFT simulations in Fig. 6.13 are particularly strong. We use the shortcut in Eq. (6.31) to evaluate the nonlocal contribution and reduce the numerical cost. The results are shown in Fig. 6.30. Regardless of whether or not the nonlocal potential is included, the maps are almost indistinguishable. The positive takeaway is that momentum maps seem to be rather insensitive to the presence of the nonlocal potential in the final state.

To validate the calculation, the overlap $\langle\psi_f|\psi_{\text{in}}\rangle$ for three different final states is shown in Fig. 6.31. The overlap of both the local and total potential calculations are smaller than the plane wave overlap. Unfortunately, the difference between the two LS approaches is rather miniscule. This might be due to a too small energy cutoff—even though 20 Hartree are used instead of the standard 15 Hartree in the rest of the chapter—or the implementation is still flawed.

In principle, CIS-scans can be calculated in the same manner, but due to time constraints we unfortunately could not do the calculations yet.

[5] The nonlocal potential is obviously already included in the initial state.

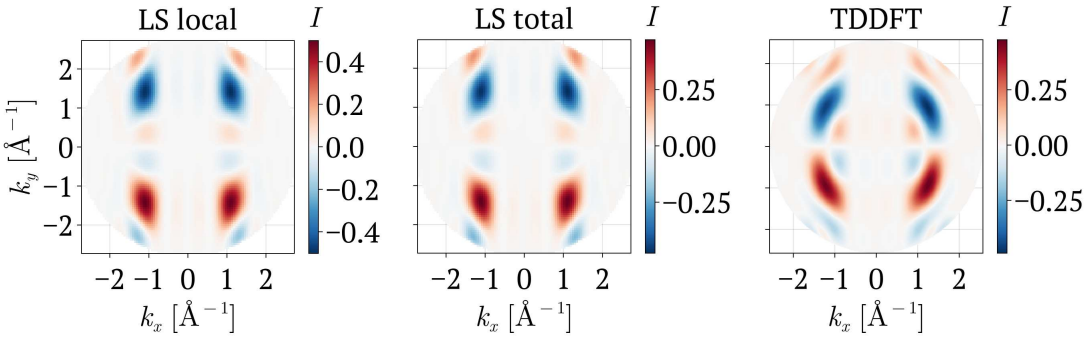

(a) $\boldsymbol{A} \propto (0, \mp i, 1)$

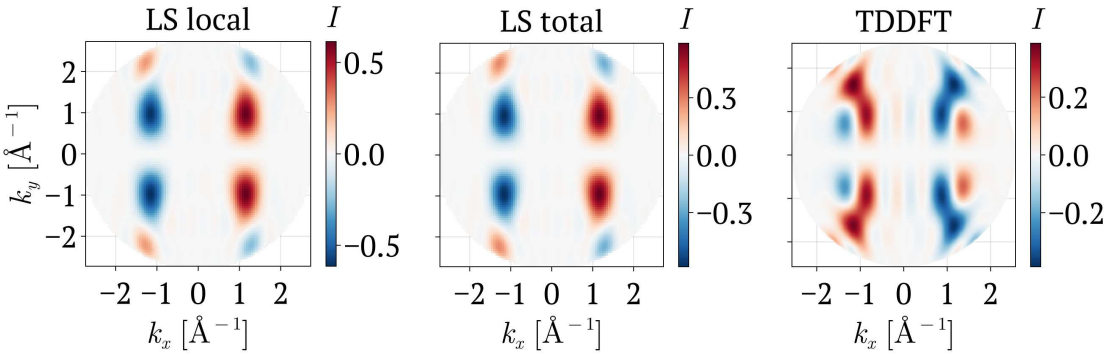

(b) $\boldsymbol{A} \propto (\pm i, 0, 1)$

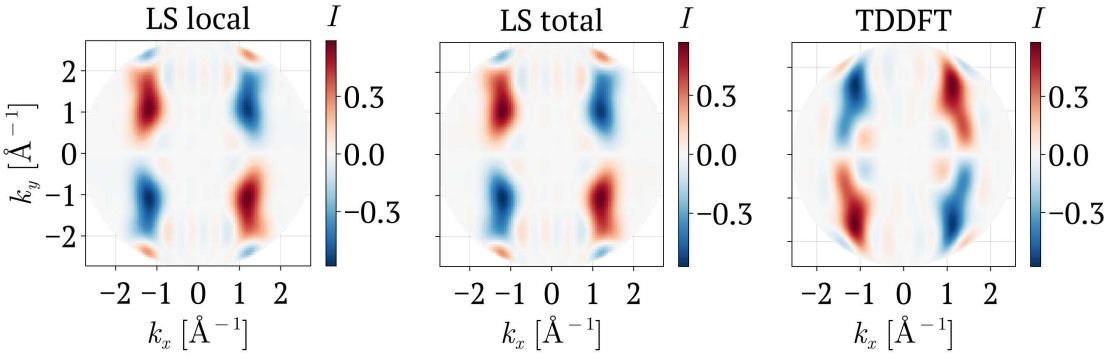

(c) $\boldsymbol{A} \propto (1, \pm i, 0)$

Figure 6.30: Same as Fig. 6.13, but the LS solution contains both the local and nonlocal contributions, while the "LS local" map only contains the local one.

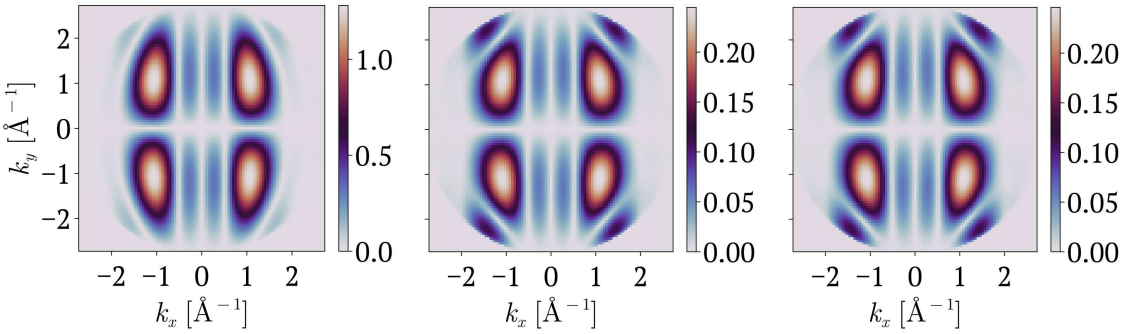

(a) Plane wave (b) Local (c) Total

Figure 6.31: Absolute value of the overlap $\langle\psi_f|\psi_{\text{in}}\rangle$ for the indicated final states. The initial state in each case is taken from the tetracene DFT calculation. Note the different scales.

Chapter 7

Conclusion

This thesis dealt with the question of how to incorporate scattering effects into the description of the photoelectron final state to avoid the major flaws of the plane-wave approximation, while still remaining computationally tractable. The aim was to implement a method that is as reliable as, or at least competitive with, and ideally faster than, the simulation approach based on time-dependent density functional theory [82, 85].

All methods developed in this thesis are based on the solution of the Lippmann-Schwinger equation, which incorporates the elastic scattering processes that the photoelectron experiences in the sample prior to being detected. Both in the plane-wave approximation and the Lippmann-Schwinger method, the required initial state properties—the binding energy and the wavefunction of the desired Kohn-Sham orbital, and the Kohn-Sham potential—stem from a (ground-state) density functional theory calculation. Depending on the simulated physical system, the Lippmann-Schwinger equation can be formulated in either reciprocal space for extended systems or in real space for isolated gas-phase molecules.

The computation of photoemission spectra is an active area of research. In the course of this thesis, at least one method that is very similar to our momentum space methods has appeared in print [18]. This publication largely supersedes our failed attempts presented in Chapter 3. Nevertheless, it might be possible to salvage something from the developed method that uses the eigenfunction expansion of the Green function; in particular, the all-ellectron description that is in principle attainable with this method might be employed successfully.

The real space method that we developed and presented in Chapter 6 is much more promising. As we have seen, it is not afflicted by the most obvious shortcomings of the plane-wave approximation. Specifically, in contrast to the plane-wave approx-

imation for the photoelectron state, it can account for a nonvanishing photoemission intensity perpendicular to the polarization direction and circular dichroism. It also alleviates some quantitative shortcomings of the plane-wave approximation, among them the photon-energy dependence of the photoemission intensity and the simulation of non-planar molecules in general. The main advantage of the real space method to time-dependent density functional theory—probably its main competitor—is its comparatively lower computational cost. Another advantage is the relative ease with which unoccupied orbitals can be treated within the real space approach, something that is not straightforward in time-dependent DFT. In addition, within the real space method, it is easy to switch between different functionals, while time-dependent DFT is limited to the local density approximation.

As a rule of thumb, the calculation of one momentum map takes about one day on a node with 64 cores, but this includes all desired polarization configurations, also when the nonlocal potential is included. Neglecting the nonlocal potential, a constant-initial state scan again takes roughly one day. Including the nonlocal potential in this case, however, results in a noticeably higher, but not prohibitive, simulation time—roughly one week for 100 photon energies on the same hardware. But since the calculations for the different photon energies are independent of each other, it would be trivial to run the code in parallel on more nodes.

Unfortunately, we had to leave some avenues unexplored. In particular, it would be interesting to test hybrid functionals and to include all-electron effects with the projector augmented wave formalism. From a numerical perspective, due to the oscillating Kernel in the Lippmann-Schwinger equation, the use of H^2-matrices instead of H-matrices could boost the performance, as could the inclusion of the point group symmetry of the molecules.

Whether this new method will be useful in the future remains to be seen.

Bibliography

[1] A. Einstein. Über einen die erzeugung und verwandlung des lichtes betreffenden heuristischen gesichtspunkt. *Annalen der Physik*, 322(6):132–148, 1905.

[2] R. Shankar. *Principles of Quantum Mechanics*. Physics and Astronomy. Springer US, 2012.

[3] J. W. Gadzuk. Surface molecules and chemisorption. ii. photoemission angular distributions. *Phys. Rev. B*, 10:5030–5044, 1974.

[4] H.A. Bethe and E.E. Salpeter. *Quantum Mechanics of One- and Two-electron Atoms*. Springer, 1957.

[5] Warren D. Grobman. Angle-resolved photoemission from molecules in the independent-atomic-center approximation. *Phys. Rev. B*, 17:4573, 1978.

[6] Andrea Damascelli, Zahid Hussain, and Zhi-Xun Shen. Angle-resolved photoemission studies of the cuprate superconductors. *Rev. Mod. Phys.*, 75:473–541, 2003.

[7] Jonathan A. Sobota, Yu He, and Zhi-Xun Shen. Angle-resolved photoemission studies of quantum materials. *Rev. Mod. Phys.*, 93:025006, 2021.

[8] Peter Puschnig, Stephen Berkebile, Alexander J. Fleming, Georg Koller, Konstantin Emtsev, Thomas Seyller, John D. Riley, Claudia Ambrosch-Draxl, Falko P. Netzer, and Michael G. Ramsey. Reconstruction of molecular orbital densities from photoemission data. *Science*, 326(5953):702–706, 2009.

[9] Peter Puschnig and Daniel Lüftner. Simulation of angle-resolved photoemission spectra by approximating the final state by a plane wave: from graphene to polycyclic aromatic hydrocarbon molecules. *J. Elec. Spec. Rel. Phen.*, 200:193–208, 2015.

[10] Philipp Hurdax, Michael Hollerer, Christian S. Kern, Peter Puschnig, Martin Sterrer, and Michael G. Ramsey. Integer charge transfer model–ptcda on mgo(001)/ag(001) probing the transition from single to double integer charge transfer. *The Journal of Physical Chemistry C*, 129(2):1553–1561, 2025.

[11] Dominik Brandstetter, Simone Mearini, Andreas Windischbacher, Yan yan Grisan Qiu, Daniel Baranowski, Vitaliy Feyer, Claus Michael Schneider, and Peter Puschnig. Revealing the character of coordination bonding in 2d metal-organic frameworks. *Advanced Science*, xxx, 2025.

[12] C. S. Kern, A. Windischbacher, and P. Puschnig. Photoemission orbital tomography for excitons in organic molecules. *Phys. Rev. B*, 108:085132, Aug 2023.

[13] A M Bradshaw and D P Woodruff. Molecular orbital tomography for adsorbed molecules: is a correct description of the final state really unimportant? *New Journal of Physics*, 17(1):013033, 2015.

[14] Philipp Wopperer, Umberto De Giovannini, and Angel Rubio. Efficient and accurate modeling of electron photoemission in nanostructures with TDDFT. *European Physical Journal B*, 90(3):51, 2017.

[15] U. De Giovannini, D. Varsano, M. A. L. Marques, H. Appel, E. K. U. Gross, and A. Rubio. Ab initio angle- and energy-resolved photoelectron spectroscopy with time-dependent density-functional theory. *Phys. Rev. A*, 85:062515, 2012.

[16] Fabio Boschini, Marta Zonno, and Andrea Damascelli. Time-resolved arpes studies of quantum materials. *Rev. Mod. Phys.*, 96:015003, 2024.

[17] H. Fukagawa, H. Yamane, T. Kataoka, S. Kera, M. Nakamura, K. Kudo, and N. Ueno. Origin of the highest occupied band position in pentacene films from ultraviolet photoelectron spectroscopy: Hole stabilization versus band dispersion. *Phys. Rev. B*, 73:245310, 2006.

[18] Ji Hoon Ryoo and Cheol-Hwan Park. Lippmann-schwinger approach for accurate photoelectron wave functions and angle-resolved photoemission spectra from first principles. *Phys. Rev. Lett.*, 135:056403, 2025.

[19] M. Dauth, M. Graus, I. Schelter, M. Wießner, A. Schöll, F. Reinert, and S. Kümmel. Perpendicular emission, dichroism, and energy dependence in angle-resolved photoemission: The importance of the final state. *Phys. Rev. Lett.*, 117:183001, 2016.

[20] C. Metzger, M. Graus, M. Grimm, G. Zamborlini, V. Feyer, M. Schwendt, D. Lüftner, P. Puschnig, A. Schöll, and F. Reinert. Plane-wave final state for photoemission from nonplanar molecules at a metal-organic interface. *Phys. Rev. B*, 101:165421, 2020.

[21] Giovanni Di Santo, Tanja Miletić, Mathias Schwendt, Yating Zhou, Benson M. Kariuki, Kenneth D. M. Harris, Luca Floreano, Andrea Goldoni, Peter Puschnig, Luca Petaccia, and Davide Bonifazi. Orbital mapping of semiconducting perylenes on cu(111). *The Journal of Physical Chemistry C*, 125(44):24477–24486, 2021.

[22] A. H. Castro Neto, F. Guinea, N. M. R. Peres, K. S. Novoselov, and A. K. Geim. The electronic properties of graphene. *Rev. Mod. Phys.*, 81:109–162, 2009.

[23] Sajedeh Manzeli, Dmitry Ovchinnikov, Diego Pasquier, Oleg V. Yazyev, and Andras Kis. 2D transition metal dichalcogenides. *Nature Reviews Materials*, 2(8):17033, 2017.

[24] Taisuke Ohta, Aaron Bostwick, J. L. McChesney, Thomas Seyller, Karsten Horn, and Eli Rotenberg. Interlayer interaction and electronic screening in multilayer graphene investigated with angle-resolved photoemission spectroscopy. *Phys. Rev. Lett.*, 98:206802, 2007.

[25] Honey Boban, Mohammed Qahosh, Xiao Hou, Tomasz Sobol, Edyta Beyer, Magdalena Szczepanik, Daniel Baranowski, Simone Mearini, Vitaliy Feyer, Yuriy Mokrousov, Yishui Zhou, Yixi Su, Keda Jin, Tobias Wichmann, Jose Martinez-Castro, Markus Ternes, F. Stefan Tautz, Felix Lüpke, Claus M. Schneider, Jürgen Henk, and Lukasz Plucinski. Scattering makes a difference in circular dichroic angle-resolved photoemission. *Phys. Rev. B*, 111:115127, 2025.

[26] Peter Puschnig and Michael G. Ramsey. Photoemission tomography: Valence band photoemission as a quantitative method for investigating molecular films. 2018.

[27] Richard M. Martin. *Electronic Structure: Basic Theory and Practical Methods*. Cambridge University Press, 2 edition, 2020.

[28] C. Fiolhais, F. Nogueira, and M.A.L. Marques. *A Primer in Density Functional Theory*. Lecture Notes in Physics. Springer Berlin Heidelberg, 2008.

[29] P. Hohenberg and W. Kohn. Inhomogeneous electron gas. *Phys. Rev.*, 136:B864–B871, 1964.

[30] W. Kohn and L. J. Sham. Self-consistent equations including exchange and correlation effects. *Phys. Rev.*, 140:A1133–A1138, 1965.

[31] John P. Perdew, Kieron Burke, and Matthias Ernzerhof. Generalized gradient approximation made simple. *Phys. Rev. Lett.*, 77:3865–3868, 1996.

[32] R. O. Jones. Density functional theory: Its origins, rise to prominence, and future. *Rev. Mod. Phys.*, 87:897–923, 2015.

[33] M.J. van Setten, M. Giantomassi, E. Bousquet, M.J. Verstraete, D.R. Hamann, X. Gonze, and G.-M. Rignanese. The pseudodojo: Training and grading a 85 element optimized norm-conserving pseudopotential table. *Computer Physics Communications*, 226:39–54, 2018.

[34] David Vanderbilt. Soft self-consistent pseudopotentials in a generalized eigenvalue formalism. *Phys. Rev. B*, 41:7892–7895, 1990.

[35] P. E. Blöchl. Projector augmented-wave method. *Phys. Rev. B*, 50:17953–17979, 1994.

[36] Leonard Kleinman and D. M. Bylander. Efficacious form for model pseudopotentials. *Phys. Rev. Lett.*, 48:1425–1428, 1982.

[37] D. R. Hamann, M. Schlüter, and C. Chiang. Norm-conserving pseudopotentials. *Phys. Rev. Lett.*, 43:1494–1497, 1979.

[38] Tung-Mow Yan Kurt Gottfried. *Quantum Mechanics: Fundamentals*. Graduate Texts in Contemporary Physics. Springer New York, NY, 2004.

[39] Economou E. N. *Green's Functions in Quantum Physics*. Springer Berlin, Heidelberg, 2006.

[40] J.E. Inglesfield and E.W. Plummer. Chapter 2 the physics of photoemission. In S.D. Kevan, editor, *Angle-Resolved Photoemission*, volume 74 of *Studies in Surface Science and Catalysis*, pages 15–61. Elsevier, 1992.

[41] T. Miller, W. E. McMahon, and T.-C. Chiang. Interference between bulk and surface photoemission transitions in ag(111). *Phys. Rev. Lett.*, 77:1167–1170, 1996.

[42] J. D. Koralek, J. F. Douglas, N. C. Plumb, Z. Sun, A. V. Fedorov, M. M. Murnane, H. C. Kapteyn, S. T. Cundiff, Y. Aiura, K. Oka, H. Eisaki, and D. S. Dessau. Laser based angle-resolved photoemission, the sudden approximation, and quasiparticle-like spectral peaks in $bi_2sr_2cacu_2o_{8+\delta}$. *Phys. Rev. Lett.*, 96:017005, 2006.

[43] M Dauth, M Wiessner, V Feyer, A Schöll, P Puschnig, F Reinert, and S Kümmel. Angle resolved photoemission from organic semiconductors: orbital imaging beyond the molecular orbital interpretation. *New Journal of Physics*, 16(10):103005, 2014.

[44] M.C. Desjonqueres and D. Spanjaard. *Concepts in Surface Physics*. Springer Berlin Heidelberg, 2012.

[45] B H Bransden and C J Joachain. *Physics of Atoms and Molecules*. Prentice-Hall, Harlow, 2003.

[46] Hans J. Weber George B. Arfken and Frank E. Harris. *Mathematical Methods for Physicists: A Comprehensive Guide*. Academic Press;, 2012.

[47] Michael Schüler. private communication.

[48] Thomas Fauster, Lutz Hammer, Klaus Heinz, and M. Alexander Schneider. *Oberflächenphysik*. De Gruyter Oldenbourg, Berlin, Boston, 2019.

[49] Steven M. Girvin and Kun Yang. *Modern Condensed Matter Physics*. Cambridge University Press, 2019.

[50] Misa Nozaki and Peter Krüger. Computational method for angle-resolved photoemission spectra from repeated-slab band structure calculations. *Phys. Rev. B*, 110:195406, 2024.

[51] Lew D. Landau Jewgeni M. Lifschitz. *Quantenmechanik*. Lehrbücher der theoretischen Physik. Europa-Lehrmittel, 1986.

[52] John W. Cooper. Photoionization from outer atomic subshells. a model study. *Phys. Rev.*, 128:681–693, 1962.

[53] Ansgar Liebsch. Theory of photoemission from localized adsorbate levels. *Phys. Rev. B*, 13:544–555, 1976.

[54] S Baral, J Jose, P C Deshmukh, and S T Manson. Cooper minima in high-z atoms: effects of correlation and relativity on np photoionization. *Journal of Physics B: Atomic, Molecular and Optical Physics*, 57(13):135001, 2024.

[55] Hans Kirschner, Alexander Gottwald, Victor Soltwisch, Mathias Richter, Peter Puschnig, and Simon Moser. Quantitative reconstruction of atomic orbital densities of neon from partial cross sections. *Phys. Rev. A*, 109:012814, 2024.

[56] M.Y. Amusia. *Atomic Photoeffect*. Physics of Atoms and Molecules. Springer US, 1990.

[57] Michael F. Herbst, Antoine Levitt, and Eric Cancès. DFTK: A Julian approach for simulating electrons in solids. *Proc. JuliaCon Conf.*, 3:69, 2021.

[58] B. Möbus, B. Magel, K.-H. Schartner, B. Langer, U. Becker, M. Wildberger, and H. Schmoranzer. Measurements of absolute ar 3s photoionization cross sections. *Phys. Rev. A*, 47:3888–3893, 1993.

[59] C. Alexandridi, D. Platzer, L. Barreau, D. Busto, S. Zhong, M. Turconi, L. Neoričić, H. Laurell, C. L. Arnold, A. Borot, J.-F. Hergott, O. Tcherbakoff, M. Lejman, M. Gisselbrecht, E. Lindroth, A. L'Huillier, J. M. Dahlström, and P. Salières. Attosecond photoionization dynamics in the vicinity of the cooper minima in argon. *Phys. Rev. Res.*, 3:L012012, 2021.

[60] M.Ya. Amusia, V.K. Ivanov, N.A. Cherepkov, and L.V. Chernysheva. Interference effects in photoionization of noble gas atoms outer s-subshells. *Physics Letters A*, 40(5):361–362, 1972.

[61] Harvey Hall. The theory of photoelectric absorption for x-rays and γ-rays. *Rev. Mod. Phys.*, 8:358–397, 1936.

[62] John M. Harriman. Numerical values for hydrogen fine structure. *Phys. Rev.*, 101:594–598, 1956.

[63] Jens Jørgen Mortensen, Ask Hjorth Larsen, Mikael Kuisma, Aleksei V. Ivanov, Alireza Taghizadeh, Andrew Peterson, Anubhab Haldar, Asmus Ougaard Dohn, Christian Schäfer, Elvar Örn Jónsson, Eric D. Hermes, Fredrik Andreas Nilsson, Georg Kastlunger, Gianluca Levi, Hannes Jónsson, Hannu Häkkinen, Jakub Fojt, Jiban Kangsabanik, Joachim Sødequist, Jouko Lehtomäki, Julian Heske, Jussi Enkovaara, Kirsten Trøstrup Winther, Marcin Dulak, Marko M. Melander, Martin Ovesen, Martti Louhivuori, Michael Walter, Morten Gjerding, Olga Lopez-Acevedo, Paul Erhart, Robert Warmbier, Rolf Würdemann,

Sami Kaappa, Simone Latini, Tara Maria Boland, Thomas Bligaard, Thorbjørn Skovhus, Toma Susi, Tristan Maxson, Tuomas Rossi, Xi Chen, Yorick Leonard A. Schmerwitz, Jakob Schiøtz, Thomas Olsen, Karsten Wedel Jacobsen, and Kristian Sommer Thygesen. Gpaw: An open python package for electronic structure calculations. *The Journal of Chemical Physics*, 160(9):092503, 2024.

[64] J. P. Perdew and Alex Zunger. Self-interaction correction to density-functional approximations for many-electron systems. *Phys. Rev. B*, 23:5048–5079, 1981.

[65] E. Aprà, E. J. Bylaska, W. A. de Jong, N. Govind, K. Kowalski, T. P. Straatsma, M. Valiev, H. J. J. van Dam, Y. Alexeev, J. Anchell, V. Anisimov, F. W. Aquino, R. Atta-Fynn, J. Autschbach, N. P. Bauman, J. C. Becca, D. E. Bernholdt, K. Bhaskaran-Nair, S. Bogatko, P. Borowski, J. Boschen, J. Brabec, A. Bruner, E. Cauët, Y. Chen, G. N. Chuev, C. J. Cramer, J. Daily, M. J. O. Deegan, T. H. Dunning, M. Dupuis, K. G. Dyall, G. I. Fann, S. A. Fischer, A. Fonari, H. Früchtl, L. Gagliardi, J. Garza, N. Gawande, S. Ghosh, K. Glaesemann, A. W. Götz, J. Hammond, V. Helms, E. D. Hermes, K. Hirao, S. Hirata, M. Jacquelin, L. Jensen, B. G. Johnson, H. Jónsson, R. A. Kendall, M. Klemm, R. Kobayashi, V. Konkov, S. Krishnamoorthy, M. Krishnan, Z. Lin, R. D. Lins, R. J. Littlefield, A. J. Logsdail, K. Lopata, W. Ma, A. V. Marenich, J. Martin del Campo, D. Mejia-Rodriguez, J. E. Moore, J. M. Mullin, T. Nakajima, D. R. Nascimento, J. A. Nichols, P. J. Nichols, J. Nieplocha, A. Otero-de-la Roza, B. Palmer, A. Panyala, T. Pirojsirikul, B. Peng, R. Peverati, J. Pittner, L. Pollack, R. M. Richard, P. Sadayappan, G. C. Schatz, W. A. Shelton, D. W. Silverstein, D. M. A. Smith, T. A. Soares, D. Song, M. Swart, H. L. Taylor, G. S. Thomas, V. Tipparaju, D. G. Truhlar, K. Tsemekhman, T. Van Voorhis, Á. Vázquez-Mayagoitia, P. Verma, O. Villa, A. Vishnu, K. D. Vogiatzis, D. Wang, J. H. Weare, M. J. Williamson, T. L. Windus, K. Woliński, A. T. Wong, Q. Wu, C. Yang, Q. Yu, M. Zacharias, Z. Zhang, Y. Zhao, and R. J. Harrison. Nwchem: Past, present, and future. *The Journal of Chemical Physics*, 152(18):184102, 2020.

[66] Takeshi Yanai, David P Tew, and Nicholas C Handy. A new hybrid exchange–correlation functional using the coulomb-attenuating method (cam-b3lyp). *Chemical Physics Letters*, 393(1):51–57, 2004.

[67] W.H. Press, S.A. Teukolsky, W.T. Vetterling, and B.P. Flannery. *Numerical Recipes: The Art of Scientific Computing*. Cambridge University Press, 3 edition, 2007.

[68] Jeff Bezanson, Alan Edelman, Stefan Karpinski, and Viral B Shah. Julia: A fresh approach to numerical computing. *SIAM Review*, 59(1):65–98, 2017.

[69] M.J. van Setten, M. Giantomassi, E. Bousquet, M.J. Verstraete, D.R. Hamann, X. Gonze, and G.-M. Rignanese. The pseudodojo: Training and grading a 85 element optimized norm-conserving pseudopotential table. *Computer Physics Communications*, 226:39–54, 2018.

[70] Sciml package.

[71] Wolfgang Hackbusch. Survey on the technique of hierarchical matrices. *Vietnam Journal of Mathematics*, 44(1):71–101, Mar 2016.

[72] Integral equation tutorials.

[73] M. Fenn and G. Steidl. *FMM and H-matrices: A Short Introduction to the Basic Idea*. Technical Reports. Universitätsbibliothek Mannheim, 2002.

[74] S. Börm. *Efficient Numerical Methods for Non-local Operators: H2-matrix Compression, Algorithms and Analysis*. EMS tracts in mathematics. European Mathematical Society, 2010.

[75] Stéphanie Chaillat, Luca Desiderio, and Patrick Ciarlet. Theory and implementation of h-matrix based iterative and direct solvers for helmholtz and elastodynamic oscillatory kernels. *Journal of Computational Physics*, 351:165–186, 2017.

[76] H-matrices package.

[77] Krylov solver package.

[78] M. Wießner, D. Hauschild, A. Schöll, F. Reinert, V. Feyer, K. Winkler, and B. Krömker. Electronic and geometric structure of the ptcda/ag(110) interface probed by angle-resolved photoemission. *Phys. Rev. B*, 86:045417, 2012.

[79] M. Willenbockel, D. Lüftner, B. Stadtmüller, G. Koller, C. Kumpf, S. Soubatch, P. Puschnig, M. G. Ramsey, and F. S. Tautz. The interplay between interface structure, energy level alignment and chemical bonding strength at organic–metal interfaces. *Phys. Chem. Chem. Phys.*, 17:1530–1548, 2015.

[80] V. N. Strocov, L. L. Lev, F. Alarab, P. Constantinou, X. Wang, T. Schmitt, T. J. Z. Stock, L. Nicolaï, J. Očenášek, and J. Minár. High-energy photoemission final states beyond the free-electron approximation. *Nature Communications*, 14(1):4827, Aug 2023.

[81] Anja Haags, Dominik Brandstetter, Xiaosheng Yang, Larissa Egger, Hans Kirschner, Alexander Gottwald, Mathias Richter, Georg Koller, François C. Bocquet, Christian Wagner, Michael G. Ramsey, Serguei Soubatch, Peter Puschnig, and F. Stefan Tautz. Tomographic identification of all molecular orbitals in a wide binding-energy range. *Phys. Rev. B*, 111:165402, 2025.

[82] Nicolas Tancogne-Dejean, Micael J. T. Oliveira, Xavier Andrade, Heiko Appel, Carlos H. Borca, Guillaume Le Breton, Florian Buchholz, Alberto Castro, Stefano Corni, Alfredo A. Correa, Umberto De Giovannini, Alain Delgado, Florian G. Eich, Johannes Flick, Gabriel Gil, Adrián Gomez, Nicole Helbig, Hannes Hübener, René Jestädt, Joaquim Jornet-Somoza, Ask H. Larsen, Irina V. Lebedeva, Martin Lüders, Miguel A. L. Marques, Sebastian T. Ohlmann, Silvio Pipolo, Markus Rampp, Carlo A. Rozzi, David A. Strubbe, Shunsuke A. Sato, Christian Schäfer, Iris Theophilou, Alicia Welden, and Angel Rubio. Octopus, a computational framework for exploring light-driven phenomena and quantum dynamics in extended and finite systems. *The Journal of Chemical Physics*, 152(12):124119, 2020.

[83] Peter Puschnig. private communication.

[84] Gerd Schönhense. Circular dichroism and spin polarization in photoemission from adsorbates and non-magnetic solids. *Physica Scripta*, 1990(T31):255, 1990.

[85] Christian S. Kern, Xiaosheng Yang, Giovanni Zamborlini, Simone Mearini, Matteo Jugovac, Vitaliy Feyer, Umberto De Giovannini, Angel Rubio, Serguei Soubatch, Michael G. Ramsey, F. Stefan Tautz, and Peter Puschnig. Circular dichroism in the photoelectron angular distribution of achiral molecules, 2025.

[86] L. Broekman, A. Tadich, E. Huwald, J. Riley, R. Leckey, T. Seyller, K. Emtsev, and L. Ley. First results from a second generation toroidal electron spectrometer. *Journal of Electron Spectroscopy and Related Phenomena*, 144-147:1001–1004, 2005. Proceeding of the Fourteenth International Conference on Vacuum Ultraviolet Radiation Physics.

[87] S. Weiß, D. Lüftner, T. Ules, E. M. Reinisch, H. Kaser, A. Gottwald, M. Richter, S. Soubatch, G. Koller, M. G. Ramsey, F. S. Tautz, and P. Puschnig. Exploring

three-dimensional orbital imaging with energy-dependent photoemission tomography. *Nature Communications*, 6(1):8287, Oct 2015.

[88] Benjamin Stadtmüller, Martin Willenbockel, Sonja Schröder, Christoph Kleimann, Eva M. Reinisch, Thomas Ules, Sergey Soubatch, Michael G. Ramsey, F. Stefan Tautz, and Christian Kumpf. Modification of the ptcda-ag bond by forming a heteromolecular bilayer film. *Phys. Rev. B*, 91:155433, 2015.

[89] Soohyun Cho, Jin-Hong Park, Soonsang Huh, Jisook Hong, Wonshik Kyung, Byeong-Gyu Park, J. Denlinger, Ji Shim, Changyoung Kim, and Seung Park. Studying local berry curvature in 2h-wse2 by circular dichroism photoemission utilizing crystal mirror plane. *Scientific Reports*, 11, 2021.

[90] Jakub Schusser, H. Orio, Maximilian Ünzelmann, J. Heßdörfer, M. Masilamani, F. Diekmann, K. Rossnagel, and F. Reinert. Towards robust dichroism in angle-resolved photoemission. *Communications Physics*, 7, 2024.

[91] Pseudopotential implementation in abinit.